

UC Berkeley

UC Berkeley Electronic Theses and Dissertations

Title

Photon upconversion improvements via molecular antenna and their applications

Permalink

<https://escholarship.org/uc/item/0z08g145>

Author

Garfield, David Jason

Publication Date

2017

Peer reviewed|Thesis/dissertation

Photon upconversion improvements via molecular antennae and their applications

by

David Jason Garfield

A dissertation submitted in partial satisfaction of the

requirements for the degree of

Doctor of Philosophy

in

Chemistry

in the

Graduate Division

of the

University of California, Berkeley

Committee in charge:

Professor Gabor Samorjai, Co-chair

Professor P. James Schuck, Co-chair

Professor Peidong Yang

Professor Daniel M. Kammen

Fall 2017

Photon upconversion improvements via molecular antenna and their applications

Copyright © David Jason Garfield 2017

All Rights Reserved

Abstract

Photon upconversion improvements via molecular antennae and their applications

by

David Jason Garfield

Doctor of Philosophy in Chemistry

University of California, Berkeley

Professor Gabor Samorjai, Co-chair

Professor P. James Schuck, Co-chair

The efficient conversion of low-energy, near-infrared (NIR) photons to higher energies promises advancements across a range of disparate fields, from more efficient solar energy capture to advanced biologic studies and therapies. At the forefront of this effort, upconverting nanoparticles (UCNPs) contain an array of lanthanide ions alloyed into a ceramic matrix, most commonly NaYF_4 . These lanthanide ions possess a 4f orbital manifold with a series of ladder-like, long-lived electronic states, allowing the sequential absorption of NIR photons at relatively low photon flux. The electrons climb the 4f Stark levels, absorbing multiple photons from the excitation source before relaxing back to the ground state upon emission of a photon with an energy higher than those from the source. While UCNPs are among the most efficient systems for converting NIR light to visible, they still hold key limitations, namely, they only weakly absorb incoming photons, hindering their external quantum efficiencies and overall performance.

This thesis presents studies designed to enhance the efficiency and brightness of UCNPs. One method to circumvent the inherently weak absorption in UCNPs involves attaching organic dye antennae to the surface of the nanoparticles to absorb incoming light and funnel the absorbed energy into the UCNP. However, a detailed understanding of the energy transfer mechanism between dye and UCNP is required to fully realize the potential of this system. We propose, using a series of spectroscopic and kinetic measurements, that this energy transfer is mediated via the absorbing dye triplet state, and further that the intersystem crossing rate within the dye is enhanced by interactions with the heavy nuclei of the lanthanides within the UCNP. We then design a highly efficient dye:UCNP hybrid system utilizing this new understanding. Lastly we present a study highlighting the power and potential of using UCNPs for biological applications. Together these studies will advance the utilization of photon upconversion towards realizing its promise in applications.

Preface

Scientists call the current epoch the Anthropocene, in order to emphasize the magnitude with which humans now influence Earth. No human influence has a more profound impact on the planet than man-made climate change. Caused by the combustion of ancient plant and animal matter converted to energy-dense fossil fuels through anaerobic decomposition, pressure, and time, humanity's thirst for energy has resulted in a >40% increase in atmospheric CO₂ concentrations since the Industrial Revolution, and it continues to rise. If left unabated, or even lackadaisically abated, this dramatic alteration of the Earth's atmosphere will result in a profound shift of the global climate and will affect every human into the distant future. In order to avert the harshest of these civilization-wide impacts, the International Panel on Climate Change asserts that global mean temperatures must be kept from rising more than 2°C over pre-Industrial Revolution levels, providing the World with an aggregate CO₂ budget, and one that looks increasingly unlikely to be maintained.

Nonetheless, in order to achieve the goal of $\leq 2^\circ\text{C}$ rise in global mean temperature, projections estimate that society must cut carbon dioxide emissions 80% versus 2005 levels by the year 2050, and transition to zero or even negative carbon dioxide emissions by the end of the 21st century. This would amount to the largest technological revolution in human history, converting tens of trillions of dollars worth of the global economy towards non-CO₂ emitting technologies. Of the potential options to power the increasing energy demands of a rising global population: wind power, nuclear fission, nuclear fusion, geothermal, wave/ tidal power, biomass, and solar. Other than nuclear fission, which remains prohibitively expensive, and nuclear fusion, which remains technologically out of reach, and geothermal, which does not have the capacity to meet global demand, all of the other forms of clean energy derive their energy from the Sun. Even fossil fuels in the end derived their energy from the Sun in the form of ancient photosynthesis. And so it only makes sense to collect this radiant energy directly from the source, our nuclear fusion reactor in the sky.

Silicon remains the most prolific material for solar photovoltaics, yet despite the technology's precipitous drop in price from 2009-2017, as production of the modules became a commodity product at tremendous scale, it is currently projected that silicon alone will not drive demand for clean energy fast enough to abate climate change. One issue involves energy storage. The combined price of solar plus storage is really the metric of interest, since traditional energy sources of the fossil variety, and battery prices do show similar cost reductions of late. Another issue is the inherent costs of silicon photovoltaics. In order to reduce these costs, photovoltaic efficiencies can be improved. Improving the efficiency of the module requires less material, land, and external balance of systems to collect the same amount of power, and thus has the potential to decrease photovoltaic prices. It is this second challenge that I will focus on in the work that follows.

To my son Owen

Contents

1 Introduction	1
1.1 Overview.....	1
1.2 Lanthanide-doped upconverting nanoparticles	2
1.2.2 Designing UCNPs.....	4
1.2.3 Limitations and potential solutions.....	6
1.3 Dye-sensitized lanthanides	6
1.3.1 Förster resonance energy transfer	7
1.3.2 Dexter electron transfer	7
1.3.3 Triplet energy transfer and the heavy atom effect	8
1.3.4 Dye-sensitized UCNPs	8
2 Methods	10
2.1 Overview.....	10
2.2 Colloidal nanoparticle synthesis.....	10
2.3 Transmission electron microscopy.....	12
2.4 Upconverted confocal microscopy	14
2.4.2 Confocal microscopy through brain tissue	16
2.5 Dye-sensitization of UCNPs.....	16
2.6 Time-gated photoluminescence	17
2.7 Upconversion quantum yield.....	18
3 Enrichment of molecular antenna triplets amplifies upconverting nanoparticle emission.....	21
3.1 Abstract	21
3.2 Introduction	21
3.3 Evidence of a resonant triplet.....	22
3.4 Enhancing triplet populations with photoactively-inert lanthanides	24
3.5 Quantification of triplet energy sensitization of upconverting nanoparticles	25
3.6 Upconversion enhancement factor and quantum efficiency	27
3.7 Energy-transfer distance dependence	30
3.8 Conclusion	30
3.9 Materials and Methods.....	31
3.9.1 Materials	31
3.9.2 Flask synthesis of core UCNPs	31
3.9.3 Automated synthesis of UCNPs	31
3.9.4 Synthesis of core/shell UCNPs.....	32
3.9.5 Nanoparticle characterization	32
3.9.6 Synthesis of IR-806.....	32
3.9.7 Functionalization of UCNPs with IR-806.....	32
3.9.8 IR806-UCNP film encapsulation.....	33
3.9.9 Absorption measurements	33
3.9.10 Steady-state fluorescence measurements	33
3.9.11 Theoretical calculations	33
3.9.12 Upconverted emission measurements	34

3.9.13 Time-gated triplet phosphorescence measurement.....	34
3.9.14 Two-photon excitation spectrum	35
3.9.15 Singlet lifetime measurements	35
3.9.16 Quantum yield measurement	35
3.9.17 Cyclooctatetraene experiments.....	36
Supplementary Figures	37
Supplementary Discussion	49
4 Up-converting nanoparticle microbulbs for deep tissue optical stimulation and imaging	51
4.1 Introduction	51
4.2 Synthesis of UCNPs for bright blue emission	52
4.3 UCNP micro lightbulbs.....	54
4.4 Imaging through thick brain slices.....	57
4.5 Discussion	59
5 Conclusions.....	61
5.1 Summary	61
5.2 Dye-sensitized UCNP efficiency improvement	61
5.2.1 Dye optimization	61
5.2.2 Dye: UCNP optimization	62
Bibliography	64

List of Figures

1.1 Opportunities for upconversion in solar energy capture	1
1.2 Transmission of light through mouse brain cortex.....	2
1.3 Ln^{3+} ion f-orbital transitions	3
1.4 Photon upconversion mechanisms.....	5
2.1 Depiction of the nucleation and growth of colloidal nanoparticles.....	11
2.2 Focal-series reconstruction of Fe_2O_3 nanoparticle	14
3.1 Dye-functionalized UCNPs, their mechanism of energy transfer, and the larger effective absorption cross-section of dyes relative to UCNPs	22
3.2 Time-gated photoluminescence as evidence of resonant triplet states.....	24
3.3 Evidence of triplet energy transfer to UCNPs.....	27
3.4 Upconverted performance improvements by enhancing dye triplet population.....	29
S.3.1 Cartoon schematic of time-gated triplet phosphorescence setup.....	37
S.3.2 IR806 Two-photon action spectrum	38
S.3.3 IR806 Two-photon action spectrum power dependence	39
S.3.4 Representative transmission electron micrograph of $\text{NaY}_{0.48}\text{Gd}_{0.3}\text{Yb}_{0.2}\text{Er}_{0.02}\text{F}_4$ nanocrystals.....	40
S.3.5 Representative transmission electron micrograph of $\text{NaY}_{0.78}\text{Yb}_{0.2}\text{Er}_{0.02}\text{F}_4$ nanocrystals.....	41
S.3.6 Representative transmission electron micrograph of $\text{NaGd}_{0.78}\text{Yb}_{0.2}\text{Er}_{0.02}\text{F}_4$ nanocrystals.....	42
S.3.7 Representative diffraction pattern of UCNPs	43
S.3.8 IR806-UCNP steady-state stability in air	44
S.3.9 IR806-UCNP dynamic stability	45
S.3.10 Visible upconverted emission at low excitation flux.....	46
S.3.11 Brightness enhancement from dye sensitization	47
S.3.12 Power-dependent enhancement from dye sensitization	48
Table S.3.1. Lowest lying triplet energies from TDDFT calculations	49
4.1 Energy level diagram of trivalent Yb and Tm.....	52
4.2 Optimization of UCNPs for blue emission.....	53
4.3 Micro lightbulb fabrication	55
4.4 Schematic of the characterization setup	56
4.5 Micropillar photoluminescence characterization	57
4.6 Imaging micro lightbulbs through mouse brain.....	58
4.7 Evaluating micro lightbulbs for optogenetic applications.....	59

Acknowledgements

I would like to first thank my advisor P. James Schuck for giving me the opportunity to perform this work. As became quickly clear to me at the beginning of the PhD, a purely synthetic project, despite holding a profound mission such as potentially enabling solar fuels, was not for me. Jim saw past my early blunder and took a chance on me. In this light I would also like to thank Gabor Somorjai for his many words of wisdom and nuggets of sage advice, and for introducing me to Jim. And I would like to thank the late Heino Nitsche for serving as chair to my thesis committee. His kind words and humor made the process much less intimidating, and I will forever remember our discussions.

I would not be where I am today without the help of Nicholas Borys. His unrelenting patience and mentorship provided me the tools to start a PhD afresh two years in, and still come out on time. Without Nick I could not have performed half of these experiments, and the other half would not have had the elegance that they do.

I would like to thank my wife for her love, support, patience and understanding, without which I would not be here today. I look forward to a marriage absent the PhD. I would like to thank my son Owen for his endless light to get me through dark times. This achievement also could not have happened without parents, who have shaped me into the person I am today, and given their support when support was needed. Lastly I thank all the teachers throughout my extensive educational career, who have provided me a wealth of knowledge for which I am eternally grateful.

1 Introduction

1.1 Overview

Modulating the frequency of low-energy light to higher energies, known as upconversion, holds promise across a wide variety of fields. For instance, solar cells cannot absorb photons with energies below the bandgap of the semiconducting material. Silicon, the most prolific solar cell material, has a bandgap of 1.1 eV, and therefore cannot absorb roughly half of the Sun's photons, those with energies less than 1.1 eV (See Figure 1.1). However, if a material placed on the backside of the semiconductor could absorb the transmitted infrared light to which the semiconductor is transparent, upconvert that light to visible wavelengths and emit the visible light back to the semiconductor, one could imagine a scheme where the overall efficiency could be greatly enhanced¹. Going back to silicon, theoretical maximum efficiencies would improve from 33% to 40% with the addition of an ideal upconverter². The late Professor David Dornfeld likened the upconverters to a turbo-charger for solar cells.

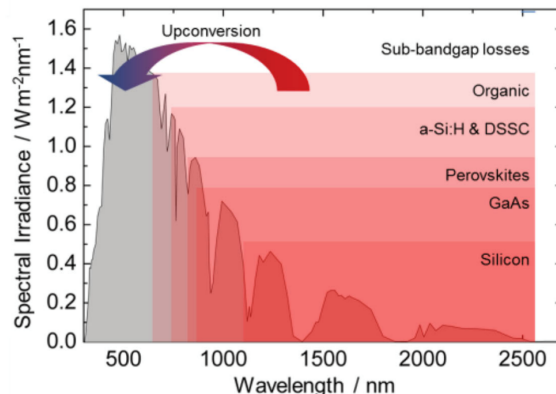


Figure 1.1. Opportunities for upconversion in solar energy capture. The grey area represents the solar irradiance at AM1.5, and the overlap with the various red squares represents the sub-bandgap loss for a range of semiconductor materials. (Reproduced from Fischer *et al.*³)

Upconversion also promises to be extremely useful in biology. Imaging studies using traditional dyes as luminescent probes suffer in signal-to-noise due to autofluorescence from surrounding cell media, as well as in tissue penetration depths due to the energetic limitations with which dyes operate (typically in the visible), coupled with the strong absorption of visible wavelengths in biological tissue (See Figure 1.2). However, upconversion alleviates both of these shortfalls. Upconverted autofluorescence is extremely rare in biological tissue, greatly increasing the signal-to-noise for these processes. Furthermore, lanthanide-doped upconverters absorb primarily in the infrared range of the electromagnetic spectrum, allowing the excitation light to exploit several near-infrared (NIR) windows found in tissue. Because the scattering cross-section through tissue scales as λ^{-4} , NIR light can penetrate orders of magnitude deeper into tissue than visible light^{4,5}.

Herein we will examine one type of upconverting material: lanthanide-doped upconverting nanoparticles (UCNPs). In this chapter I will introduce UCNPs, both from a photophysical and synthetic background. I will also introduce organic dyes, as these were used as antennae for a bulk of the work of this thesis. I will then focus on the questions remaining in optimizing the efficiency and brightness of UCNPs, and outline the remainder of the thesis.

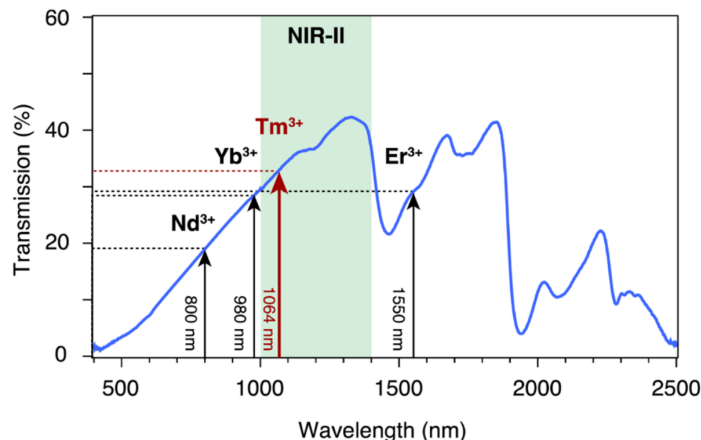


Figure 1.2. Transmission of light through mouse brain cortex. Arrows show respective absorption for various Ln^{3+} infrared absorptions. Reproduced from Levy *et al.*⁵⁾

1.2 Lanthanide-doped upconverting nanoparticles

Lanthanide-doped upconverting nanocrystals convert near-infrared (NIR) photons to higher energies by absorbing multiple NIR photons before emitting a single photon at higher energy. These absorptions occur through a series of real intermediate electronic states, in contrast to the simultaneous absorptions in multi-photon excitation through virtual intermediate excited states. It is this key difference that allows UCNPs to upconvert light ~ 5 - 6 orders of magnitude more efficiently than multi-photon excitation⁶.

The lanthanide ions in UCNPs typically occupy a 3^+ oxidation state, with the $4f$ manifold filling with electrons as one moves from La to Lu. These $4f$ electrons provide the upconverting properties to the lanthanides, since these electronic states form a ladder-like series of energy levels with energetic spacing on the order of NIR light (See Figure 1.3). Absorption and emission events occur via $4f^N \rightarrow 4f^N$ electronic transitions, yet $f \rightarrow f$ transitions are Laporte (parity) forbidden in centrosymmetric molecules:

$$\int_{-\infty}^{\infty} \psi_{el} \hat{\mu} \psi_{el}^{ex} d\tau = |\langle i | \hat{\mu} | f \rangle| \quad (1.1)$$

where ψ_{el} and ψ_{el}^{ex} represent the initial and final electronic wavefunctions, respectively, and $\hat{\mu}$ represents the transition dipole moment operator. This equation represents the core of Fermi's Golden Rule:

$$\lambda_{if} = \frac{2\pi}{\hbar} |\langle i | \hat{\mu} | f \rangle|^2 \rho_f \quad (1.2)$$

where λ_{if} represents the transition probability from state i to f , and ρ_f represents the density of final states. Thus UCNP are typically weak absorbers of incoming light, since the integral of Eq. 1.1 and therefore Eq 1.2 would be zero for initial and final states of the same inversion symmetry.

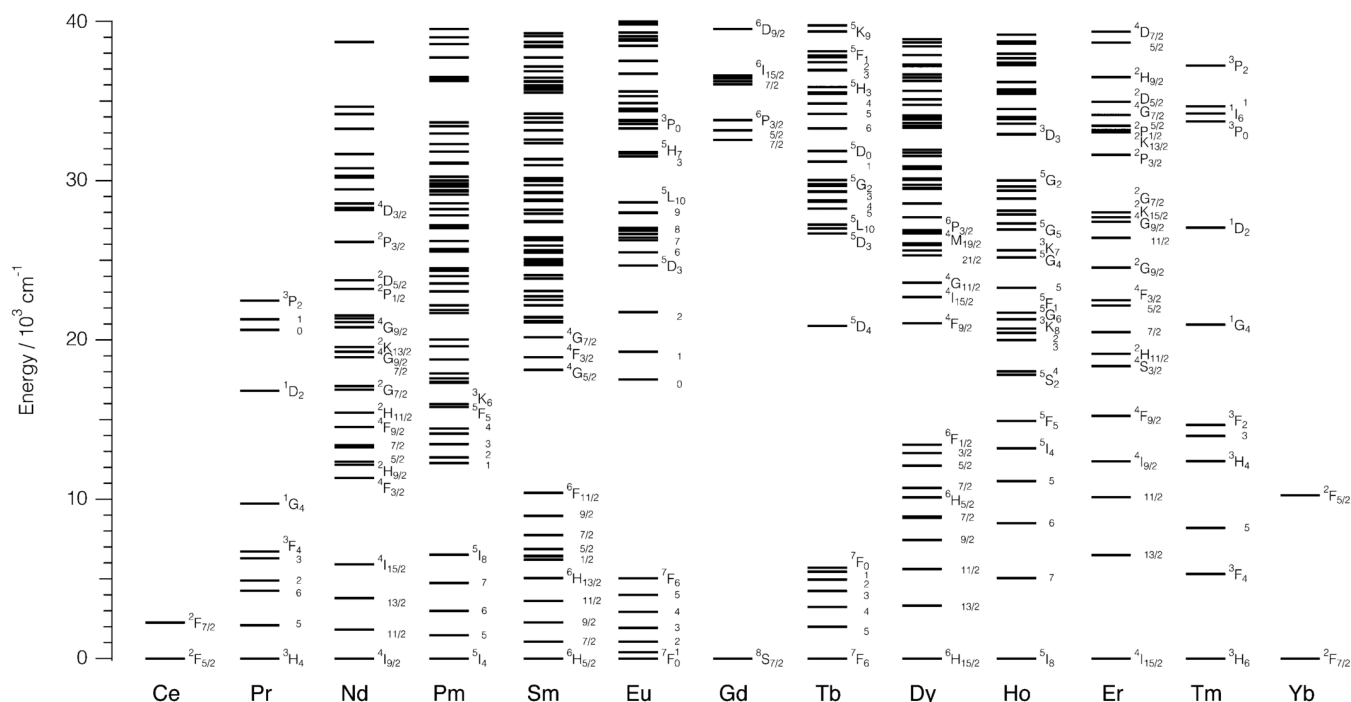


Figure 1.3. Ln^{3+} ion f-orbital transitions. Energy levels represented by their $^{2S+1}L_J$ term symbols, where S , L , and J represent the total spin, orbital and angular momentum quantum numbers, respectively. (Reproduced from Chan.⁷)

The lanthanide ions contribute other key attributes to UCNP. The partially filled $4f$ -orbital manifolds remain mostly shielded from their environment due to outer shell $5s$, p manifolds, giving the orbitals an almost atomic-like nature. The line shape of the emission spectra are determined by crystal-field Stark splitting of the respective $^{2S+1}L_J$ energy levels, where S , L , and J represent the spin, angular momentum, and total angular momentum quantum numbers, respectively, caused by the electrostatic external field of the host matrix⁸. These line shapes are ~ 10 - 100 cm^{-1} wide, much narrower than a typical organic dye with spectral linewidths on the order of 1000 - 2000 cm^{-1} , and therefore give spectral purity to UCNP emission.

The prototypical UCNP system employs the ceramic host NaYF_4 , with various combinations of lanthanide ions replacing the Y^{3+} sites. NaYF_4 can form two phases, β and α , where the former is a hexagonal phase and the latter is a cubic phase. Because the Laporte selection rules can be relaxed when the lanthanide ion is placed in a crystal structure without inversion symmetry, the NaYF_4 UCNP in the β -phase are 1-2 orders of magnitude brighter than similar α -phase UCNP^{9,10}. The NaYF_4 crystal structure also

has low phonon vibrational energies, helping to inhibit nonradiative relaxation pathways through phonon emission into the crystal lattice.

The Laporte-forbidden f-f transitions within the lanthanides are responsible for the crucial attribute of UCNPs, namely upconversion itself. Upconversion is ultimately a kinetic problem, and one must compare the rate of excitation to the rate of relaxation. In order to multiply excite an electron with any meaningful probability before it relaxes, the rate of excitation must be significantly greater than the rate of relaxation:

$$k_{ex} \gg k_{rel} \quad (1.3)$$

where k_{ex} and k_{rel} represent the rates of excitation and relaxation, respectively. Because of the parity-forbidden nature of the f-f transitions within the lanthanides, and the fact that the 4f orbitals are partially shielded by the outer 5s and 5p orbitals and are thus protected against non-radiative phonon-coupled relaxation to the environment, lanthanide ions enjoy excited-state lifetimes on the order of 10 μ s – 10 ms. These long lifetimes, in turn, give the nanocrystals their unique upconverting properties at photon fluxes relevant for applications in solar and biological studies.

1.2.2 Designing UCNPs

Several parameters can be tuned when designing an optimum UCNP system. Before a synthesis even begins, one must choose the ratio of various lanthanide ions depending on the ultimate use of the UCNP. Size and shape of the nanoparticles, as well as morphology are also critical. And post-synthetic work-ups involving ligand exchange, ligand-stripping or functionalization, drop-casting, spin-coating, and many other physical and chemical manipulations can be achieved.

The most common UCNP composition consists of a NaYF₄ host matrix, with 20% of the Y³⁺ replaced by Yb³⁺ and 2% of the Y³⁺ replaced by Er³⁺. This yields an upconverting system that absorbs primarily at 980 nm due to the Yb³⁺ ²F_{7/2}→²F_{5/2} transition and emits at 550 nm and 660 nm due to the Er³⁺ ⁴S_{3/2}→⁴I_{15/2} and ⁴F_{9/2}→⁴I_{15/2} transitions, respectively (See Figure 1.3). Yb³⁺ is used as the sensitizer ion for its large absorption cross-section relative to other lanthanides¹¹. The Yb³⁺ then nonradiatively transfers its excited energy to the emitting Er³⁺. Subsequent Er³⁺ excitations occur via either inter- Er³⁺: Er³⁺ interactions or from another Yb³⁺: Er³⁺ interaction (See Figure 1.4).

While Yb³⁺: Er³⁺ systems are most common, they are not at all exclusive. Because all fourteen Ln³⁺ ions are of similar size, and similar in size to Y³⁺, synthesis of any variety of UCNP is effectively modular, with >95% incorporation effectiveness⁷. Thus systems can be designed based on maximizing a specific color emission (See Chapter 4), isolating color purity¹¹, or more complex structures can be engineered to achieve the desired properties¹².

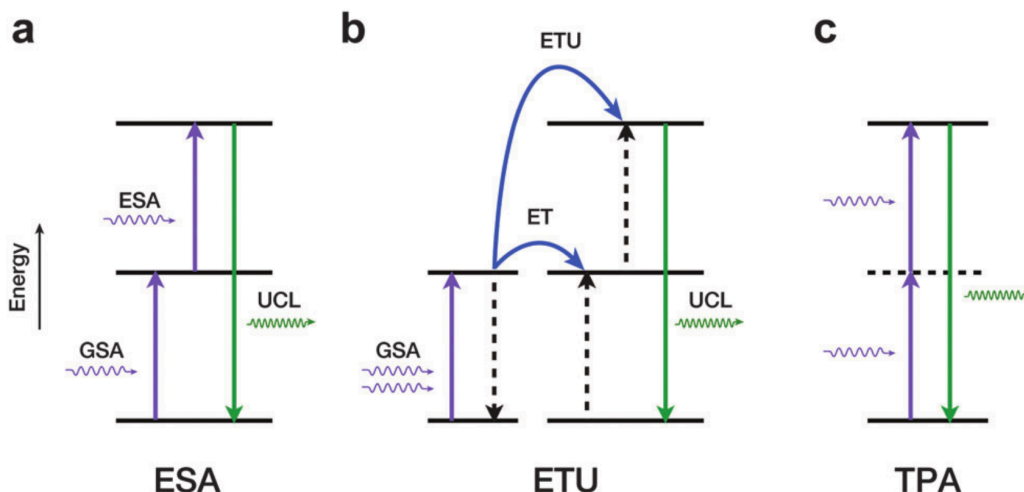


Figure 1.4. Photon upconversion mechanisms. **a.** Sequential excited state absorption (ESA) via ground state absorption (GSA) followed by ESA, and subsequent Upconversion Luminescence (UCL), all by the same ion. **b.** Energy transfer upconversion (ETU), similar to ESA but utilizing a sensitizer ion to absorb incoming photons followed by energy transfer (ET) to the emitting ion. **c.** Simultaneous two-photon absorption (TPA) via an imaginary intermediate excited state, followed by UCL. (Reproduced from Chan.⁷)

The size of upconverters is determined by a variety of factors similar to other colloidal synthesis techniques including reaction time, temperature, relative concentrations of the precursors, relative concentrations of the ligands (oleic acid, oleylamine), reducing agents (oleylamine), etc. Though I have successfully run many of these reactions myself, I am by no means an expert in synthesis, so I will defer to experts in this regard^{9,13–17}. In general, the synthesis is a one-pot reaction on a Schlenk line in air-free conditions, with reaction temperatures around 310°C and total synthesis time of approximately 1/2 a day. β -phase is the thermodynamic product, and thus tends to proliferate at higher temperatures and longer reaction times.

Post-synthesis, the particles will remain in a homogenous solution for up to two years in a well-sealed sample vial. Some recommend adding a small excess of oleic acid to the vial; however, I do not recommend this as it will make ligand exchange more difficult in the future. As noted above, many post-synthesis workups are possible. The native ligand is typically oleic acid, with the carboxyl group bound to the UCNP surface and the aliphatic chain extending from the surface. These particles are soluble in organic, non-polar solvents such as toluene or hexane. A ligand exchange through mass action^{18,19} or polymer wrapping with an amphiphilic polymer¹³ allows the particles to be soluble and stable in polar solvents, including water, which is vital for biological studies. Furthermore, the particles can be added to a solution of dissolved polymer such as polystyrene in toluene and spun onto a substrate to form a homogeneous film for solid-state applications such as solar cell backings.

1.2.3 Limitations and potential solutions

While UCNPs hold much promise, these upconverting nanoparticles do not come without limitations. Of primary importance is their low absorption cross-sections, which is one attribute leading to their low upconversion quantum yields (UCQY):

$$UCQY = \frac{\# \text{ of photons emitted}}{\# \text{ of photons absorbed}} \quad (1.4)$$

where the emitted photons must be of higher energy than the absorbed photons, by definition of upconversion, and therefore UCQY is limited to a maximum value of 50% for a two-photon process. Upconversion is a nonlinear process, and thus the UCQY scales with excitation power, since a higher photon flux yields a higher probability of exciting an already-excited electron. Because of the low absorption of UCNPs, most studies use monochromatic laser fluxes in the range of 10^3 W/cm², still far lower than those used in two-photon experiments with pulsed lasers ($10^{10} - 10^{12}$ W/cm²), but significantly higher than the single-color solar flux (~ 0.1 W/cm²)²⁰ or the FDA-approved irradiation levels (~ 1 W/cm²). Thus in order to make UCNPs effective for practical applications, the UCQY needs be improved.

Typically, the larger the particle, the less surface-related non-radiative losses are present, and thus the more efficient the particle. For instance the UCQY for bulk lanthanide-doped NaYF₄ material approaches 10%²¹ while the best UCQY for UCNPs is currently around 5% (See Chapter 3), though typical UCNP UCQYs are closer to $\sim 0.1\%$. One way to improve efficiency and mimic the properties of bulk crystals is to add an inert shell around the UCNP. Undoped NaYF₄ (or NaGdF₄, NaLuF₄, as long as the shell material has only inaccessible electronic states) is typically used in order to avoid surface quenching²², and recent studies have found that very thick shells (~ 15 nm thick) can yield UCQYs approaching bulk levels¹⁷, increasing the UCQY by an order of magnitude. These particles, however, become quite large by nano standards, sometimes 30-40 nm, and thus their practicality for single-molecule studies is inhibited.

Another approach to increasing upconversion efficiency utilizes antennae to absorb incoming light and then funneling this energy into the UCNP. This can be achieved through dropping UCNPs onto plasmonic structures^{23,24} or through binding organic dyes to the surface the nanoparticles^{25,26}. In the following section I will provide a brief overview of the burgeoning dye-sensitized UCNP field, a field which consumed the majority of my PhD and this dissertation.

1.3 Dye-sensitized lanthanides

Organic/inorganic hybrid systems are proving useful across a range of fields, and in fact science itself is finding its new innovations at the intersection of previously disparate fields. Coordination chemists have long known that highly-absorbing organic ligands covalently bound to individual lanthanide ions can greatly increase the lanthanide luminescence through non-radiative energy transfer into the lanthanide 4f manifold²⁷⁻²⁹. This strategy circumvents the weak absorption oscillator strength of the lanthanide ion by taking advantage of the much higher oscillator strength in the organic dye (extinction coefficients for dyes are $\sim 10^5 \times$ larger than UCNPs) before non-radiatively transferring the energy into the lanthanide. Several non-radiative energy

transfer mechanisms exist and have been explored, including Dexter and Förster energy transfer.

1.3.1 Förster resonance energy transfer

Förster resonance energy transfer (FRET), proposed³⁰ by Theodor Förster in 1948, involves the emission of a virtual photon from a donor state of one system to the acceptor state of a second system. This is essentially a dipole-dipole coupling interaction between the donor and acceptor states. Its strength depends on the spectral overlap of the donor emission with the acceptor absorption, as well as the spatial distance between acceptor and donor as follows:

$$k_{et} = \tau^{-1} \left(\frac{R_0}{r} \right)^6 \quad (1.5)$$

where k_{et} is the rate of energy transfer, τ is the donor lifetime, R_0 is the critical distance between donor and acceptor, known as the FRET distance, such that when $R_0=r$, $k_{et}=k_r$, where k_r is the radiative rate of decay. R_0 can be further defined as follows:

$$R_0 = 8.78 \times 10^{-2} \kappa^2 \Phi_D n^{-4} J \quad (1.6)$$

where κ represents the orientation factor between donor and acceptor, which for solutions equals 2/3, Φ_D represents the donor emission quantum yield, n represents the refractive index of the solvent, and J represents the spectral overlap between the donor emission and the acceptor absorption. Because of the R^{-6} distance-dependence, FRET processes are typically limited to system within <10 nm of one another. Furthermore, because the process effectively involves a virtual photon, it depends on the strength of the acceptor absorption oscillator strength, and therefore the scheme of dye-functionalizing lanthanides or UCNPs would not fully circumvent the weak absorption oscillator strength of the lanthanides.

1.3.2 Dexter electron transfer

Dexter energy transfer was formulated by D. L. Dexter in 1953, basing his work off of the previous work by Förster³¹. Dexter calculated that the exchange of an electron from donor to acceptor depends on wave-function overlap between the two states, and therefore has a strong, e^{-R} distance dependence:

$$k_{et} \propto J e^{-\frac{2r}{L}} \quad (1.7)$$

where k_{et} is again the rate constant of energy transfer, J is the spectral overlap integral between donor and acceptor, normalized by the absorption of the acceptor, r is the distance between donor and acceptor, and L is the spatial separation of donor and acceptor relative to their van der Waals radii. Essentially when the donor D becomes excited (D^*), if the donor is sufficiently close to the acceptor A (<~1 nm), the wave function of the excited-state electron in D^* can overlap with the wave function of an excited state hole in A, while at the same time a ground state electron in A overlaps with the ground state hole of D, and the two electrons swap places to form D and A^* .

Because in Dexter processes the overlap integral J is normalized to the absorption coefficient of A , this electron exchange depends much less on the absorption oscillator strength of A . This makes Dexter exchange processes ideally suited for sensitizing lanthanide ions, and allows the sensitizer to circumvent the weak absorption of the $4f \rightarrow 4f$ lanthanide transition, unlike with Förster transfer.

1.3.3 Triplet energy transfer and the heavy atom effect

Several studies have indicated, at least in the coordination chemistry field, that organic sensitizers in close proximity to lanthanides rapidly undergo intersystem crossing (ISC) due to the heavy atom effect caused by the lanthanide nuclei. The heavy nucleus (for lanthanides $Z=57-71$) aids in spin-orbit coupling between the sensitizer singlet and triplet states, effectively increasing the ISC rate to the sensitizer excited triplet state. Many studies have shown strong evidence that the sensitizer triplet is in fact an intermediate in the energy transfer from sensitizer to lanthanide³²⁻³⁴. In fact, because ISC is believed to be so rapid in these systems, it is believed that triplet intermediates, and subsequent Dexter electron exchange, are the dominant mechanisms for lanthanide sensitization.

1.3.4 Dye-Sensitized UCNPs

In 2012, Hummelen's group published the first paper showing the sensitization of UCNPs with organic dyes²⁵. In this seminal work, the authors used mass-action to exchange the native oleic acid and oleylamine ligands on the nanoparticles with a slightly modified infrared laser dye. The modification involved adding a carboxyl functional group to the center of the chromophore backbone to aid in attachment to the nanoparticle surface. This dye has an absorption centered at 808 nm. $\text{NaY}_{0.78}\text{Yb}_{0.2}\text{Er}_{0.02}\text{F}_4$ nanoparticles were used, with maximum absorption at 980 nm and upconverted luminescence from the Er^{3+} primarily at 550 nm and 660 nm. The authors showed a staggering $3,300\times$ enhancement when exciting these dye-functionalized UCNPs across the full absorption spectrum of the dye, versus exciting the unfunctionalized UCNPs directly across the full absorption of Yb^{3+} . Furthermore, under monochromatic excitation at the peak absorption wavelengths of the two respective parts, a $1,100\times$ enhancement was seen (808 nm versus 980 nm excitation). Thus the majority of this enhancement can be attributed to the much stronger absorption cross-section of the IR dye compared with the Yb^{3+} absorption. Further, because as stated above, UCQY is a function of excitation intensity, and because the dye absorbs $\sim 10^5\times$ more photons at a given intensity, the effective power felt by the UCNP in the dye-functionalized case is orders of magnitude greater, and thus it can be expected that UCQY for the dye-functionalized case should also increase dramatically. This was not shown in the 2012 work; however it has been shown in subsequent dye-functionalized UCNP papers³⁵. The additional $3\times$ increase in upconverted emission ($3,300\times$ compared with $1,100\times$) is due to the former case taking advantage of the broader spectral absorption of the dye compared with the narrow-band Stark levels of the lanthanides (See Section 1.2).

Subsequent works have expanded from this original work since 2012. However, a perplexing lag in dye-sensitized UCNP publications between 2012 and 2015 occurred, despite the Hummelen work stirring much hype in the community. I believe this can be attributed to the difficulty in reproducing this original work⁶. Most likely, based on my

experience, these issues with reproducibility stem from the instability of dye-UCNP systems in air. This instability arises from the enhanced ISC rates discussed in Section 1.3.3. The subsequent dye triplet states readily react with O_2 in the atmosphere, which has a triplet ground state. These undergo triplet-triplet annihilation, promoting the O_2 to the excited singlet state. And singlet oxygen (O_2^*) is highly oxidative, and can readily oxidize and thus photobleach the proximate dye molecule, effectively killing it. Thus in my experience, all dye-functionalized UCNP work must occur in air-free (O_2 -free), and also water-free conditions.

Despite these reproducibility issues, in 2015 Prasad's group published a study in which they made UCNPs with a traditional core, and iterative shells doped with a single sensitizing lanthanide³⁶. The idea was to allow energy transfer to occur from dye to the outer shell, with subsequent energy-transfer steps into the inner core, upon which upconversion would allow Anti-Stokes emission. This in theory allows one to take advantage of the more efficient core-shell UCNPs while also taking advantage of dye-sensitization. However, this core-“active-shell” approach used a Nd^{3+} -doped shell, with a main transition at 800 nm, and was thus optimized for dye-singlet \rightarrow Nd^{3+*} energy transfer, and the authors only saw a 14 \times increase in overall upconverted brightness versus the non-functionalized UCNPs. Granted, this enhancement comparison could be flawed if one measurement has a much smaller numerator compared with the other (something one could expect with shelled versus unshelled particles); however, it was unlikely that the two orders of magnitude difference in enhancement could be explainable by this alone (typical enhancements from shelling are one order of a magnitude). Somewhat audaciously, the authors claimed that Förster energy transfer dominates from dye to UCNP, due to the “unchanged spin-flip” in these systems.

Subsequent work from a related cohort of authors also published on dye-sensitized UCNPs. All subsequent work followed this same line of “active shells”. As an aside, it has been shown that back energy transfer from excited lanthanides out to outer shells readily occurs, and thus the surface-passivation effect expected from shells without energetically accessible transitions (traditional $NaYF_4$, $NaGdF_4$, etc.) does not occur in these “active shell” systems. Despite this, some of these works have achieved impressive UCQYs, using slightly different dye molecules or lanthanide compositions³⁵. However, none of the works up until that contained in this thesis explored the energy transfer mechanism between dye and UCNP in detail, a curious phenomenon given the overwhelming evidence from the coordination chemistry community that sensitizer triplet states are the predominant intermediate in energy transfer to lanthanides.

The remainder of this thesis will break down as follows. Chapter 2 will be devoted to the experimental methods used within. Spectroscopic and synthetic details will be explained. Chapter 3 will be devoted to the work done in elucidating the mechanism of energy transfer from dye to UCNP. The major demonstration within this chapter being that the dye undergoes intersystem crossing before energy transfer occurs to the UCNP, and that this ISC (and subsequent energy transfer) can be enhanced by adding otherwise energetically-inert lanthanides to the UCNP. Chapter 4 will show one potential application for UCNPs, displaying the deep-tissue penetration capabilities of NIR light. Chapter 5 will conclude and highlight potential routes for future work.

2 Methods

2.1 Overview

A key part of any scientific endeavor involves building up a toolkit with which to probe for answers to the questions posed by the scientist. When Richard Feynman posited in 1959 that “There is plenty of room at the bottom,” meaning that the advent of the manipulation of matter at the atomic scale represented an untapped avenue in science, he could not have imagined the toolbox nanoscientists now enjoy less than 60 years later. Nanoscience requires a way to “see” what one has made. I regularly joke in the lab that I will use my nanovision to see if I made what I intended to make. Unfortunately, nanovision is physically impossible, since by definition the minimum dimension of a nano-anything is < 100 nm, and visible light (the part of the electromagnetic spectrum we as humans evolved to detect with our eyes) ranges from 400-700 nm. Thus based on the diffraction limit, where at best you can half the wavelength of the probing photon to discern between two points that distance apart, visible light can only discern features on the order of ~ 200 nm. Fortunately for the nanoscientist, other standard particles such as X-rays and electrons have much smaller wavelengths than visible photons. Thus techniques such as X-ray diffraction (XRD) and transmission electron microscopy (TEM) can discern features down to single lattice spacings in the former, or down to 0.5 \AA (0.05 nm) for the latter.

For this specific study, one must of course first make the nanoparticles of interest. Following this requisite step, standard characterization tools were used to ensure the correct particles were made, namely TEM. Assuming the desired particles are in hand, their key attribute, i.e. upconversion was most commonly tested using a custom-built inverted confocal microscope. Further upconversion enhancement can occur via dye-sensitization, and these dye triplet excited state emissions can be detected via a custom-built time-gated photoluminescence system. Finally the UCQY of the nanoparticles, both with and without dye, were measured and will be discussed.

2.2 Colloidal nanoparticle synthesis

Before a nanoparticle can be characterized, or used, it must first be synthesized. Nanoparticle synthesis can take many forms. However, Paul Alivisatos in 1988, along with Lou Brus at Bell Labs discovered a method of synthesizing CdSe nanoparticles using a liquid-based approach³⁷. In essence, coordinated metal precursors are first created *in situ*, by taking a metal of the proper oxidation state and heating it under inert atmosphere in a ligand solvent, such as trioctylphosphine or oleic acid. These precursors are then combined in a high-boiling solvent, most typically octadecene, with a weak reducing agent to strip the metal of its ligands, again *in situ*, and the metal monomers react and nucleate into nanoparticle seeds, which then ripen into larger nanoparticles. The size of the particles is determined by the speed with which the temperature is ramped up to the reaction temperature, since higher ramp rates will lead to more nucleation, and hence smaller particles for the final reaction. The size is also determined by the ratio of ligand to monomer, as well as the total concentration of monomer, and the amount of reducing agent (the more reducing agent, the more rapidly monomers with nucleate, and the smaller the particles). However, all of these are gross

generalizations, and a new synthesis can take dozens of attempts to yield the correct phase, size, etc. It also seems that certain people have a knack for synthesis – they “have good hands” some professors like to say – while others should be relegated to characterization or data analysis. The sizing most broadly follows the classical nucleation theory (CNT), and subsequently LaMer’s nucleation theory (See Figure 2.1 a and b). The principle idea is that the surface energy of clusters drops with radius, and thus small clusters will tend to ripen into larger clusters.

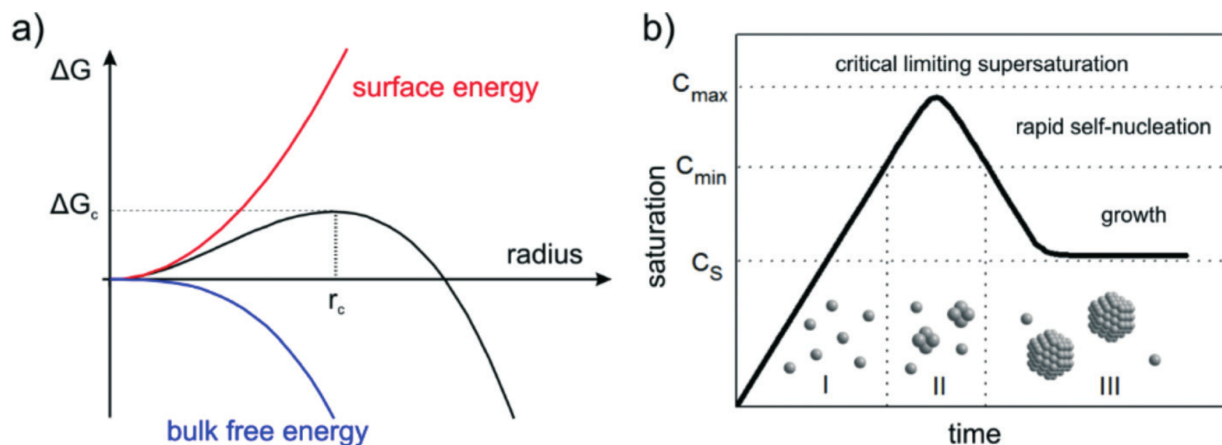


Figure 2.1. Depiction of the nucleation and growth of colloidal nanoparticles. **a.** Dependence of the free energy of the cluster on size. r_c is the critical size at which the particle becomes stable. **b.** Growth and ripening of nuclei into homogeneous nanoparticles. The curve represents the concentration of monomer precursor with time. (Reproduced from Polte.³⁸)

UCNP colloidal synthesis follows from this original work, as do all other colloidal nanoparticle syntheses I am aware of. For UCNPs, the lanthanides are bought with very high purity (preferably from Strem) as the LnCl_3 salts. These are added in the proper molar ratios to a three-neck round bottom flask. For NaYF_4 particles, the remainder of the Y sites are supplied by YCl_3 . To this salt mixture is added an excess of oleic acid and octadecene, and the flask is put under inert atmosphere on a Schlenk line and heated to approximately 50°C . The flask is then placed under vacuum and the temperature is ramped to 110°C , and held at this temperature for approximately 1 hour. This step ensures the formation of Ln-oleates, with three oleic acids bound to each Ln^{3+} atom (and Y^{3+}). Upon cooling the flask, it is opened to air and additional oleic acid, octadecene, sodium oleate, and ammonium fluoride are added. The flask is then put under inert atmosphere again, then vacuum once more to pull off any water and air at elevated temperatures ($\sim 80^\circ\text{C}$), before the growth phase begins. The mixture is then quickly ramped up to the desired growth temperature ($\sim 315^\circ\text{C}$ at a ramp rate of $20^\circ\text{C}/\text{min}$), and held at the reaction temperature for approximately an hour. The flask is then rapidly cooled, and the contents are transferred to a centrifuge tube and centrifuged at 6000 g for five minutes with the addition of a $1/1\ v$ of ethanol. The supernatant is removed and discarded, and the precipitated pellet is resuspended in fresh toluene (do not use hexane if it can be avoided, toluene is much less toxic to the laboratory scientist). This suspension is then spun at a lower speed of 3000 g to remove any salts that may have formed in the reaction such as NaF . Any nanoparticles of

interest will remain in the supernatant due to the ligand affinity for the solvent. To this supernatant is added another equivalent of ethanol, and the mixture is centrifuged again at 6000 *g*. The pellet is again collected, suspended in fresh toluene, and this last step is repeated once more. This will rid the nanoparticles of excess ligand. If ligand exchange is desired, the cleaning step should be repeated ~3 more times before ligand exchange, and immediately prior to ligand exchange, in order to ensure a bare UCNP surface while ensuring continued solubility.

2.3 Transmission electron microscopy

While several techniques exist to detect and characterize structural features on the nanoscale, including X-ray diffraction (XRD), dynamic light scattering (DLS), atomic force microscopy (AFM), scanning tunneling microscopy (STM), and transmission electron microscopy (TEM), I focus this section on TEM because of its familiarity, relative ease of use, and clarity. Like all aspects of modern science, all of these techniques have subfields and further sub-subfields, and could consume an entire PhD or team of PhDs on their own. I by no means claim to be an expert of TEM, and will present here nothing more than a cursory summary of the technique and some modern advances that may be pertinent to UCNP research. For a detailed understanding of TEM, please refer to a tremendous book on the subject by Fultz and Howe³⁹.

Louis de Broglie first postulated the wave-like behavior of matter in his 1924 Physics PhD thesis from the Sorbonne, for which he won the 1929 Nobel Prize in Physics. The seminal equation:

$$\lambda = \frac{h}{mv} \sqrt{1 - \frac{v^2}{c^2}} \quad (2.1)$$

where λ , h , m , v , and c , represent the wavelength of the particle, Plank's constant, the rest mass and velocity of the particle, and the speed of light in vacuum, respectively, prescribes the fundamental principle upon which electron microscopes function. By accelerating electrons from a sharp metal filament down the microscope chamber at very large energies, the microscopist produces electrons with extremely small wavelengths. For instance, for a 100 keV electron beam, the electron wavelength is only 0.037 Å. It is this essential attribute that allows TEMs to image objects on the nanoscale.

A very cursory description of the TEM is as follows. The main chamber of a traditional TEM must be under ultra-high vacuum (UHV, $< 10^{-7}$ Pa) in order to avoid electron collisions with molecules in the atmosphere. A sharp metal filament, most commonly tungsten, is given sufficient current to emit electrons via thermionic or field electron emission down the chamber. The electron beam is then collimated and focused using a series of magnetic and electrostatic lenses before reaching the sample, and further focused after transmitting through the sample onto the electron detector. Modern detectors use a large charge-coupled device (CCD) to detect the electrons spatially and temporally.

Many attributes determine the quality of the microscope, including the sharpness of the filament, the quality and stability of the lenses, and the quality of the detector. Further improvements can also be made. For instance, electron emission via field emission (essentially pulling electrons out of the metal using a very strong electromagnetic field) produces an electron beam with a much narrower wavelength spread than thermionic emission. This wavelength spread can be further narrowed using a monochromator at the top of the column to select only a narrow range of electron energies, limiting the range of electron energies to 0.15 eV. The smaller the energy spread in the electron beam, the less chromatic aberration occurs in the lenses.

Modern TEMs utilize a series of aberration correctors to account for electron and lens aberrations in the instrument. The two main aberrations limiting resolution are spherical and chromatic aberration. Spherical aberration occurs due to imperfections in the magnetic lenses which focus the electron beam. High-angle electrons relative to the optic axis are bent inaccurately by the magnetic field that constitutes the lens, and therefore depending on the angle of impinging electrons, the electron beam becomes non-uniform across the electromagnetic lenses. Chromatic aberration occurs due to the non-uniformity of the energies of the electrons within the beam. Two electrons with the same path but different energies will be focused differently by the magnetic field of the lens, creating less-than-ideal focusing, and therefore limiting the minimum resolution of the instrument. Both types of aberration can be somewhat corrected using modern aberration correction, which attempt to compensate for these expected non-ideal behaviors of the electron beam in real time. Some corrections can also be made in post-processing. To date even the most sophisticated TEMs achieve a resolution no better than 0.5 Å. However, practically speaking, this resolution is nothing to sneeze at, and is sufficient to detect sub-atomic features within a nanostructure.

The cutting edge of the electron microscopy field includes advances such as environmental TEMs that allow imaging in controlled, non-UHV atmospheres, low-dose rate imaging with amplitude and phase retention to image samples without incurring beam damage (See Figure 2.2), and advances in analytical TEM to detect not only spatial but compositional information on a sample using the ejected electrons within the sample itself to infer atomic composition with spatial information retained. It is this last technique that is especially pertinent to the UCNP field, as currently it remains unknown the specific arrangement of lanthanide ions within the nanoparticle structure.

Relevant to the UCNP scientist, TEM can provide us most directly with nanoparticle size and size distribution, as well as the crystal phase of the nanoparticle, be it α or β (See Section 1.2.2). More sophisticated techniques such as scanning transmission electron microscopy- energy dispersive spectroscopy (STEM-EDS) or electron energy loss spectroscopy (EELS) can provide compositional information of both the entire nanoparticle, as well as through a complicated core-shell structure. At the cutting edge, and currently not quite possible, would be a study which determines the binding method of the surface ligands onto the UCNP. This remains slightly out of reach to the electron spectroscopist due to the challenge of imaging such light elements as carbon and oxygen, as well as the challenge of imaging single atoms as opposed to

columns of atoms (this arises from the nature of only being able to detect those ligands at the periphery of a z-projection into two dimensions).

Specific instruction into actually utilizing a TEM depends on the individual instrument, and the techniques required to obtain the desired information. I will therefore encourage finding an expert on the machine of interest and going from there. Ultimately, the versatility and usefulness of TEM will allow it to remain an invaluable tool for the nanoscientist. After all, a picture is worth 1,000 words.

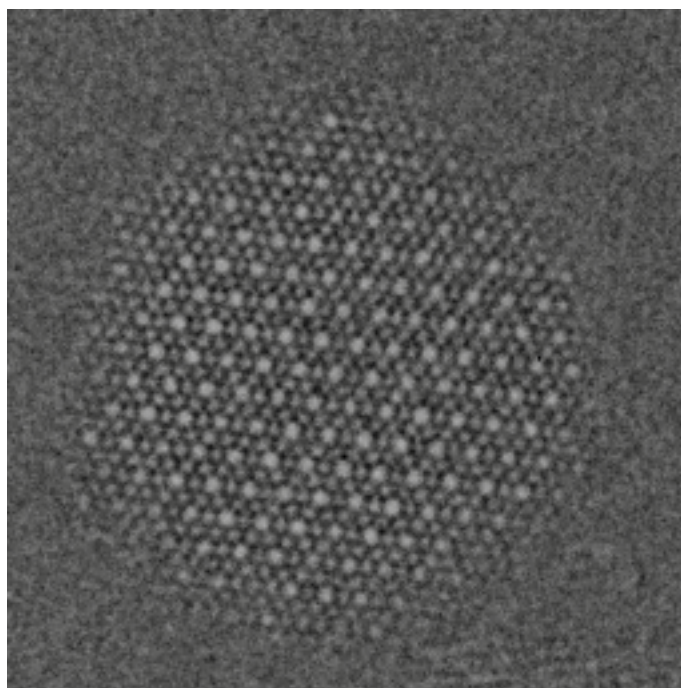


Figure 2.2. Focal-series reconstruction of Fe₂O₃ nanoparticle.

This image was taken on the TEAM 0.5 transmission electron microscope at the National Center for Electron Microscopy (NCEM), in collaboration with Christian Kisielowski. The current on the electron gun was reduced to a few zeptoamps, and the particle was kept in the shadow of the monochromator of the microscope until the system was ready to take the image. Upon imaging, a series of single images were taken at various focal lengths, and with this information the full phase of the electron exit wavefunction was reconstructed, allowing the superb resolution seen above. The diameter of the particle above is 4 nm. The larger atomic columns are the Fe³⁺, while the smaller are the O²⁻. With this technique, no knock-on beam occurs, allowing surface analysis and amorphous nanoparticle analysis.

2.4 Upconverted confocal microscopy

Despite the limitations imposed by the diffraction limit, optical microscopy remains an extremely useful tool when probing for information about a physical sample, even at the nanoscale. Optical energies (~1.7-3.1 eV) constitute an energetic range in which electrons are promoted from the ground state to excited states in a wide variety of

materials. Optical spectroscopy therefore provides information about electronic transitions within a material.

The workhorse of this PhD involved a custom-built inverted confocal microscope (See Figure 4.4). This instrument was based on a Nikon-series inverted microscope, equipped with two-axis piezo stages, a series of continuous-wave (CW) lasers at different wavelengths able to be used to excite the sample, and both an avalanche photodiode (APD) for photon counting, as well as a spectrometer for collecting spectral information in the collection path, with a flip mirror to choose between the two detectors. The sample was excited from below through a focusing lens, and emission from the sample was collected through the same objective lens. Dichroic filters were used to separate emission from excitation light, and a pinhole was used when spatial information was desired.

For facile upconversion characterization, a drop of UCNPs in hexanes or toluene was drop-cast onto a glass slide, which provided ample signal for the instrument set-up above. Somewhat unique to upconversion, short-pass dichroic filters of the appropriate pass wavelength (in between the excitation and emission energies) were used to ensure the detectors were not flooded with excitation light. For example, using the prototypical $\text{NaY}_{0.78}\text{Yb}_{0.2}\text{Er}_{0.02}\text{F}_4$ UCNP composition, a 980 nm CW laser was used for excitation, and an 890 nm shortpass filter was placed in the collection path to allow the upconverted Er^{3+} emission at 550 and 660 nm to pass to the detectors while the 980 nm reflected excitation was blocked by the filter.

The beauty of this setup is that its sensitivity allows for single-particle measurements as well. UCNPs can be relatively easy to detect at the single-particle level, due to the nature of upconversion itself and the fact that they are orders of magnitude more efficient at upconversion than most other materials. This allows for a very high S/N ratio. Going back to the Yb^{3+} , Er^{3+} above, essentially any detected light at 550 or 660 nm will be coming from the UCNP. Thus the degree of cleanliness and rigor that more traditional single-particle studies require are not necessary in this case. Nonetheless, optimizing the system to detect single nanoparticles is still not *easy*, per se. Glass slides must be sonicated in a series of solvents (ethanol, acetone, ultrapure water) and then further cleaned with oxygen plasma to remove any organics on the glass. The proper concentration of UCNP solution must then be determined through trial and error, and spin-coated onto the cleaned glass slides so as to obtain a final density of UCNPs that is much less than one per diffraction limited laser spot. This ensures the imaging scan contains resolvable single particles.

The trick to measuring single UCNPs is to have the system aligned before trying to identify single particles. System alignment can be made much more facile by installing the pinhole and APD onto three-axes micrometer stages. The system can first be aligned to the laser light reflection on a piece of silicon. Once signal is detected, a dense film of UCNPs of the same composition as the desired singles should be placed onto the microscope. This will allow the arrangement of the system to the specific chromatic aberrations of the UCNP of interest (chromatic aberrations abound in strongly upconverting systems since excitation and emission wavelengths are typically far apart). After iterating through the positioning of the pinhole, APD, and focus to

optimize signal with the dense film, the single-particle density film should be placed on the microscope. Since APD and pinhole will already be located in nearly the ideal locations, only the focus need be adjusted. A large scan with the piezo stages, with fingers crossed to detect any number of counts (usually at very high excitation laser powers), followed by a zoom into the detected spot and further optimization of focus (followed sequentially by pinhole and APD position optimization) should yield a nice single-particle scan.

2.4.2 Confocal microscopy through brain tissue

Obviously, passing excitation and emitted light through a high-index, highly absorbing and scattering material such as mouse brain will make imaging more complicated. However, as mentioned above, one of the main benefits of upconversion for use in biological studies is the fact that biological tissue essentially does not upconvert light. Therefore background signal is very low. Furthermore, upconverters are typically excited in the near-infrared (NIR), and in the studies in this thesis, Tm^{3+} emission at 800 nm allowed detection to occur in the NIR as well. Since scattering scales as λ^{-4} , these longer wavelengths relative to the visible (where nearly all high-efficiency dye molecules emit) enable much more facile imaging through thick tissue specimens. The studies described in chapter 4 achieve 2 μm resolution through 2 mm of mouse brain.

In order to achieve these results, one must first have something to image. 5 μm square wells were microfabricated into a silicon wafer as described in Ch. 4. UCNPs were then dropcast into the wells, also described in Ch. 4. The fixed brain slice was placed on top of this micropillar array, and capped with a glass coverslip which stayed affixed through capillary action. Imaging was performed through the glass coverslip from the bottom, so that the brain slice was hanging upside down on the underside of the silicon microarray.

Similarly to measuring single particles, the microscope pinhole and APD alignment for imaging through the brain tissue was first optimized on part of the wafer not covered by brain. This not only achieved pinhole and APD alignment, but also positioned the focus relatively close to that required to go through brain. Because brain has a higher refractive index than air, the focus was then advanced when approaching to go through brain. Having the ordered array also helped with spatial alignment of the micro-adjusted sample stage. At this point, one just hopes it is a good day with the experimental stars aligned. Have fun with your brain!

2.5 Dye-sensitization of UCNPs

UCNPs were dye-functionalized in this study in a manner similar to that used in the original dye:UCNP work²⁵. However, some discrepancies should be noted. The key is to perform all dye-functionalization in a glovebox to ensure that the excess triplets created in the dye through proximity to the UCNP lanthanides do not oxidize the dye and render the system useless. Another key is to optimize the proper number of washing steps for each new batch of synthesized UCNPs. This is important, since the

amount of native ligand on the surface of the UCNP significantly affects the effectiveness of the dye-functionalization.

All dye functionalizations aimed to achieve a dye surface density on the UCNPs of ~ 1 dye/ 11 nm^2 . Thus the proper amount of the dye per UCNP for each functionalization was calculated with this in mind. The proper amount of UCNPs in toluene was then added to a micro-centrifuge tube, and to this was added 1.5 volume equivalents of dry ethanol. The mixture was centrifuged at $5000 g$, the supernatant removed, and the pellet resuspended in the original amount of dry toluene. This procedure was repeated twice more. The point of doing this is to reduce the amount of oleic acid in the system, and create a barer UCNP surface upon which to attach the dye. This will aid in dye functionalization through mass action. Because the substituting dye and oleic acid share a carboxylate functional attachment to the nanoparticle surface, mass action will be slow. Thus the reason to let the solution sit overnight. To alleviate this slow ligand exchange, the native UCNP ligand should be of L-type (e.g. amines, phosphines) while the dye functional moiety remains of X-type (carboxylates, phosphonates, etc.)¹⁹.

After the final centrifuge step, the dry pellet is not resuspended in toluene, but is brought into the glovebox dry. With the pellet, a film of the dye in a clean glass vial (proper amount for one functionalization) is also brought into the box. Inside the box, the dye is resuspended in chloroform while the UCNP pellet is suspended in toluene, and the two solutions are mixed and vortexed, all inside the box. (O_2 and H_2O levels inside the glovebox should be < 0.1 parts per million.) The final mixture is left in the box overnight to ensure proper dye-functionalization.

2.6 Time-gated photoluminescence

The bread and butter of this PhD, time-gated photoluminescence allowed us to measure a “dark” triplet state of the dye in order to verify that energy transfer was likely occurring via this triplet state. The main idea of gated luminescence measurements is to control the detection time relative to the excitation time. The two should not overlap, and should instead be separated by a delay much greater than the lifetime of the bright fluorescence states of the system of interest. In this way the detector and the scientist do not have to search for the proverbial needle in the haystack, since all of the fast and bright fluorescence will have dissipated before one even begins looking for the long-lived “dark” states. Thus it is more like looking for a needle in an empty barn: still difficult, but much more achievable.

The key components of such a system include the following: a chopper of some variety (I used a physical chopper wheel to ensure that when the excitation signal was blocked, it was fully off), a high-powered laser of the proper wavelength, a gateable detector, a time-synchronizing device, and of course the sample of interest (See Figure S.3.1).

Specifically, to this study, dye-functionalized NaGdF_4 nanoparticles were used to ensure no misleading lanthanide phosphorescence detection. They were functionalized akin to that in the section above, except that the toluene used to suspend the

nanoparticles had 5 mg/ mL polystyrene pre-dissolved into it. An N₂-atmosphere cryogenic sample chamber was brought into the glovebox, and the dye: NaGdF₄ solution was spin-cast onto a small silicon wafer with an ~100 nm SiO₂ layer on top. The film was then affixed to the cold finger of the cryogenic chamber (Linkam) with silver paste, and the chamber closed before being brought out of the box. It was then rushed down to the laser lab where it was quickly brought under N₂ atmosphere.

At this time, the sample can be cooled to cryogenic temperature to reduce non-radiative phonon-coupled losses of the triplet state. Once the system was optimized for singlet detection, the chopper and detector gating were activated using the time synchronizer (Quantum Composer) and the gating was slowly adjusted to reduce the singlet signal to background noise (~30 μs delay). As an aside, the room must be completely darkened, including computer monitors, and the detector, in this case an Excelitas APD should be covered adequately to achieve a dark count below 20 counts/s. Further aside, make sure the time synchronizer can sink the electrical current from the APD, or else a custom breadboard may be required with a voltage-dependent sink, as was required for these measurements. Contact the manufacturers for detailed requirements.

At this point, in order to measure the triplet spectrum, a monochromator set up in front of the APD was scanned across the expected wavelength range, with the APD cycling and integrating signal over two-minute cycle times per monochromator position. A custom script to control all of these various components proved extremely useful, and I thank Nicholas Borys and Ed Barnard immensely for their ScopeFoundry software.

Ultimately, measuring dark or nearly dark emissive states will be challenging. Key take aways include: (1) oxygen is your enemy, exclude it is all costs; (2) use as much laser power as you can without burning your sample; (3) when you use a chopper, make sure you use the highest ratio of on:off power as possible, in this study this was ∞ since a physical chopper brought the denominator to zero; (4) find smart people to help you when you get stuck; and (5) be patient!

2.7 Upconversion quantum yield

Upconversion quantum yield measurements also proved a seminal aspect of showing that the dye triplet state was indeed contributing to the energy transfer and not just a red herring. Measuring upconversion quantum yield of UCNPs is relatively straightforward, though special precautions must be made to ensure consistency and accuracy. For a very thorough explanation of an exact and trustworthy setup, see Stefan Fischer's works^{16,17}. In general, one must be mindful of the optical characteristics of every lens, filter, and cuvette being used, and these base spectra must be corrected for in order to measure absolute quantum yields.

External upconversion quantum yield (UCQY) was defined above in Equation 1.4. It is essentially the ratio of emitted photons at the desired upconverted wavelengths to absorbed excitation photons. As can be seen, UCQY cannot exceed 50% for a two-photon process, i.e. 980 nm → 550 nm for Er³⁺, or 33% for a three-photon process, etc.

The most challenging aspect of measuring UCQY accurately for non-sensitized UCNPs is accurately measuring the number of absorbed photons, because the absorption of UCNPs is so small. Thus it is recommended to use as high a concentration of UCNPs as possible when performing this measurement, such that the solution achieves an OD ~ 0.1 . To ensure such a high OD, if UCQY is known to be desired for a new batch of UCNPs, upon measuring the yield of a given synthesis, one can simply use the entire batch for the QY measurement, dissolved into $\sim 500 \mu\text{L}$.

The UCQY setup at the Molecular Foundry, where this work took place, consisted of the following. An integrating sphere coated with rough Teflon walls was used as the sample holder, to ensure many optical pass-throughs before detection. The sample was held in a $700 \mu\text{L}$ cylindrical quartz cuvette, capped with a push-in Teflon stopper. The excitation laser was coupled into the integrating sphere using optical fiber, and the collected light was also coupled out of the integrating sphere, at a 90° angle to the excitation port, using optical fiber. At the end of the collection fiber was installed a collimating lens to ensure proper coupling into the spectrometer used to measure either the emitted or transmitted photons. To ensure clean excitation with no side-bands, a narrow-band dielectric filter was placed in the excitation path prior to the integrating sphere.

Key measurements must be done prior to measuring at UCQY, and all obtained data properly corrected. The quantum efficiency of the detector to be used needs to be measured against a calibration lamp. Also, the transmission of every filter and lens to be used in the collection path needs to be measured.

When measuring a QY, essentially four spectra are taken for each QY measurement. To speed to process, it is ideal to have two identical sample cuvettes, one with the sample of interest, and the other with just neat solvent (or containing inert nanoparticles if contributions from sample scattering are a concern) to be used as a blank. The absorption of the excitation light should be measured for the both the sample and the blank, and the emission spectra of both the sample and blank need also be collected. For this work, the absorption was measured as the difference in transmission for the blank compared with the sample. The resultant QY is then calculated using Equation 3.1. To obtain a true QY, 3-5 separate QY's should be averaged.

Measuring the QY of dye-sensitized UCNP's can prove more difficult. In general, whenever a different excitation laser is to be used, the system needs to be completely re-optimized for the new wavelength. Furthermore, because the dye:UCNP system is air-sensitive, the filling of all QY cuvettes needs to be done in the glovebox, akin to taking triplet measurements, and then sealed with Teflon tape to ensure it is airtight. Because the dye absorbs so much more light than the UCNP, one must be cognizant not to concentrate the sample too much, or the absorption will influence the measured QY and will be artificially suppressed. In my experience, excess dye in the solutions seems to photobleach faster than dye attached to UCNPs, and so an uptick in QY is observed upon successive measurements of the same sample. Because different samples may photobleach more quickly than others for one reason or another, the first 2 QY

measurements of a given sample of dye:UCNPs seem to be the most accurate description for a particular sample.

As a last note, it should be mentioned that because upconversion is a nonlinear process with excitation power, the quantum yield responds in kind with excitation power. This can be summarized as follows. Upconversion using lanthanide ions occurs via real intermediate excited states within the lanthanides. As the excitation power increases, these intermediate states have a higher probability of being filled. It is essentially a kinetics problem, comparing the rate of impending photons onto the sample to the lifetime of the intermediate excited states. Once the probability that the intermediate states are filled approaches unity, upconversion essentially only needs one more photon in order for the process to occur, turning the two-photon process into a one-photon process, and dramatically increasing the QY. This is not a step function, however, but a continuous increase in UCQY with increasing intermediate state population. It is therefore imperative to report the excitation power used to measure the UCQY. For UCNPs it is not an intrinsic value, and UCQYs reported without this value should be viewed with caution.

3 Enrichment of molecular antenna triplets amplifies upconverting nanoparticle emission

3.1 Abstract

Efficient photon upconversion at low light intensities promises major advances in technologies spanning solar energy harvesting to deep-tissue biophotonics. Here, we discover the critical mechanisms that enable near-infrared (NIR) dye antennas to significantly enhance brightness and efficiency in lanthanide-doped upconverting nanoparticles (UCNP) systems, and leverage these findings to design dye-UCNP hybrids with a 33,000-fold increase in brightness and a 100-fold increase in quantum yield over bare UCNPs. We show that even photoactively-inert lanthanides in the UCNP substantially increase triplet state populations in the dye antennas, and the resultant triplet states then mediate energy transfer into the nanocrystals. Based on lifetime and quantum yield measurements, we find that increasing the Ln^{3+} content of the UCNP from 22 to 52% shifts the primary energy donor from singlet to triplet, with 2/3 of energy transfer originating from the triplet in higher- Ln^{3+} UCNPs. Time-gated phosphorescence, density functional theory, and triplet-quenching experiments support these findings. This interplay between the excited-state populations in organic antennas and the composition of UCNPs presents new design rules that overcome the limitations of previous upconverting materials, enabling performances now relevant for photovoltaics, biophotonics, and infrared detection.

3.2 Introduction

Photon upconversion, the process of combining multiple low-energy photons into a single higher-energy photon, underlies advanced optical technologies in solar light harvesting^{40,6,1} deep-tissue bioimaging^{41,42}, sensing⁴³, and optogenetics^{44,45}. Two multiphoton techniques, molecular triplet-triplet annihilation⁴⁶⁻⁴⁸ (TTA) and multistep absorption in lanthanide-doped upconverting nanoparticles (UCNPs) show exceptionally efficient anti-Stokes emission and each have specific advantages depending on wavelengths, fluences, and desired applications. The current study focuses on UCNP systems, capable of upconverting NIR light 5-6 orders of magnitude more efficiently than other nonlinear optical materials⁶. Consisting of an optically inert ceramic matrix doped with photoactive lanthanide ions such as Yb^{3+} and Er^{3+} , UCNPs take advantage of the long-lived intermediate-energy states within the lanthanide ions⁴⁹ to sequentially absorb multiple photons at low excitation intensities, enabling efficient anti-Stokes emission^{6,41,13,50}. Recent studies have shown that attachment of organic dye antennas to the UCNP surface dramatically increases their optical cross-sections and absorption bandwidths^{40,44,26,51,35,52}, potentially transforming a range of fields. However, the existing studies demonstrate either large emission enhancement⁴⁰ or increased upconverting efficiencies^{44,26,51,35} when dye antennas are attached to the UCNPs, but not both. This highlights a lack of general understanding surrounding the dye-nanocrystal interactions, which currently prevents their use in any practical applications.

In this work, we reveal that spin-triplet states in the dye antennas act as key intermediates in the sensitization of the UCNPs, and further, that lanthanide ions at the

UCNP surface enhance intersystem crossing (ISC) within the dye from the singlet (S_1) to triplet (T_1) excited states through the heavy atom effect, where $ISC \propto Z_{\text{eff}}^4$ (Fig. 1)⁵³. Leveraging the importance of dye triplet states and the influence that UCNP composition holds on their population, we produce sub-20 nm nanoparticles with upconverted emission greater than 4 orders of magnitude greater than that of non-sensitized UCNPs.

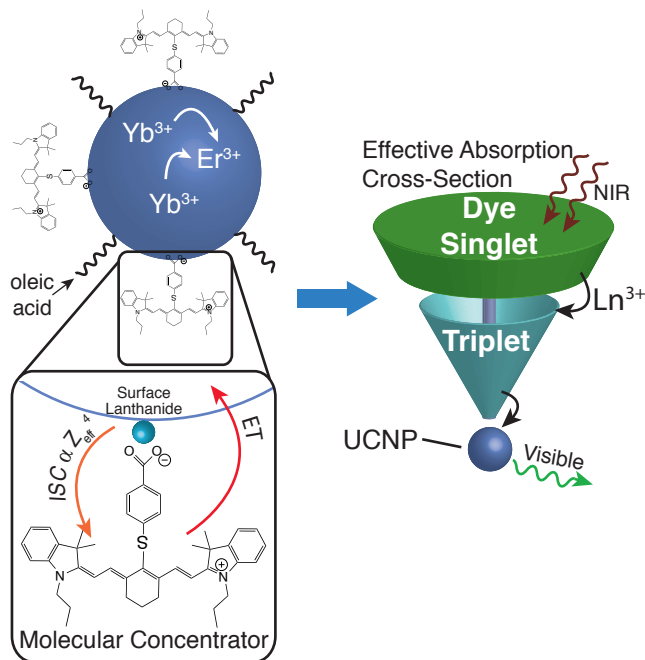


Figure 3.1. Dye-functionalized UCNPs, their mechanism of energy transfer, and the larger effective absorption cross-section of dyes relative to UCNPs.

(Top Left) A cartoon schematic of the dye-sensitized UCNP system, showing IR806 bound to the UCNP surface (not to scale), and an upconversion event inside the UCNP where two excited Yb^{3+} nonradiatively excite an Er^{3+} into a higher energetic state. (Bottom Left) A magnified illustration of the interactions between IR806 and a surface lanthanide—the heavy nucleus of the lanthanide aids in intersystem crossing (ISC) from IR806 $S_1 \rightarrow T_1$ states, allowing much more efficient T_1 sensitization of the Ln^{3+} atoms within the UCNP. (Right) A depiction of the antenna-like nature of IR806 in sensitizing the UCNP upconversion, conveying the much larger absorption cross-section of IR806 relative to the UCNP.

3.3 Evidence of a resonant triplet

We chose to investigate the means of energy transfer from the cyanine dye antenna IR806^{40,44,26,52}, which is commonly coupled to UCNPs despite the weak spectral overlap of its fluorescence with the absorption of the UCNP Yb^{3+} sensitizer (spectral overlap integral = 11%)^{40,26}. We used time-gated photoluminescence spectroscopy to search for a relatively dark lower-energy phosphorescent state of the dye that better

overlaps with Yb^{3+} absorption, potentially explaining efficient energy transfer. Thin films of IR806 in polystyrene cooled to 80 K yielded no detectable delayed luminescence. Recognizing that ISC to the triplet state could be enhanced by proximal lanthanides in the UCNP^{27–29,54}, we attached IR806 dyes to optically inert NaGdF_4 nanoparticles (i.e. no Yb^{3+} or Er^{3+}), a common host matrix for UCNPs with luminescent transitions only in the ultraviolet⁵⁵. Upon excitation at 791 nm, films of IR806- NaGdF_4 nanoparticles in polystyrene exhibit a long-lived peak centered at 981 nm, close to the 976 nm absorption maximum of the sensitizing Yb^{3+} transition $^2\text{F}_{7/2} \rightarrow ^2\text{F}_{5/2}$ (Fig. 2A and Supplementary Fig. 1). This spectrum was taken with a 10 μs delay relative to singlet emission ($\tau_{\text{singlet}} = 575$ ps), ensuring the signal originates from long-lived phosphorescence. Excitation spectroscopy confirms the presence of a lower energy state at 980 nm (Supplementary Figs. 2, 3). To confirm the origins of these emissions, we used time-dependent density functional theory (TD-DFT) to calculate vertical excitation energies for the T_1 state of IR806 in the range 0.9–1.2 eV, in close agreement with the experimentally determined value (Fig. 2B, Supplementary Table 1, Supplemental Methods). Interestingly, the ground state molecular configuration of IR806 suggests the sulfur bridge may facilitate triplet energy transfer, bringing the frontier π -orbital to within $\sim 3\text{--}7$ Å of the nanoparticle surface. The relevant transitions and energy transfer pathways in the dye-sensitized UCNP system (Figs. 2C–D) highlight the weak spectral overlap of the dye S_1 state with absorbing UCNP lanthanides and the direct overlap of the T_1 state with the Yb^{3+} and Er^{3+} absorption spectra.

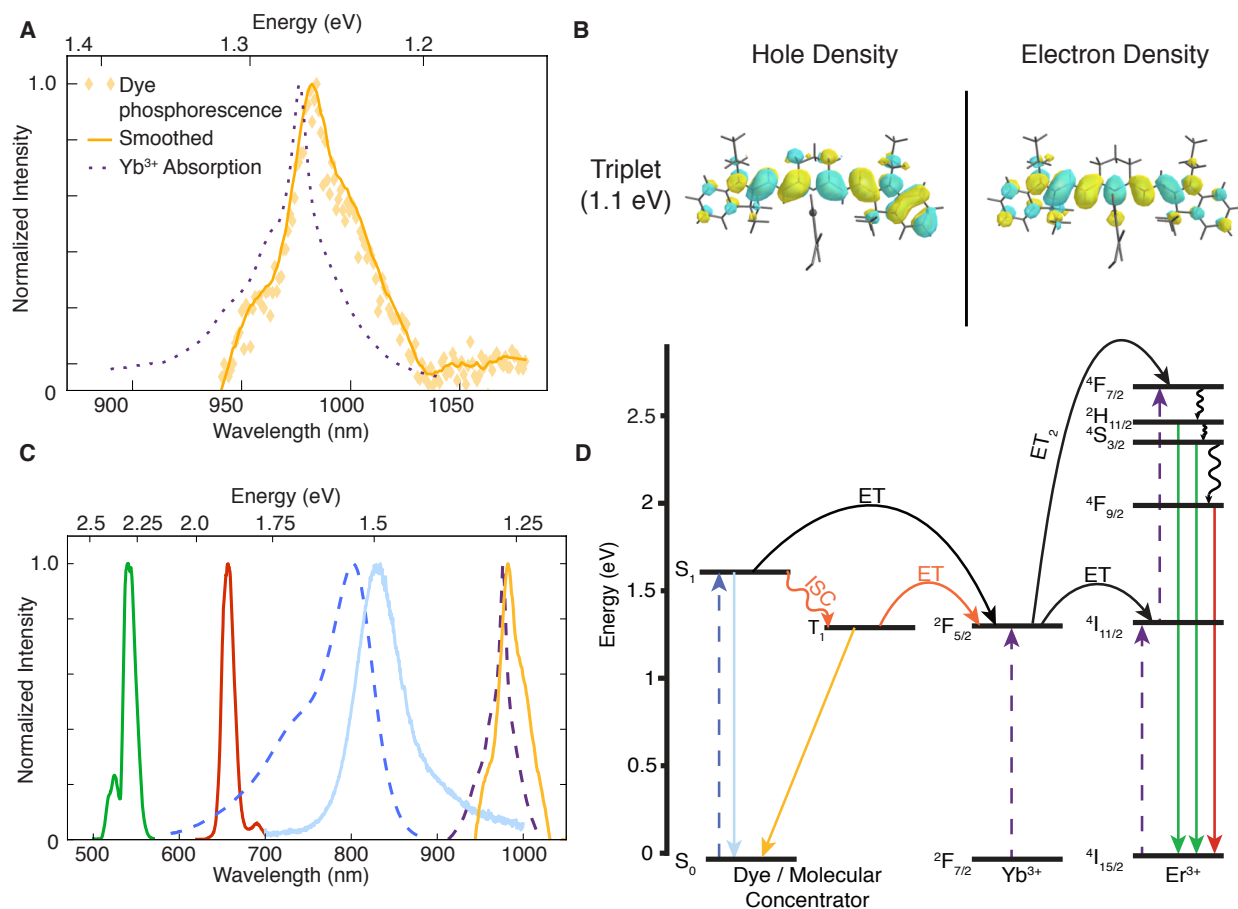


Figure 3.2. Time-gated photoluminescence as evidence of resonant triplet states. **a.** Time-gated triplet phosphorescence spectrum of IR806 on NaGdF₄ nanoparticles at 80 K (no Yb³⁺ or Er³⁺ present), overlaid with the NIR portion of the UCNP absorption spectrum (at room temperature). **b.** Electronic densities of the natural transition orbital (NTO) of the hole and the NTO of the electron for the first excited triplet state of IR806, calculated using TD-DFT. **c.** Spectra from left to right, colored according to their transitions in **d.** Er³⁺ emission (green and red curves), IR806 absorption (dashed blue curve), IR806 fluorescence (solid, light blue curve), UC, NP absorption (dashed purple curve) and IR806 phosphorescence (yellow curve) **D:** Jablonski diagram of proposed energy-transfer landscape, showing dye intersystem cross to the triplet state T₁ before transfer to UCNP lanthanides.

3.4 Enhancing triplet populations with photoactively-inert lanthanides

Based on this new understanding of the IR806 triplet manifold, we sought to modify the UCNP composition in order to rationally enhance the dye triplet population. While triplet states have been shown to transfer energy to and from nanoparticles^{56–61}, the concept of altering nanoparticle composition to increase the number of dye triplets, which in turn enhance energy transfer to and emission from the nanoparticle, has not

been described (See Fig. 1). We varied the heavy atom content by adjusting the ratio of Y^{3+} to Gd^{3+} ions, synthesizing ~ 12 nm UCNP with either 0% or 30% Gd^{3+} ($\beta\text{-NaY}_{0.78-x}\text{Gd}_x\text{Yb}_{0.2}\text{Er}_{0.02}\text{F}_4$), and functionalized these with IR806, prepared and sealed without water or O_2 (Supplementary Figs. 4-7 and Supplementary Methods). Neither Gd^{3+} nor Y^{3+} have optical transitions in the NIR or visible and thus do not directly participate in the photophysical transitions that give rise to NIR-to-visible upconversion⁶². For UCNPs with 0% Gd^{3+} , dye sensitization ($\lambda_{\text{ex}} = 808$ nm) enhances the upconverted emission intensity ~ 500 -fold over direct UCNP excitation ($\lambda_{\text{ex}} = 980$ nm) using the same excitation power density at both wavelengths (10^3 Wcm^{-2}), an enhancement similar to previous reports⁴⁰. Dye sensitization of the 30% Gd^{3+} UCNPs, however, enhances upconverted emission intensity $\sim 15,000$ -fold over direct UCNP excitation at the same excitation density. Thus by raising the Gd^{3+} content, we increase the spin-orbit coupling and ISC kinetics within the dye by increasing the average Z_{eff} of atoms on the UCNP surface^{27-29,54}, yielding an additional 30-fold enhancement in upconverted emission (Fig. 3a). These spectra were taken with 5 Wcm^{-2} excitation power density, highlighting the potency of using light antennas to lower the required excitation flux. Signal-to-noise analysis (Supplemental Methods) of Fig. 3a further shows that fluences less than 100 mWcm^{-2} can give measurable signal. This result demonstrates that in dye-sensitized UCNPs, the lanthanide composition may be optimized concurrently with dye sensitization to achieve maximum performance, due to the coupled nature of these systems.

3.5 Quantification of triplet energy sensitization of upconverting nanoparticles

To determine the extent to which UCNP lanthanide content influences IR806 photophysics, we measured sub-nanosecond singlet lifetimes of IR806 in the presence and absence of UCNPs (Fig. 3b). Free IR806 in solution has a characteristic singlet lifetime, τ_{F} , of 575 ps, yet bound to the surface of 0% Gd^{3+} UCNPs, it shortens by about half to 293 ps. This is indicative primarily of Förster Resonance Energy Transfer (FRET) from the dye singlet to Yb^{3+} , although with 22% lanthanide content, we believe a small amount of this decay is caused by ISC to the dye triplet state. When bound to the surface of 30% Gd^{3+} UCNPs, the IR806 singlet lifetime shortens even more to 173 ps. Because the Yb^{3+} and Er^{3+} content remains constant, this shortening of the singlet lifetime can be entirely attributed to intersystem crossing (ISC), suggesting the dye is not only close enough to the UCNP lanthanides for FRET, but close enough to be influenced by the heavy atom effect^{53,27-29,54} of UCNP Gd^{3+} nuclei. The increased heavy atom effect then increases ISC within the dye ~ 8 -fold, which is responsible for the shortened lifetime. We also note the absence of an unquenched component in the time-resolved emissions of the IR806-UCNP complexes, suggesting that free IR806 contributes little to their measured emission.

To further quantify the energy transfer contribution of these triplets into the UCNPs, and to verify that the triplet acts as an intermediate in sensitizing upconversion within the UCNPs, we sought to systematically quench energy transfer from the triplet manifold of the dye. The triplet quencher cyclooctatetraene (COT) was used as a molecule known to selectively scavenge excited state triplets in organic dyes because of its high-energy singlet state (4.39 eV) and low-lying triplet state (0.8 eV)⁶³⁻⁶⁵, enabling

COT to quench triplets without siphoning excited-state singlets. The upconverted quantum yield (UCQY) of dye-sensitized UCNPs was measured in the presence of increasing amounts of COT, and while UCNPs with 0% Gd³⁺ showed a decrease of UCQY by ~25%, UCNPs with 30% Gd³⁺ content showed a decrease of UCQY by ~65% (Fig. 3c). This not only provides compelling evidence that significant energy transfer to the UCNP occurs via molecular antenna triplets, but that lanthanide content within the UCNP influences ISC rates and thereby triplet populations.

These long-lived triplets are known to suffer from photooxidation by ambient water and reactive oxygen species⁶⁶, presenting a challenge for using dye-UCNP complexes. Changes in the steady-state absorption of dyes bound to UCNPs suggest that they are photocleaved in ambient atmosphere (Supplementary Fig. 8), as has been observed with other cyanine dyes⁶⁷, and we find that this photocleavage is enhanced when bound to the UCNP (Supplementary Fig. 9). Dispersions of IR806-UCNP conjugates prepared under N₂ are stable (Fig 3d), showing no measurable photodegradation after continuous excitation for 30 minutes. Encapsulation of IR806-UCNP films in polymer under N₂ (Supplemental Methods) leads to an order of magnitude increase in photostability over ambient films, and these polymers may be further optimized akin to methods used for preparing stable perovskite-based photovoltaic devices⁶⁸. These results provide further evidence that the heavy lanthanide ions on the UCNP surface enhance ISC rates and subsequent triplet populations within the dye, and highlight that isolation from O₂ and H₂O through encapsulation³⁵ is paramount to achieving long-term stability of dye-sensitized UCNPs.

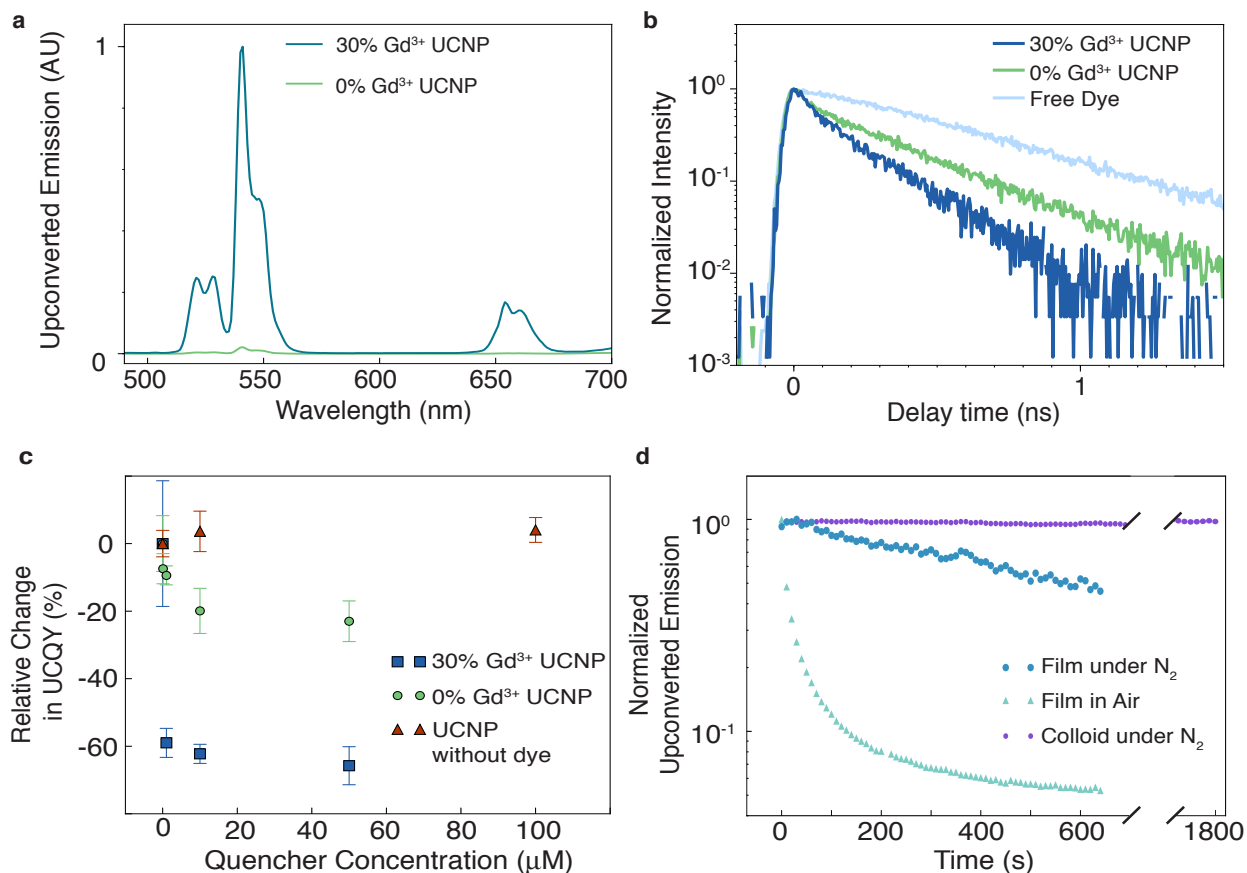


Figure 3.3. Evidence of triplet energy transfer to UCNPs. **a.** Upconverted emission from dye-sensitized UCNPs with 30% Gd^{3+} (blue line) and with 0% Gd^{3+} (green line). Excitation power $\sim 5 \text{ Wcm}^{-2}$. **b.** IR806 singlet emission lifetimes for free dye (top curve, $\tau = 575 \text{ ps}$), bound to 0% Gd^{3+} UCNPs (middle curve, $\tau = 293 \text{ ps}$), and bound to 30% Gd^{3+} UCNPs (bottom curve, $\tau = 173 \text{ ps}$). **c.** Relative change in UCQY of 30% Gd^{3+} (blue squares) and 0% Gd^{3+} IR806-UCNPs (green circles), as well as UCNPs without dye (orange triangles) as a function of the concentration of the triplet quencher COT. Error bars represent one standard deviation from the mean. **d.** Temporal photodegradation of upconversion from 30% Gd^{3+} IR806-UCNP films in air (light blue) or encapsulated under N_2 (dark blue), as well as a colloidal suspension in toluene under N_2 (purple).

3.6 Upconversion enhancement factor and quantum efficiency

We measured the upconverted emission of the 30% Gd^{3+} nanoparticles under a wide range of excitation densities, comparing excitation through the dye antennas with direct lanthanide excitation. Even at low powers ($\sim 1.8 \text{ Wcm}^{-2}$), upconverted emission is noticeable by eye when exciting the dye antennas, but not via direct UCNP excitation (Supplementary Fig. 10). Quantitatively, dye-sensitized upconverted emission is enhanced $\sim 33,000$ -fold over bare UCNPs (at 200 Wcm^{-2} excitation density, Fig. 4A, Supplementary Fig. 11), and if we take into account the broad molecular absorption

band of IR806 compared with the UCNP atomic transitions (Fig. 2C), the dye-UCNP system here could be $\sim 100,000$ -fold brighter than the bare UCNPs under broadband excitation⁴⁰. Importantly, this signal enhancement originates from the large absorption cross-section of the dye relative to lanthanides, as well as significant improvements in energy-transfer and upconversion efficiencies achieved by enriching molecular triplet states. This lowers the excitation intensity required to saturate the lanthanide intermediate energy states, promoting more efficient upconversion at lower powers. Maximizing this effect by capitalizing on both singlet and triplet energy transfer pathways is key to achieving optimal efficiencies while reducing input power.

Much of this enhancement is attributed to the increased efficiency of the dye-conjugated system, which we contrast to several other compositions in Fig. 4B. The UCQY of the 30% Gd³⁺ nanocrystals without dye is $0.06 \pm 0.01\%$ using direct 980 nm UCNP excitation at 10 Wcm^{-2} , in agreement with values reported elsewhere^{69,17}. The dye-sensitized UCQY, however, is measured to be $5.32 \pm 0.42\%$ under 800 nm dye excitation at 5 Wcm^{-2} , a ~ 100 -fold increase over the bare nanoparticles and comparable to bulk upconverting materials²¹. The UCQY of the dye-functionalized 0% Gd³⁺ system is $0.08 \pm 0.01\%$, almost two orders of magnitude lower and in agreement with previous reports⁴⁰. Interestingly, dye-functionalized UCNPs with 78% Gd³⁺ content (NaGd_{0.78}Yb_{0.2}Er_{0.02}F₄) show UCQY similar to that of 0% Gd³⁺ (See Fig. 4b), implying the system is more complex than simply maximizing ISC. This may have to do with the higher-energy states of Gd³⁺, which have been shown to transfer energy to and from other Ln³⁺ at higher fluences⁶².

Because of the nonlinear nature of the upconversion process, its efficiency increases with the excitation rate. The dyes, with absorption cross-sections $\sim 1000\times$ larger than UCNPs⁴⁰, function as molecular light concentrators, funneling orders of magnitude more excitation energy into the UCNP. This lowers the excitation intensity required to saturate the lanthanide intermediate energy states, promoting more efficient upconversion at lower powers. Maximizing this effect by capitalizing on both singlet and triplet energy transfer pathways is key to achieving optimal efficiencies while reducing input power, which eliminates a major impediment of using UCNPs for reducing phototoxicity in bioimaging or boosting solar cell efficiency^{6,1}.

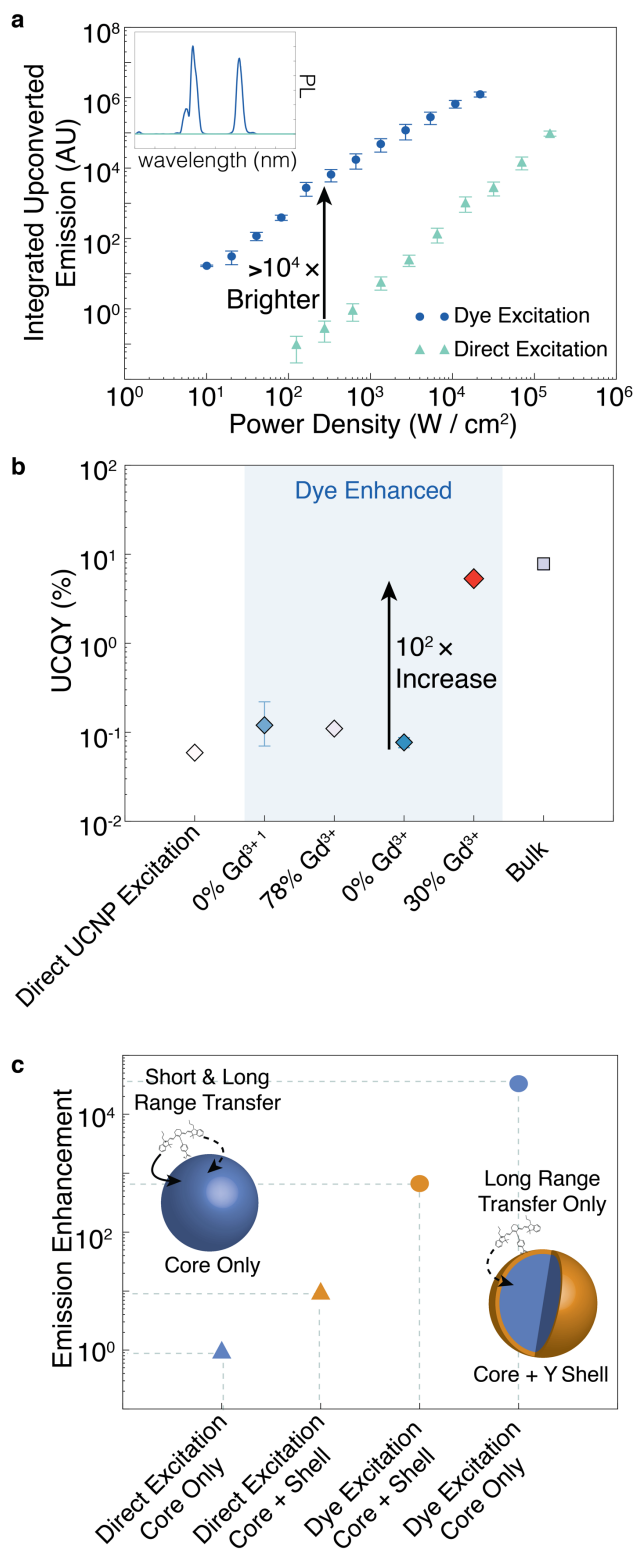


Figure 3.4. Upconverted performance improvements by enhancing dye triplet population. Excitation power dependence of upconverted emission from 30%

Gd³⁺ IR806-UCNP under excitation of the dye (dark blue; 808 nm excitation) or UCNP (light blue; 980 nm excitation). *Inset*: representative emission spectra for dye- or direct-excitation. Error bars represent one standard deviation from the mean. **b.** Quantum yields from (*left to right*) directly-excited 30% Gd³⁺ cores, dye-sensitized 0% Gd³⁺ value from literature⁴⁰, dye-sensitized 78% Gd³⁺ cores, dye-sensitized 0% Gd³⁺ cores, dye-sensitized 30% Gd³⁺ cores, and a bulk upconverting crystal²¹. Dye-sensitized UCQYs were measured at 5 Wcm⁻² excitation intensity. **c.** Emission enhancement from directly excited 30% Gd³⁺ cores (blue triangle), directly excited 20% Gd³⁺ cores coated with a 1.2 nm NaYF₄ shell (orange triangle), the same core-shell UCNPs but dye-sensitized (orange circle), and dye-sensitized 30% Gd³⁺ cores (blue circle).

3.7 Energy-transfer distance dependence

Finally, we gain further insight into energy transfer and enhancement mechanisms by comparing dye sensitization effects on core-only and core-shell UCNPs with the triplet enhancer Gd³⁺ (Fig. 4c). It is well-known that a thin inert shell enhances upconversion by passivating surface-related energy loss pathways^{49,17,70}. Dye-sensitization of these core-shell UCNPs produces additional upconversion enhancements that, while significant, are roughly 1 to 2 orders of magnitude less than what is achieved by dye-sensitizing the core-only 30% Gd³⁺ UCNPs. This discrepancy occurs despite the shell thickness (1.2 nm) being smaller than the dye-Yb³⁺ FRET distance of ~1.5 nm²⁶. Similar dye-sensitized enhancements are seen for other shell thicknesses, including NaGdF₄ shells (Supplementary Fig. 12). These results emphasize two key points. First, while longer-range resonant energy transfer from the singlet to the UCNP contributes to enhanced upconversion, other short-range (e.g., Dexter-like) pathways clearly contribute. Second, when adding a passivating shell, there is an inherent trade-off between reducing surface-related losses and eliminating short-range energy transfer processes. These conclusions highlight a potential avenue for further optimized systems based on more complex heterostructures and computational approaches^{44,26,51,35,71}.

3.8 Conclusions

We have demonstrated that triplet states in dye antennas critically affect the brightness and stability of dye-UCNP systems, revealing a clear strategy that overcomes the limitations of previous materials. We find that ISC within the dye is enhanced by spin-orbit coupling to lanthanide ions near the surface of the UCNPs and that this enriched triplet population is responsible for a significant amount of the energy transferred into the UCNP. Designing dyes whose excited state wavefunctions sit closer to the nanocrystals surface may further boost energy transfer by enhancing sub-nanometer processes such as spin-orbital coupling and Dexter electron transfer. Also, tuning the UCNP composition to higher active lanthanide content or heavier lanthanides such as Lu³⁺ may lead to further upconversion enhancements. Leveraging this nuanced mechanistic understanding results in superior dye-UCNP performance, which is now poised to drive improvements in solar energy conversion, infrared detection, and biological applications.

3.9 Materials and Methods

3.9.1 Materials

Sodium oleate, ammonium fluoride (anhydrous), oleic acid (OA, 90%), 1-octadecene (ODE, 90%), IR780 iodide, 4-mercaptobenzoic acid, poly(methyl methacrylate) (PMMA), cyclooctatetraene (COT), chloroform, hexanes, acetonitrile, dimethylformamide (DMF), trimethylamine (Et₃N), anhydrous ethanol (EtOH) and toluene were purchased from Sigma. Anhydrous lanthanide trichlorides were purchased from Strem.

3.9.2 Flask synthesis of core UCNPs

UCNPs were synthesized using air-free Schlenk techniques as reported previously⁷² with some modifications. For NaY_{0.48}Gd_{0.3}Yb_{0.2}Er_{0.02}F₄ UCNPs: to a dry 50-mL 3-neck flask, YCl₃ (192 μmol, 37.5 mg), YbCl₃ (80 μmol, 22 mg), ErCl₃ (8 μmol, 2.2 mg), and GdCl₃ (120 μmol, 32 mg) were added, followed by OA (3.25 g, 11.5 mmol) and ODE (4 mL). The flask was stirred, placed under vacuum and heated to 110 °C for 1 h, causing the solution to become clear. The flask was cooled and filled with N₂, and sodium oleate (1.25 mmol, 381 mg) and NH₄F (2 mmol, 74 mg) were added. The flask was again placed under vacuum and stirred at room temperature for 20 min, and then flushed 3 times with N₂. The reaction was heated to 315 °C, stirred for 45 min under N₂, and then cooled rapidly by a strong stream of air to the outside of the flask following removal of the heating mantle. When the reaction had cooled to 75 °C, EtOH (20 mL) and acetone (20 mL) were added to precipitate the nanocrystals. The reaction was transferred to a centrifuge tube and centrifuged at 3000 × *g* for 5 min to precipitate the nanocrystals completely. The supernatant was discarded and the white solid (~80 mg) was resuspended in minimal hexanes (5 mL) to break up the pellet. The nanocrystals were then precipitated again with addition of EtOH (45 mL) and centrifuged at 3000 × *g* for 5 min. The nanocrystals were resuspended and stored in 10 mL of hexanes with 0.2% (*v/v*) oleic acid to give a ~10 mM dispersion.

Because added Gd³⁺ typically yields smaller nanocrystals¹⁴, UCNPs with 30% Gd³⁺ content were grown at 320 °C.

3.9.3 Automated synthesis of UCNPs

The Workstation for Automated Nanomaterial Discovery and Analysis (WANDA) robot was sometimes used to explore the synthesis space⁷². When WANDA was used, the High-throughput Experimentation Robot for the Multiplexed Automation of Nanochemistry (HERMAN) robot was used to dispense solid materials. For NaY_{0.48}Gd_{0.2}Yb_{0.2}Er_{0.02}F₄ UCNPs: a precursor solution of Ln-oleate was prepared by adding YCl₃ (3.51 mmol, 685 mg), YbCl₃ (0.90 mmol, 252 mg), and ErCl₃ (0.090 mmol, 25 mg) to a 100 mL round-bottom flask. OA (24.4 g) and ODE (14.2 g) were added, and the solution was heated to 110 °C under vacuum while stirring, and held at this temperature for 1 h to form a homogenous clear solution. The solution was then cooled

to room temperature and brought under vacuum into an N₂ glovebox equipped with the WANDA robot. To each reaction vial were added solid sodium oleate (1.25 mmol, 380 mg) and NH₄F (2 mmol, 74 mg), using the HERMAN robot. This was followed by the Ln-oleate solution (4.38 g) and additional ODE (such that the total mass of ODE = 5.5 g). The reaction vials were heated using the WANDA reactor at 30 °C/min to temperatures of 280 – 330 °C and held at that temperature for 30-90 min. The reactors were cooled to 75 °C, after which 9 mL of EtOH was added to precipitate the nanoparticles. Cleaning was then performed analogously to flask synthesis.

3.9.4 Synthesis of core/shell UCNPs

NaYF₄ or NaGdF₄ shells were grown using a protocol adapted from Li *et al.*⁷³ Briefly, UCNP cores in hexanes were dried in a three-neck 50 mL round bottom flask using gentle N₂ flow. Dry UCNPs were dispersed in 4 mL of OA and 6 mL of ODE and stirred under vacuum at 70 °C for 1 hour. UCNPs were then heated under N₂ to 280°C. For NaYF₄ shells, sequential injections of 0.1 M yttrium oleate dissolved in 40% (*v/v*) OA in ODE and 0.4 M sodium trifluoroacetate in OA were performed every 15 min. For NaGdF₄ shells, 0.1 M gadolinium oleate dissolved in 40% (*v/v*) OA in ODE and 0.4 M sodium trifluoroacetate in OA were utilized. Lanthanide and sodium precursors were added in a 1:2 molar ratio. At the end of an injection series, the reaction mixture was kept at 280 °C for 30 min and then cooled with a stream of air until it reached room temperature before cleaning as described above.

3.9.5 Nanoparticle characterization

TEM was performed using a JEOL JEM-2100F field emission transmission electron microscope at an acceleration voltage of 200 kV. Size statistics were acquired for approximately 100 nanoparticles using ImageJ software from multiple High-Angle Annular Dark Field images. X-Ray diffraction (XRD) measurements were performed using a Bruker D8 Discover diffractometer with Cu K α radiation.

3.9.6 Synthesis of IR806

In a glass vial, IR780 iodide (26 mg, 39 μ mol), 4-mercaptobenzoic acid (12 mg, 76 μ mol), and Et₃N (12 μ L, 86 μ mol) were dissolved in 1 mL of dry DMF, and the reaction was stirred at room temperature overnight under N₂. Purification by high-performance liquid chromatography (Varian) on a C₁₈ column using a linear gradient of 70 - 100% CH₃CN over 30 minutes gave product eluting at 22 min (84% CH₃CN). NMR (500 MHz, CD₃OD): δ 8.72 (d, 2H, *J* = 2.8 Hz), 7.91 (d, 2H, *J* = 1.8 Hz), 7.43-7.24 (m, 10H), 6.32 (d, 2H, *J* = 3.3 Hz), 4.11 (t, 4H, *J* = 0.9 Hz), 2.79 (m, 4H), 2.05 (m, 2H), 1.85 (q, 4H, *J* = 1.1 Hz), 2.15 (s, 12H), 1.02 (t, 6H, *J* = 1.0 Hz). MS for C₄₃H₄₉N₂O₂S⁺ calculated: 657.9; found: 658.4.

3.9.7 Functionalization of UCNPs with IR806

IR806 carboxylates are likely to exchange with surface oleates via mass action^{19,74}, occurring through a two-step X-type ligand exchange, whereby a proton from the substituting ligand is donated to the substituted ligand, which maintains charge neutrality in the nonpolar solvent. In a typical procedure, 2.7 μ L of 7 mM IR806 in

CHCl_3 was added to an empty vial and the CHCl_3 was allowed to evaporate. In a separate microcentrifuge tube, 85 μL of a 5 μM 13-nm UCNP dispersion in toluene were precipitated with excess EtOH and centrifuged. This process was then repeated after resuspension in toluene, and the UCNP pellet in the microcentrifuge tube, along with the vial containing the dried dye were brought into an N_2 glovebox. The nanoparticle pellet was resuspended in anhydrous toluene, the dye resuspended in anhydrous CHCl_3 , and the UCNP dispersion added to the vial containing the dye. The mixture was vortexed briefly and kept in the glovebox overnight, and the IR806-UCNP was used without further purification. For variously sized nanoparticles, the total surface area of UCNP was calculated and a surface density of ~ 1 IR806 molecule per 11 nm^2 was used to functionalize the UCNPs.

3.9.8 IR806-UCNP film encapsulation

After dye-functionalization of the UCNPs, encapsulation was achieved by suspending the IR806-UCNPs in a toluene solution of 5% (*m/v*) polystyrene (Sigma) and spin-coating the resulting suspension at 1000 rpm onto a silicon wafer with a 250 nm SiO_x top layer. A ring of UV-curable epoxy resin (Epotek 3035B) was then applied to the film, a glass coverslip pressed onto the ring to form a seal, and the polymer was cured using a UV lamp, with a small piece of foil shading the film to prevent photo-damage from the lamp. This entire procedure was done inside an N_2 glovebox.

3.9.9 Absorption measurements

All absorption measurements were performed in solution through a quartz cuvette (Starna) using an Agilent Cary Series UV-vis-NIR spectrometer.

3.9.10 Steady-state Fluorescence Measurements

Steady-state fluorescence were obtained with a back-illuminated silicon electron-multiplied CCD chip detector (Andor iXON, model # DU-897E-CSO; QE $\sim 17\%$ at 980nm) calibrated with a NIST-certified calibration lamp.

3.9.11 Theoretical calculations

Vertical excitation energies and natural transition orbitals⁷⁵ (NTOs) were calculated in Q-Chem utilizing time-dependent density functional theory (TDDFT), the B3LYP exchange-correlation functional, and a VTZ basis set, with solvation effects treated with the ptSS and ptLR polarizable continuum models^{76,77}. The lowest lying bright singlet and first triplet transitions are both dominated by π - π^* HOMO to LUMO transitions, and the molecule belongs to the cyanine family of dyes whose singlet excitations have been challenging^{78,79} to capture with theory. DFT geometry optimization at the B3LYP/VTZ level of theory, performed with two possible initial geometries, yielded two molecular configurations which are pictured below and were of nearly identical energy. The total SCF ground state energy difference at the B3LYP level was 0.08 eV, with the second pictured molecule in the table below having the lower energy. The effect of the choice of the exchange correlation functional (XCF) was explored and, with the Tamm Dancoff approximation (TDA), yielded triplet energies

between 0.9 and 1.2 eV. The effect of the TDA was significant in some cases, and its energies are likely more accurate⁸⁰. These results are summarized in Table S1.

3.9.12 Upconverted emission measurements

For direct UCNP excitation, a dispersion of UCNPs was added to a sealed quartz cuvette (Starna) and placed on an inverted confocal microscope (Nikon). A 980-nm laser (Thorlabs) is directed into the back aperture of a 0.6 NA 40× Objective (Nikon), and focused through the polished bottom of the cuvette. Emitted light is collected back through the same objective, filtered by two 700-nm short-pass (SP) filters and routed to an LN₂-cooled CCD spectrometer (Princeton Instruments). For dye excitation, an 808 nm laser was used (CrystalLaser). All IR806-UCNP dispersions were handled in an N₂ glovebox from the moment of mixing the dye with the UCNPs through to measurements in the sealed quartz cuvette under N₂. To obtain the power dependence measurements of Figure 4, a continuously variable neutral density wheel was used, and turned by an Arduino-controlled rotator. Powers were read by a Thorlabs power meter simultaneously by using a glass coverslip to reflect 5% of the incoming flux.

For the spectra shown in Fig. 3a, an excitation fluence of 5 W cm⁻² was used, and signal was collected using a Hamamatsu photomultiplier tube (PMT) with a wide spectral response (model R928). The 30% Gd³⁺ spectrum has a maximum intensity that is >4660 times larger than the measured noise floor of the detector (dominated by dark current). Conservatively assuming a quadratic dependence of upconverted emission on excitation fluence, this implies that signal levels larger than the noise floor are expected to be detected for excitation intensities of $(5/(4660)^{0.5})$ Wcm⁻²; i.e., <100 mW cm⁻².

3.9.13 Time-gated triplet phosphorescence measurement

The triplet spectrum was measured on a modern setup modeled after the phosphorimeters of the past century, in which excitation light is blocked while emitted light from the sample is being collected, in order to only collect long-lifetime emission events (Figure S4). A Chameleon Ti:Sapphire tunable laser from Coherent was used as the excitation source. The laser wavelength was tuned to 791 nm in the fundamental beam (2.8 mW CW power). A physical optical chopper was used at a frequency of 500 Hz to ensure the laser was completely attenuated during “off” times. The chopper was controlled by a central delay pulse generator (Quantum Composer) which was also used to modulate the avalanche photodiode (APD, Excelitas SPCM-AQRH) on and off out of phase with the chopper, with an 8-μs delay between the chopper and the APD. The sample was made akin to the encapsulation technique using NaGdF₄ UCNPs with no Yb³⁺ or Er³⁺ to exclude the possibility of long-lived lanthanide phosphorescence. However, after spin-coating the IR806-UCNP/ polystyrene suspension onto the Si wafer, it was not encapsulated with UV-curable polymer, but instead was attached to the cold finger of a cryogenic microscope stage (Linkam Scientific) inside the glovebox using silver paste to ensure thermal conductivity (Perkin Elmer), and cooled to 80 K using liquid N₂. Two 808 longpass filters were placed in the emission path (Semrock 808LP RazorEdge). The APD was set up behind a monochromator and the monochromator swept from 800 nm to 1020 nm. Each 0.5 nm position of the monochromator was

integrated for 20 seconds. A blank sample of NaGdF₄ UCNP with no dye was also measured to ensure no Yb³⁺ or Er³⁺ contribution, and was subtracted out of the peak shown in Fig 2A.

3.9.14 Two-photon Excitation Spectrum

To further elucidate the presence of a lower-lying triplet state, an excitation spectrum of the dye film was taken. IR806 dye was mixed with a 5 mg/mL solution of PMMA in toluene in a N₂ glovebox, and spun onto a Si wafer with a 100nm SiO_x top layer. The wafer was quickly placed under vacuum, attached to the cold finger of a cryostat (Janis ST-500) with silver paste. The sample was cooled to 77K. The same Ti:Sapphire laser as above was used, and the excitation wavelength was scanned from 910 - 1040nm. Two 850SP dichroic filters (ThorLabs) were placed in the emission path of the microscope, and a 900LP (Semrock) filter was placed in the excitation path to ensure no high-energy features of the laser could pass. An Andor iXon EMCCD camera was used to collect the spectra, with 2 second integrations and the binning set to 4. Singlet emission from 700-850nm was integrated for each excitation wavelength, and forward and back sweeps were averaged to obtain the spectrum shown below.

To obtain the power dependence of the shoulder feature, the laser wavelength was fixed near the excitation spectrum's peak at 980 nm, while the power was tuned across approximately 1.5 orders of magnitude. Each point represents a singlet emission spectrum integrated as above from 700 – 850nm. The blue points represent both the forward and back scans. The green line has a slope equal to 1.84, clearly showing the two-photon dependence inherent with this feature.

3.9.15 Singlet Lifetime Measurements

Singlet lifetimes were measured using a supercontinuum laser () whose wavelength was tuned with an acousto-optic tunable filter (AOTF, Gooch and Housego) to 693 nm, exciting the high-energy tail of the IR806 singlet absorption feature. A 740 LP dichroic filter (ThorLabs) was placed in the emission path of the microscope to block any reflected laser light. Approximately 1 μW of laser power was focused using a long-working-distance objective (Nikon Super Plan Fluor 40x, 0.6 NA, 2.8 mm WD) into a sealed quartz cuvette (Starna) containing the relevant dye or IR806-UCNP dispersion, sealed in an N₂ glovebox as above. Emission was collected using a single-photon avalanche photodiode (MPD PDM) with <50 ps timing resolution, connected to a time-correlated single-photon detector (Picoquant) with 4 ps resolution. Samples were diluted ~100x relative to the concentrations used in the upconverted emission measurements. Data were fitted using single exponential fits over the first 1 ns of decay. Single exponentials were used to elucidate the average decay behavior, and are unaffected by instrument response (~40 ps).

3.9.16 Quantum yield measurements

To determine the upconversion quantum yields (UCQYs), 500 μL of a UCNP dispersion in toluene was placed in a quartz cuvette with a Teflon cap, sealed with Teflon tape, and placed in an integrating sphere (Horiba Jobin-Yvon) for the Fluorolog-3 spectrometer. Unfunctionalized UCNP UCQY measurements were performed under ambient atmosphere. IR806-UCNPs were dispersed in anhydrous toluene, sealed in an

N_2 -glovebox and wrapped with Teflon tape before removing from the box. The light paths between the excitation laser (Sheaumann, 976 nm, 1 W for bare UCNPs, Hi-tech Optoelectronics Co., 800 nm for IR806-UCNPs), integrating sphere, and the spectrometer were routed using fiber optic bundles (Fiberoptic Systems, Inc). For each sample, the emission was measured from 510 to 680 nm. The unabsorbed laser radiation (excitation spectrum) was measured at the detector from 970 to 984 nm for bare UCNPs, or 794-804 nm for IR806-UCNPs. For IR806-UCNPs an 808 nm notch filter (Semrock) was used to attenuate the laser light so as not to saturate the detector. Pure toluene was used to record blank excitation and emission spectra. Excitation and emission spectra were corrected for the sensitivity of the detector over the appropriate wavelengths using a NIST-traceable calibrated light source (Avantes Avalight HAL-CAL) with the same integrating sphere, fiber optic setup, detector, and spectrometer settings. Excitation spectra were also corrected using the transmission spectrum of the 808 nm notch filter. Reported UCQYs are the result of five UCQY measurements for each sample that have been averaged. Occasionally, ‘ripening’ of the QY was observed for dye-sensitized samples, meaning recorded UCQY measurements showed an appreciable increase in QY upon successive measurements. This is attributed to both a decrease in absorption and increase in emission, the causes of which are currently unknown. Each UCQY measurement was calculated using the four intensity values as follows:

$$UCQY = (I_{em, sample} - I_{em, blank}) \div (I_{ex, blank} - I_{ex, sample})$$

where I_{em} represents the integrated emission from 510 - 680 nm, and I_{ex} represents the transmitted laser radiation, integrated from 970 - 984 nm (794 - 804 nm for dye excitation).

Any IR806 unbound to the UCNPs may reduce observed UCQYs through an inner filter effect, by absorbing incident light without transferring that energy into the nanoparticle (i.e. the real UCQYs may be larger than what we report). The absence of an unquenched component in IR806-UCNP singlet lifetime data (Fig. 3b) suggests the free dye contribution is minor, so any reductions in UCQYs are also likely to be minor.

3.9.17 Cyclooctatetraene Experiments

To obtain the cyclooctatetraene (COT) dependences in Fig. 3a, IR806-UCNP samples were prepared as above in a N_2 glovebox. A fresh bottle of COT (Sigma) was brought into the glovebox and stored there. The IR806-UCNP sample (or in the case of the control, UCNP sample) was diluted five-fold such that a 50 μ L aliquot of the same sample could be used for all COT concentrations within a single experiment. Because of photodegradation of COT, only two UCQY measurements were averaged for each sample. Toluene mixed with the appropriate amount of COT was used to record blank excitation and emission spectra.

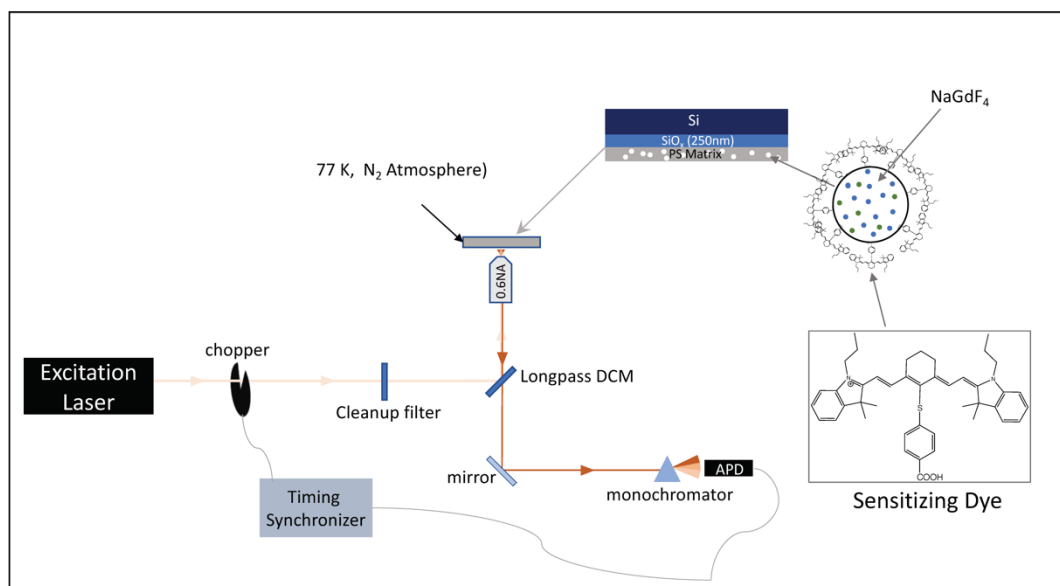


Figure S.3.1. Cartoon schematic of time-gated triplet phosphorescence setup.

See Section 3.9.12 for experimental details.

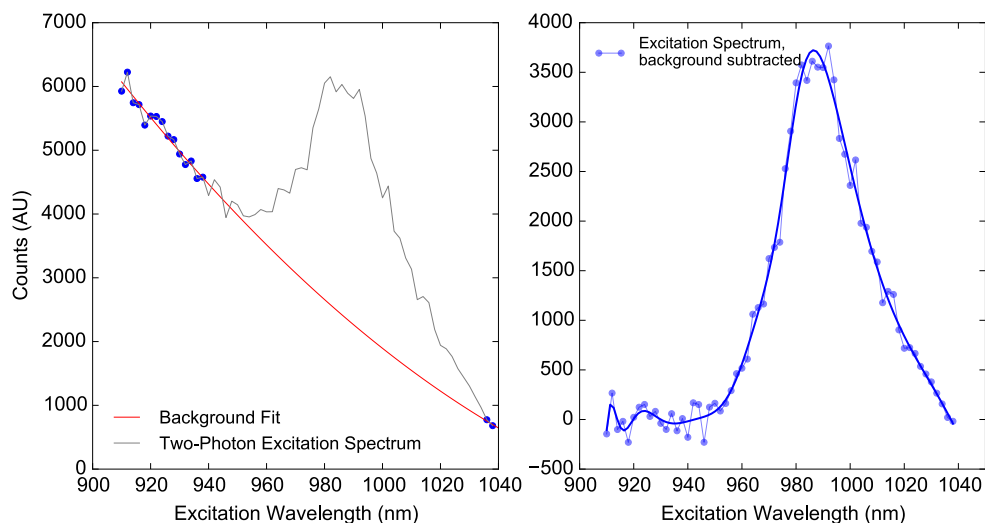


Figure S.3.2. IR806 Two-photon Action Spectrum

(*Left*) Two-photon action spectrum of IR806 film under vacuum and cooled to 77K. The measurement was taken by integrating IR806 singlet emission (700 - 850 nm) while sweeping the excitation wavelength from 900 – 1040 nm. Blue dots represent data points used to calculate the background signal (red line), attributed to absorption through the low-energy tail vibronics of the S_1 state. The background was fitted to a double polynomial. (*Right*) Background-subtracted two-photon action spectrum of IR806 (blue dots) and smoothed curve (blue line). This shoulder feature is attributed to two-photon excitation of the singlet state through exciting the dye T_1 state as an intermediate.

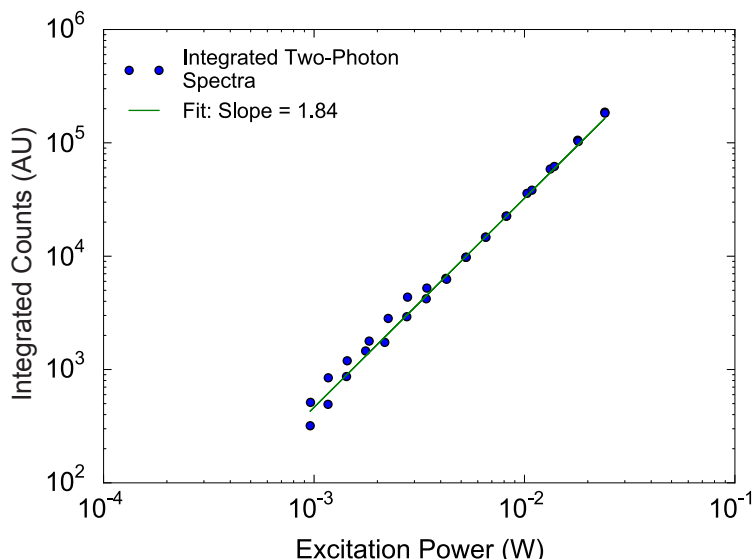


Figure S.3.3. IR806 two-photon action spectrum power dependence.

The excitation wavelength was fixed at 980 nm, near the peak intensity of the shoulder feature in Supplementary Figure 2, and the integrated emission measured from 700 – 850 nm. The laser power was varied across ~ 1.5 orders of magnitude. Data points are both the forward and back scans in power. Fitted green line slope is 1.84, showing the two-photon dependence inherent with this feature.

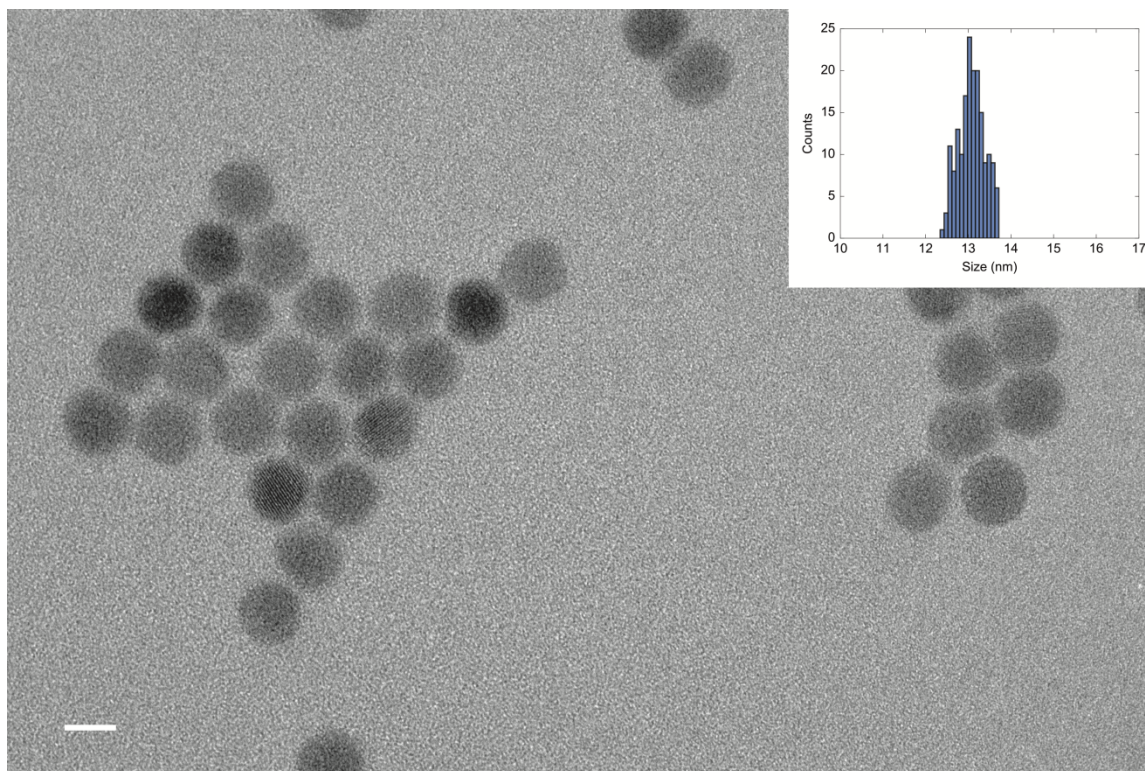


Figure S.3.4. Representative transmission electron micrograph of $\text{NaY}_{0.48}\text{Gd}_{0.3}\text{Yb}_{0.2}\text{Er}_{0.02}\text{F}_4$ nanocrystals.

Scale bar = 10 nm. Inset: size histogram, measured with ImageJ software from multiple High-Angle Annular Dark Field electron microscope images to improve the Z-contrast for automated sizing. Average size is 13.1 ± 1.0 nm.

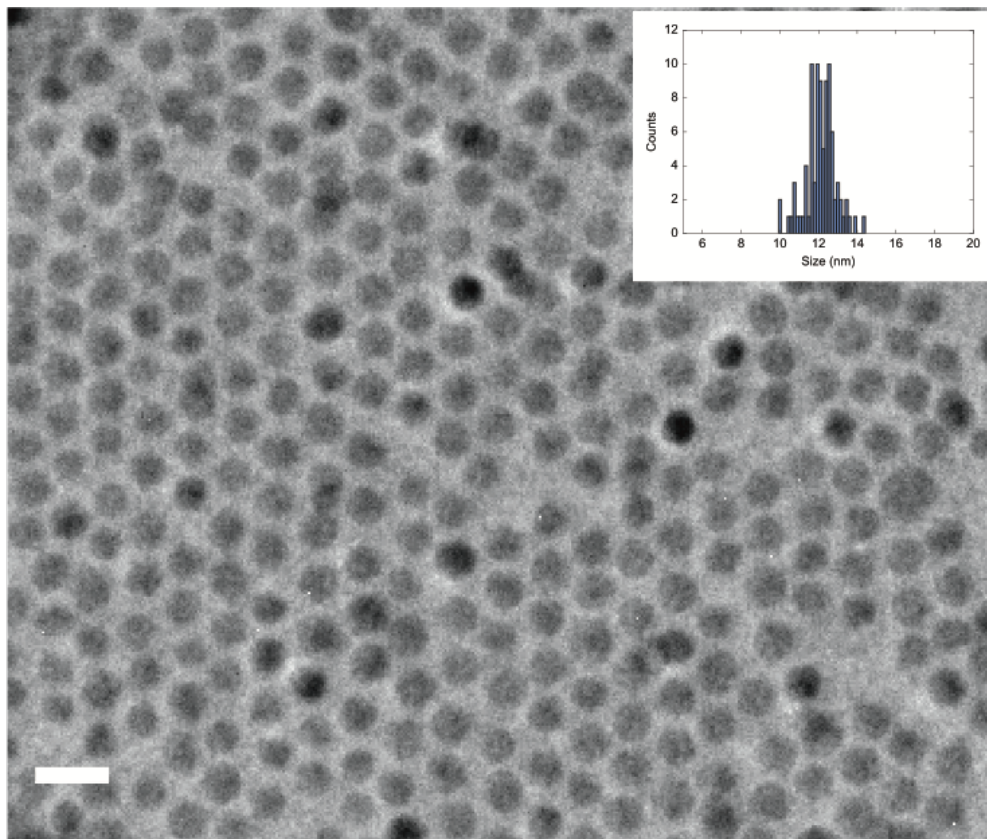


Figure S.3.5. Representative transmission electron micrograph of $\text{NaY}_{0.78}\text{Yb}_{0.2}\text{Er}_{0.02}\text{F}_4$ nanocrystals.

Scale bar = 20 nm. Inset: size histogram, measured with ImageJ software from multiple High-Angle Annular Dark Field electron microscope images to improve the Z-contrast for automated sizing. Average size is 12.1 ± 0.8 nm.

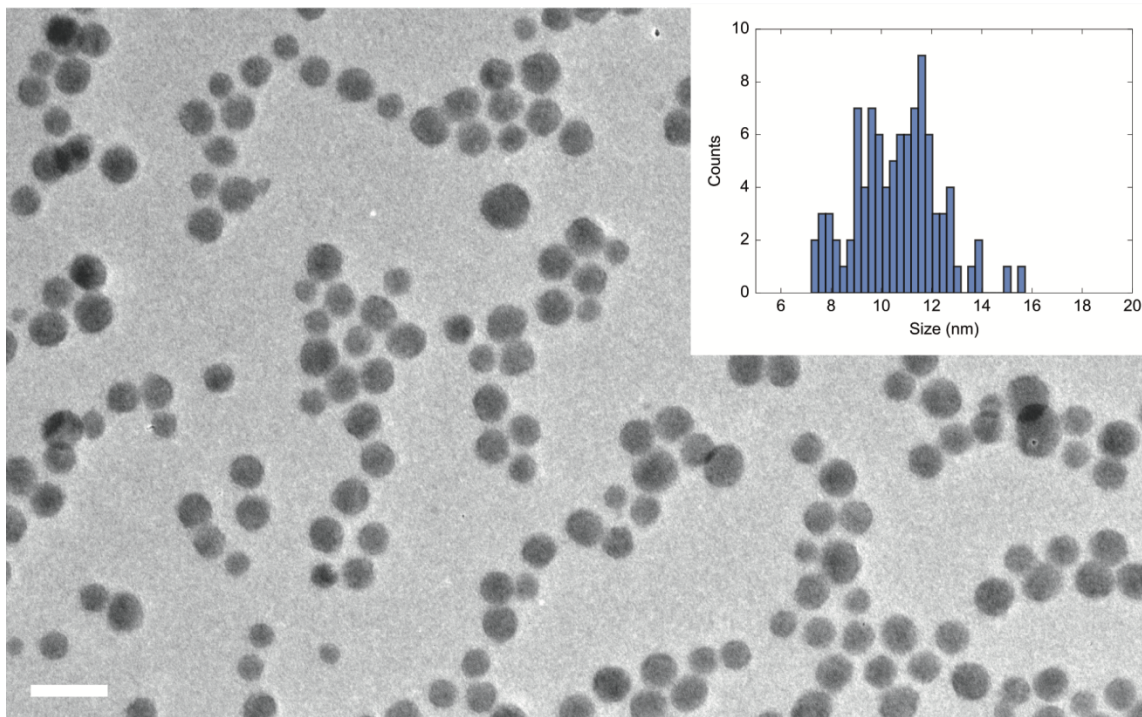


Figure S.3.6. Representative transmission electron micrograph of $\text{NaGd}_{0.78}\text{Yb}_{0.2}\text{Er}_{0.02}\text{F}_4$ nanocrystals.

Scale bar = 20 nm. Inset: size histogram, measured with ImageJ software from multiple High-Angle Annular Dark Field electron microscope images to improve the Z-contrast for automated sizing. Average size is 10.6 ± 1.7 nm.

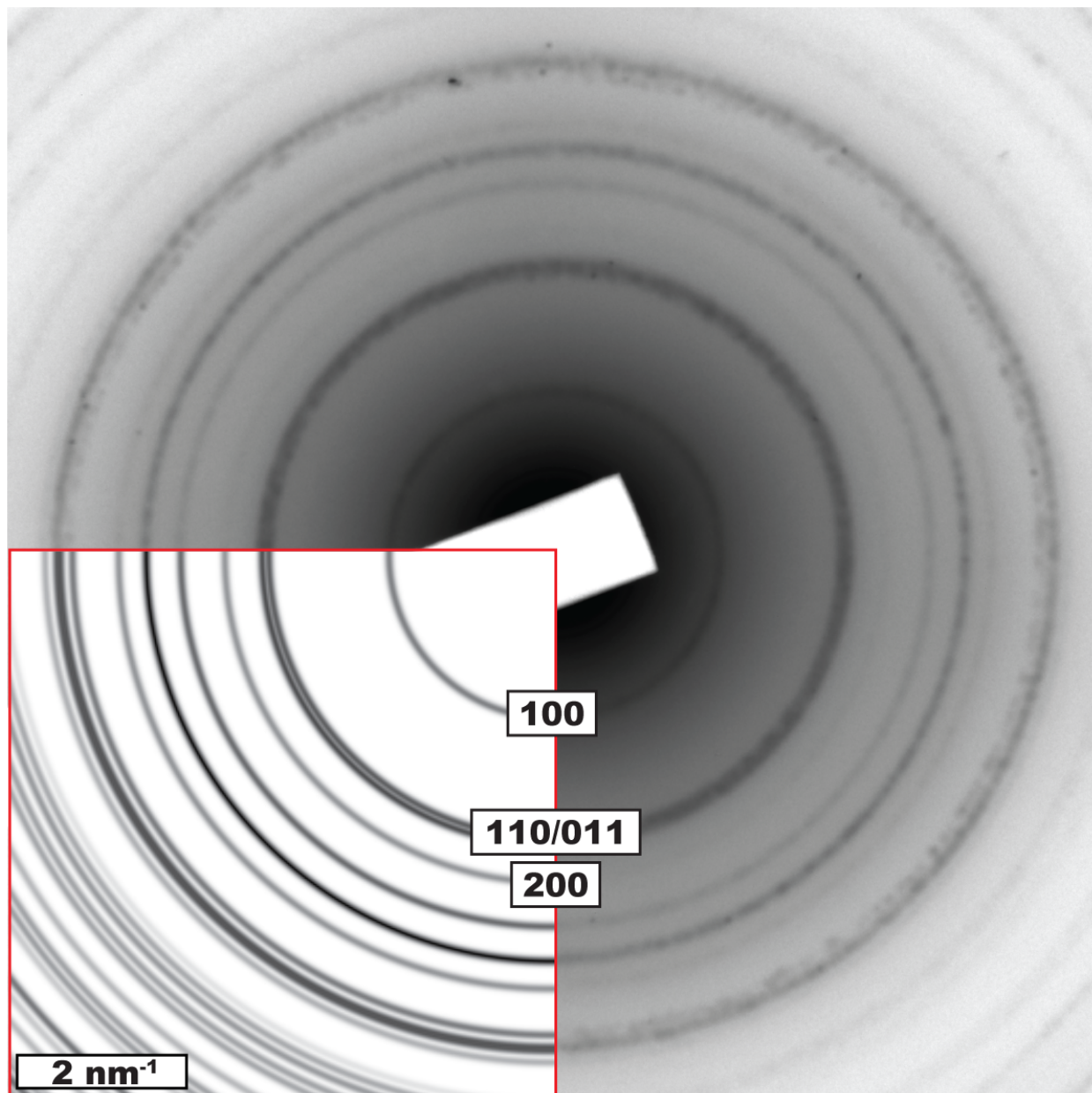


Figure S.3.7. Representative diffraction pattern of UCNPs

Pattern taken with a parallel electron beam of $1 \mu\text{m}$ diameter over a dense region of UCNPs. Inset shows kinematic simulation calculated with CrystalMaker software. The pattern shows 100% β -phase NaYF_4 crystal structure.

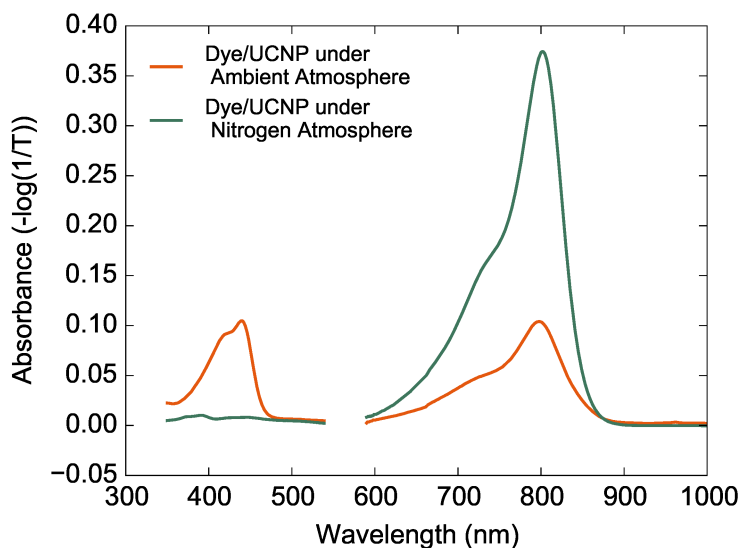


Figure S.3.8. IR806-UCNP steady-state stability in air

Absorbance spectra of NaGdF₄ nanoparticles dye functionalized in the glovebox (green line) or in air (orange line). When the functionalization was performed in air, the dye undergoes a rapid and visible color change from blue green to orange. However, when functionalized in an inert N₂ glovebox, the dye color remains stable.

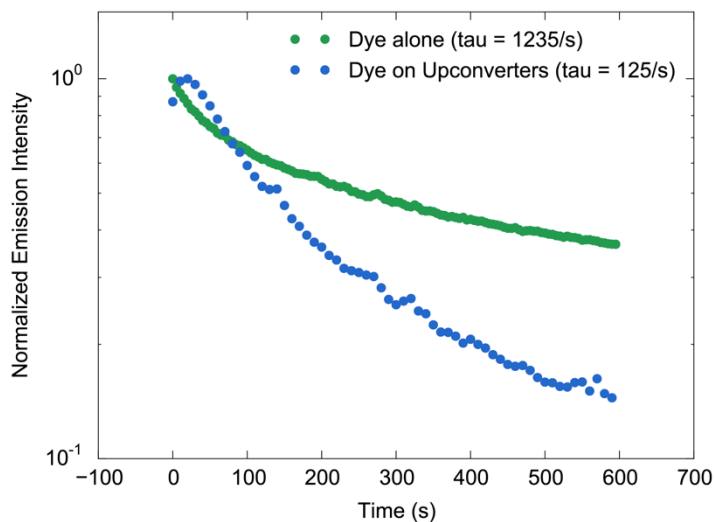


Figure S.3.9. IR806-UCNP Dynamic Stability

Films of IR806-UCNPs were made akin to the films in time-gated triplet phosphorescence measurements, but were left at room temperature instead of cooling to cryogenic temperatures. For the air studies the cryostat was opened to air. A series of emissions from a film of IR806-NaGdF₄ prepared in a glovebox was measured in a system analogous to upconverted emission measurements, where the spectrometer recorded one spectrum after another. Data was then condensed to a single point by integrating each emission spectrum from 500 - 700 nm. Emission from a film of the dye on and off the NaGdF₄ nanoparticles reveals the IR806-Gd³⁺ conjugate photobleaches an order of magnitude faster than the dye alone.



Figure S.3.10. Visible upconverted emission at low excitation flux.

A solution of IR806-functionalized $\text{NaY}_{0.48}\text{Gd}_{0.3}\text{Yb}_{0.2}\text{Er}_{0.02}\text{F}_4$ UCNPs under N_2 atmosphere in a Starna fluorescence 18F-Q-10-GL14-C quartz cuvette (path length 2mm). The images were taken with the camera of an Apple iPhone 7—Right: excited with 1.8 Wcm^{-2} 808nm collimated laser light, and Left: excited with 1.8 Wcm^{-2} 980nm collimated laser light. As can be seen, visible upconverted emission is clearly visible when exciting the dye antennae, but not when exciting the UCNPs directly.

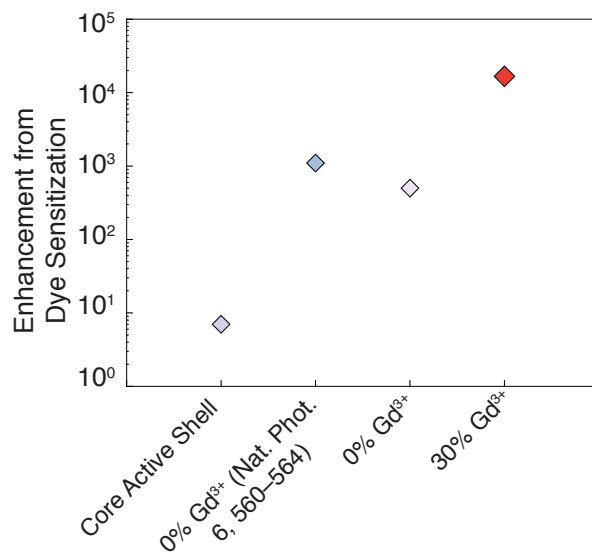


Figure S.3.11. Brightness enhancement from dye sensitization

Comparison of brightness enhancements from dye excitation divided by direct nanoparticle excitation: dye-sensitized $\beta\text{-NaY}_{0.78}\text{Yb}_{0.2}\text{Er}_{0.02}\text{F}_4$ @ $\beta\text{-NaY}_{0.9}\text{Yb}_{0.1}\text{F}_4$ (Core Active Shell)²⁶, dye-sensitized $\beta\text{-NaY}_{0.78}\text{Yb}_{0.2}\text{Er}_{0.02}\text{F}_4$ cores (0% Gd³⁺ (Nat. Phot. 6, 560-564))²⁵, dye-sensitized $\beta\text{-NaY}_{0.78}\text{Yb}_{0.2}\text{Er}_{0.02}\text{F}_4$ cores (0% Gd³⁺), and dye-sensitized $\beta\text{-NaY}_{0.78}\text{Gd}_{0.3}\text{Yb}_{0.2}\text{Er}_{0.02}\text{F}_4$ cores (30% Gd³⁺).

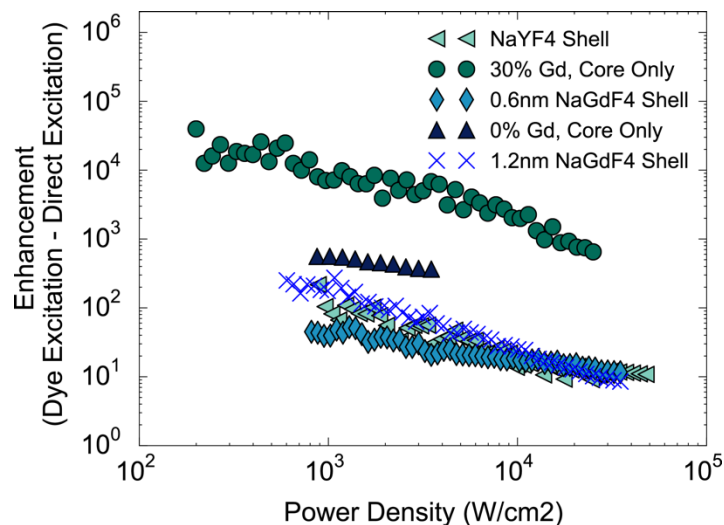


Figure S.3.12. Power-dependent enhancement from dye sensitization

Comparison across many UCNPs sensitized with IR806 dye showing the relative increase in upconverted brightness from exciting the system directly with 980 nm light versus exciting the system through the dye antenna at 808 nm. The 0% Gd³⁺, core sample is analogous to that used by Zou *et al.*²⁵ As can be seen, the 30% Gd³⁺ cores show remarkably high brightness enhancements. It is worth noting that the enhancement factors increase with decreasing power. Thus, while we cannot strictly measure an enhancement factor at excitation intensities in the \sim W/cm² range, we know it is >33,000.

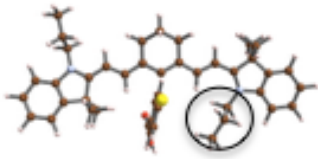
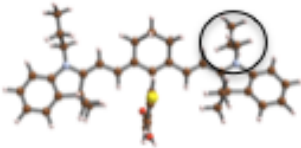
Optimized DFT Geometry	XCF	TDA (eV)	no TDA (eV)
	PBE0	1.0	0.8
	B3LYP	1.0	0.9
	BHLYP	1.0	0.6
	wB97X-D	1.0	0.3
	CAM-B3LYP	0.9	0.4
	B3LYP	1.0	0.9
	BHLYP	1.2	0.8

Table S.3.1. Lowest lying triplet energies from TDDFT calculations.

Exchange Correlation Functional (XCF), Tamm Dancoff approximation (TDA).

Supplementary Discussion

Discussion of Energy Transfer Kinetics

Comparing lifetimes of free IR806 and of IR806 on UCNPs with 0% Gd³⁺ (or, 22% total lanthanide composition with the 20% Yb³⁺ and 2% Er³⁺) in Fig. 3b, we observe a reduction in dye lifetime by a factor of ~2 when functionalized to the 0% Gd³⁺ UCNPs (575 ps vs. 293 ps). This is consistent with the same measurement in Zou *et al.*²⁵

The decay rate of the singlet excited state of the dye can be written as:

$$k_{\text{SingletState}} = k_{\text{dye}} + k_{\text{FRET}} + k_{\text{ISC}}$$

where k_{ISC} is the intersystem crossing rate from the singlet excited state S₁ to the triplet state T₁; k_{FRET} is the FRET rate from S₁ to the UCNP, and k_{dye} is decay rate of S₁ when not in the presence of FRET acceptors or heavy atoms, which we take here to be equal to the decay rate of the free dye.

We know from our measurements with the triplet quencher (Fig. 3c) that the UC quantum yield (UCQY) changes by ~20% when the quencher is added to the dye-UCNP complexes with 0% Gd³⁺ (22% total Ln³⁺). From the approximately linear slope of the “dye excited” curve at low intensities in Fig. 4a, we know that the IR806-UCNPs are operating near the Yb³⁺ saturation regime (due to the antenna effect of the dyes). A linear dependence of emission on excitation fluence means that the ~20% reduction in UCQY implies an ~20% decrease in energy transfer from the dye to the nanoparticle. Thus these data, along with the reduction in dye singlet lifetime by ~2x, allow us to calculate the total FRET and ISC rates to be ~1/0.72 ns and ~1/2.87 ns, respectively. This tells us that singlet-state FRET is the primary energy-transfer mechanism for 22%

Ln^{3+} UCNPs, though ISC is not negligible and is approaching the same order of magnitude as the FRET rate.

Next, we measure nearly another 2-fold reduction in lifetime when the dye is functionalized on the 30% Gd^{3+} UCNPs (52% Ln^{3+}). This gives a further increase in the ISC rate to 1/373 ps, which is 7.7x faster than without the additional Gd^{3+} . Importantly, this implies that decay of the dye singlet state is now dominated by ISC rather than FRET. Further, if we assume that most triplets transfer their energy to the NP, then the primary contribution of energy transfer to the nanoparticle is now from the triplet state. More specifically ~66% of energy transfer to the NP is from the triplet. Note that this agrees remarkably well with the COT triplet quencher measurement on these UCNPs, where a ~60% reduction in UCQY is observed for dyes functionalized on the 30% Gd^{3+} UCNPs (see Fig. 3c).

Comparing to previous reports, this increase in ISC rate by ~8-fold is reasonable and consistent with ISC increases seen, for example, with heavy-atom-enhanced triplet formation in organic electronic polymers⁸¹. Furthermore, the measured ISC rate is also consistent with previous work: as expected, it is slightly slower than the rates observed in heavy-atom-based molecular complexes, which are often in the 10^{10} - 10^{14} s⁻¹ range⁸²⁻⁸⁴, but faster than the FRET rate from the singlet in this system.

This also emphasizes that the notable increase in enhancement relative to Zou *et al.* (~30x higher at low fluences) is rooted in 2 related mechanisms. Namely, (i) that the increased energy transfer rate and shorter singlet lifetimes lead to the UCNP effectively experiencing a higher excitation intensity when there are more triplets, and (ii) this in turn increases the upconverting quantum yield of the system since UCQY is an inherently intensity-dependent value in these nonlinear systems. These two effects are multiplicative. The improvement in UCQY via enhanced ET rates into the particle is particularly pronounced at low excitation intensities, where the UCQYs of the unsensitized (or less-effectively sensitized) UCNPs fall off significantly as pump intensity is reduced, whereas the better-sensitized particles still operate at relatively high UCQY even at these lower intensities since the molecular antennas effectively put the particle in the near-saturation regime of Yb^{3+} (where UCQY is much less sensitive to changes in I). This is shown directly in Fig. 4a and Suppl. Fig. 12, where the upconverted emission enhancement factors increase as excitation power densities decrease. Also, the effect of the dyes on the UCQYs of our 30% Gd^{3+} particles at low power can be seen in Fig. 4b, where the UCQY was measured at a low excitation intensity of 5 Wcm⁻², and can also be seen in Fig. 3a, where the two spectra were collected at the same low intensity (5 Wcm⁻²).

4 Upconverting nanoparticle microbulbs for deep tissue optical stimulation and imaging

4.1 Introduction

With the advent of optogenetics to stimulate neural activity and the rapidly growing field of functional imaging using calcium and voltage indicators, optical imaging and neural stimulation are now becoming powerful techniques to study neural circuits in the brain^{85–88}. Most of these optical tags, and almost all existing opsins have absorption bands in the visible wavelengths; wavelengths that brain tissue strongly absorbs and scatters^{85,89}. Spatial resolution degrades dramatically as a result, as does the achievable excitation depth within the brain, limiting most neural studies to the superficial layers of the cortex. To alleviate this problem, implantable light guides or LEDs have been designed to deliver light deeper into the brain^{90–94}. However, implantable, tethered light guides can significantly damage the brain. Such optical implants can be used for acute experiments, but the invasive nature of these methods—large size and continuous tethering force—prohibits chronic studies on awake, naturally behaving studies. Thus to harness the true power of optical techniques in neuroscience, a less invasive optical delivery method capable of reaching deep regions of the brain is crucial.

To circumvent the shallow penetration depths of visible light in the brain, we propose utilizing near-infrared (NIR) light to penetrate deep into brain tissue^{95,96}. NIR wavelengths take advantage of the decreasing scattering cross-section of light, which falls off as λ^{-4} , as well as the several optical windows at 1200 nm-1400 nm, 1650 nm-1850 nm, 2100 nm- 2250 nm where brain tissue absorption reaches local minima. The extinction spectrum of light through a 1 mm coronal brain slice from an adult C57BL/6 mouse (7-10 weeks old) shows that the extinction of light at the excitation wavelength of Channelrhodopsin-2 (ChR-2) ($\lambda = 480$ nm) is ~ 30 dB through a 2 mm brain slice, whereas the extinction of NIR light at $\lambda = 1300$ nm is only ~ 4 dB⁵.

However, in order to fully utilize the ability of NIR light to deeply penetrate the brain, we must locally convert it to higher wavelengths after it propagates to the target region, since optical reporters and opsins respond primarily to the visible light⁹⁷. In this work, we demonstrate an approach to design implantable, tetherless and passive micro-lightbulbs (MLBs) that can absorb near-infrared light in the optical window and emit visible light locally to stimulate or record neural activity. Such microstructures can be injected into the brain tissue and remain floating via brain micromotions. The proposed MLBs are composed of lanthanide-doped upconverting nanocrystals (UCNPs) encapsulated in the biocompatible polymer parylene. We use NIR light at $\lambda = 980$ nm to reach deep into the brain tissue, minimizing tissue absorption while maximize upconversion efficiency. Herein we discuss the synthesis of UCNPs optimized for Channelrhodopsin excitation and the subsequent fabrication of MLBs. We demonstrate successful imaging of these MLBs through very thick (~ 2 mm) brain slices from a mouse subject. We believe the presented technique can serve as a new and powerful modality for deep brain stimulation and imaging using NIR light in a minimally invasive way.

4.2 Synthesis of UCNPs for bright blue emission

UCNPs exploit the long-lived excited states within the 4f manifolds of the lanthanide ions to efficiently upconvert NIR energies to the visible⁴⁹. This process involves two, three, or more absorptions of NIR photons to progressively excite electrons up the 4f orbital ladder, followed by subsequent Anti-Stokes emission all the way to the ground state (See Figure 4.1). These nanocrystals offer significant advantages in efficiency and wavelength over existing organic dyes recently used for 3-photon fluorescence imaging at depths exceeding 1 mm⁹⁶. We have recently shown that our 3-photon UCNPs can be *orders of magnitude brighter* than organics and comparable to conventional 2-photon UCNPs – which themselves are already 5–6 *orders of magnitude* more efficient than 2-photon fluorescence processes in the best 2-photon dyes -- despite the lower-energy excitation and near-infrared emission⁴⁹.

In this chapter, we optimize UCNP emission with a goal of exciting channelrhodopsins, which absorb light in the range $\lambda = 450\text{--}500\text{ nm}$. We utilize Yb^{3+} as a sensitizer ion ($\lambda_{\text{ex}} = 980\text{ nm}$, ${}^2\text{F}_{7/2} \rightarrow {}^2\text{F}_{5/2}$) due to its much higher absorption cross-section compared with other lanthanide ions, while Tm^{3+} is used as the emitter ion due to its transitions ${}^3\text{H}_4 \rightarrow {}^3\text{H}_6$, ${}^1\text{G}_4 \rightarrow {}^3\text{H}_6$, and ${}^1\text{D}_2 \rightarrow {}^3\text{F}_4$ at 800 nm, 474 nm, and 450 nm, respectively (See Fig. 1)⁴¹. The 800 nm transition allows us to track the MLBs deep within the brain, while the transitions in the blue will be used to excite the Channelrhodopsin.

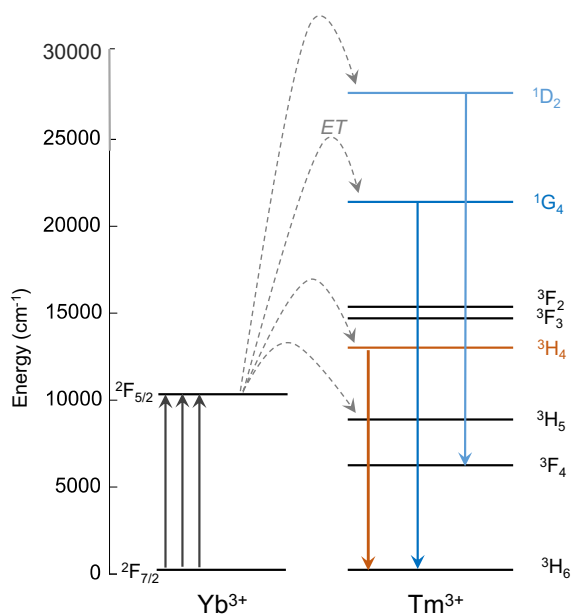


Figure 4.1. Energy level diagram of trivalent Yb and Tm The three primary transitions of interest in Tm, ${}^3\text{H}_4 \rightarrow {}^3\text{H}_6$, ${}^1\text{G}_4 \rightarrow {}^3\text{H}_6$, and ${}^1\text{D}_2 \rightarrow {}^3\text{F}_4$ at 800 nm, 474 nm, and 450 nm, respectively.

Using the Workstation for Automated Nanomaterials Discovery and Analysis (WANDA), a custom-built robot designed to automate the combinatorial discovery of new colloidal nanoparticles⁹⁸, we optimized the Yb^{3+} , Tm^{3+} : UCNPs for blue emission.

As shown in Fig. 4.2a, we found that NaYF₄ UCNPs alloyed with 40% Yb³⁺, 20% Gd³⁺, and 2% Tm³⁺ produce the brightest two and three photon emissions. This figure shows the measured emission spectrum of thin uniform films of nanocrystals immobilized on a glass substrate, when excited with a continuous wave (CW) laser at $\lambda = 980$ nm, with an illumination intensity of 10^3 W/cm². As can be seen, 2% Tm³⁺ particles are much brighter than the other compositions at these powers, in agreement with a previous study.⁹⁹ The emission at 800 nm is much more pronounced than that at 450 nm, since the 800 nm Anti-Stokes emission is a two photon process as opposed to the three photons requires to upconvert 980 nm to 450 nm. However, we propose to use the 800 nm emission to track the MLBs within the brain, since this remains in the NIR-I infrared window. The winning particle cores were 12 nm in diameter, and encapsulated by a 4 nm thick NaYF₄ shell to avoid deleterious non-radiative surface losses^{49,70}.

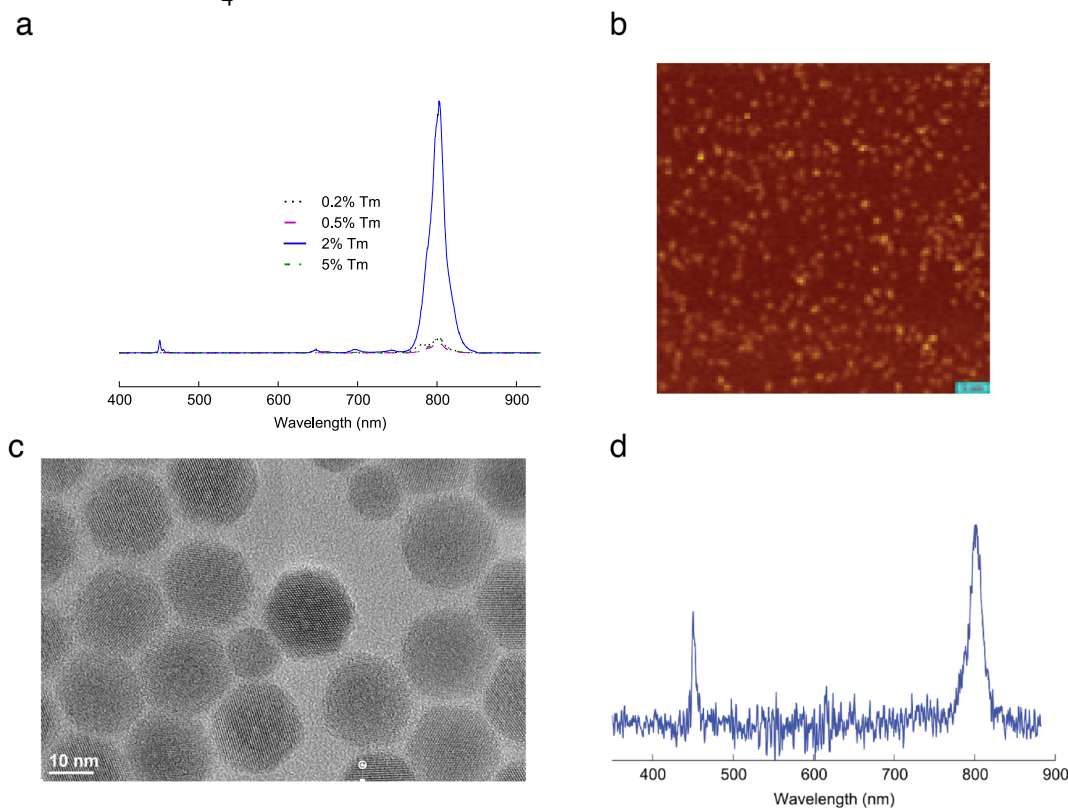


Figure 4.2. Optimization of UCNPs for blue emission. **a.** Upconverted emission spectra comparing Tm concentrations with Yb = 40%, excited with 980nm laser at 10^3 W/cm² **b.** Confocal scan of single UCNPs, 2%Tm, excited with 980nm laser at 10^5 W/cm², 50ms integration time per pixel **c.** HRTEM image of core/shell 2% Tm showing hexagonal beta-phase and continuous single crystal extending from core to shell domain. **d.** Spectrum of single UCNP, 2%Tm, excited at same power as b), integrated for 10 s.

4.3 UCNP micro lightbulbs

A certain threshold intensity of light must be met in order to trigger optical processes in the nervous system. For example, opsins require at least 1 mW/mm^2 of typically blue light to evoke action potentials^{86,100}. We therefore need a large concentration of UCNPs at the target locations in order to generate the threshold intensity of visible light. To achieve this concentration, we encapsulated a thick film of UCNPs in microstructures made of Parylene C, a biocompatible polymer. We call these microstructures micro-light bulbs since they emit visible light when excited with NIR light at $\lambda = 980 \text{ nm}$. These MLBs can be dispersed in artificial cerebrospinal fluid (ACSF) and safely injected into the brain tissue to generate a local high-intensity of visible light inside the brain tissue by virtue of directing the generated light from all the encapsulated UCNPs to the output facets. Parylene C is used as the encapsulating material since it is biocompatible, can be deposited using a chemical vapor deposition (CVD) method at room temperature, and can be micromachined using our previously established fabrication process^{101,102}.

The fabrication process flow is shown in Fig. 4.3a. We start with a 150 mm silicon wafer and pattern global alignment marks using DUV lithography and shallow silicon etching (200 nm). Then we spin coat Dow UV26-3.0 photoresist at 5000 RPM to a thickness of $3.3 \mu\text{m}$. Photoresist is then baked at 130°C for 60 sec on a proximity hot plate. This layer of photoresist is used as a sacrificial layer for the subsequent release of MLBs from the wafer. A layer of Parylene C polymer is then deposited onto the wafer to a thickness of $5 \mu\text{m}$ at room temperature in a Specialty Coating system (PVD 200). An array of disks each with a diameter of $4 \mu\text{m}$ is then lithographically patterned into a DUV210 resist on top of Parylene C using a DUV lithography technique (ASML Stepper 5500/300). The solution of UCNPs dispersed in Toluene is drop coated on the wafer in an equilibrated chamber for $\sim 15 \text{ min}$. Toluene tends to wet the surface of Parylene C much more than the surface of DUV210. As a result, most of the UCNPs dispersed in Toluene are collected into the pits on the Parylene C surface. The equilibrated chamber is then brought to ambient conditions to let the Toluene evaporate. The UCNPs are then mostly coated on the exposed Parylene C surface and some residue remains on photoresist. The UV210 resist is then stripped in Acetone to lift off the unwanted UCNPs. In the next step, a thin layer of Parylene C ($2 \mu\text{m}$) is deposited to cap the UCNP patterns. In a subsequent DUV lithography step, the same pattern of disks is defined with a layer of DUV210 on top, and aligned with the first layer of previously defined disks. A 200 nm layer of Aluminum is then deposited using electron beam evaporation and then lift off as a hardmask on top of the regions with UCNPs. Then we use oxygen plasma to etch Parylene and transfer the pattern of such disks onto Parylene C to form pillars that encapsulate UCNPs. These pillars are our desired micro-light bulbs that will be finally released from the wafer by dissolving the sacrificial layer underneath. Optical micrograph of an array of these MLBs is shown in Fig. 4.3b.

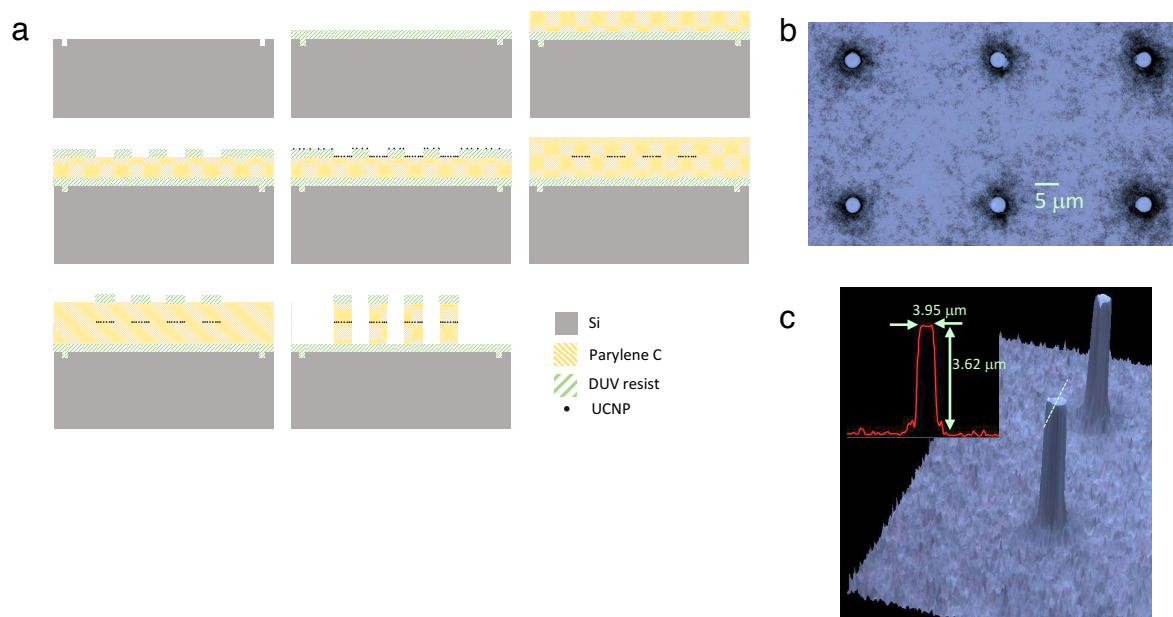


Figure 4.3. Micro lightbulb fabrication a. The fabrication process flow to realize UCNP micro-light bulbs. **b.** An optical micrograph of an array of UCNP micro-light bulbs.

We used a custom-designed inverted confocal microscope to optically characterize the MLBs (Figure 4.4). A CW laser diode at $\lambda = 980$ nm is used to illuminate the sample. An objective lens (40x, NA=0.6) is used to focus the beam of light to a diffraction-limited spot of diameter of 820 nm. The emission is measured in reflection mode, where the pump wavelength is filtered out using a shortpass filter (SP850 with $\lambda_{\text{edge}} = 850$ nm). The emission spectrum can be either routed to a spectrometer or an avalanche photodiode (APD, PDM Series, Micro Photon Devices) using a flip mirror. Using this setup, we can both measure the emission spectrum at a single pixel and also the emission image by integrating the optical power at a single point and moving the sample along x and y directions. The xy stage that is used to hold the sample is equipped with piezoelectric actuators for precise scanning of the sample. A reconstructed image of the emission pattern (filtered in the range of $\lambda = 400$ -900 nm) from our MLB array measured in air is shown in Fig. 5a. The emission pattern from each MLB suggests that the UCNPs are more concentrated around the circumference of the pillars, producing a coffee-ring pattern upon drying. The emission intensity spectrum from a micropillar is shown in Fig. 5b for two different input intensities. It can be seen that the amplitude and shape of the emission spectrum are both nonlinear functions of input intensity. For example, at the input intensity of $I_0 = 10^2$ W/cm², no blue emission is captured, whereas at $I_0 = 10^3$ W/cm², an appreciable amount of blue light emission is measured. To characterize the nonlinear spectral behavior of the emission from micro-light bulbs, we used bandpass filters in front of the APD to filter the emission bands centered on $\lambda = 450$ nm and $\lambda = 800$ nm separately and measured the emission intensities as a function of input intensity. The emission intensity at the blue wavelength

($\lambda = 450$ nm) and at the 800 nm emission bands are plotted as a function of the input excitation intensity in the inset of Fig. 5b. It can be clearly seen that the emission intensities are nonlinear functions of the input intensity and the saturation at high powers happens at lower excitation intensities for the 800 nm emission, as expected. Before saturation, the blue emission intensity scales as $I_0^{2.36}$ and the 800 nm emission scales as $I_0^{1.16}$, where I_0 is the input excitation intensity. The blue emission reaches the saturation regime ($I_{\text{out}} = I_0^{-1}$) at a higher input pump intensity due to its being a three-photon process, contrasted with the two-photon emission at 800 nm. In essence, the saturation regime occurs when the intermediate excited states within the 4f lanthanide manifold are full, and thus incoming photons need only excite these intermediate states as opposed to exciting all the way from the ground state.

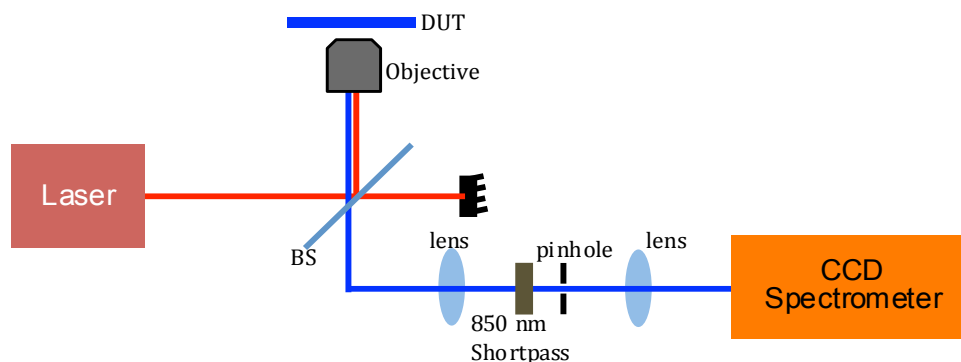


Figure 4.4 Schematic of the characterization setup. A custom-designed confocal microscope is coupled to a cooled-CCD spectrometer. The sample is held on a precision xy stage with piezoelectric actuators.

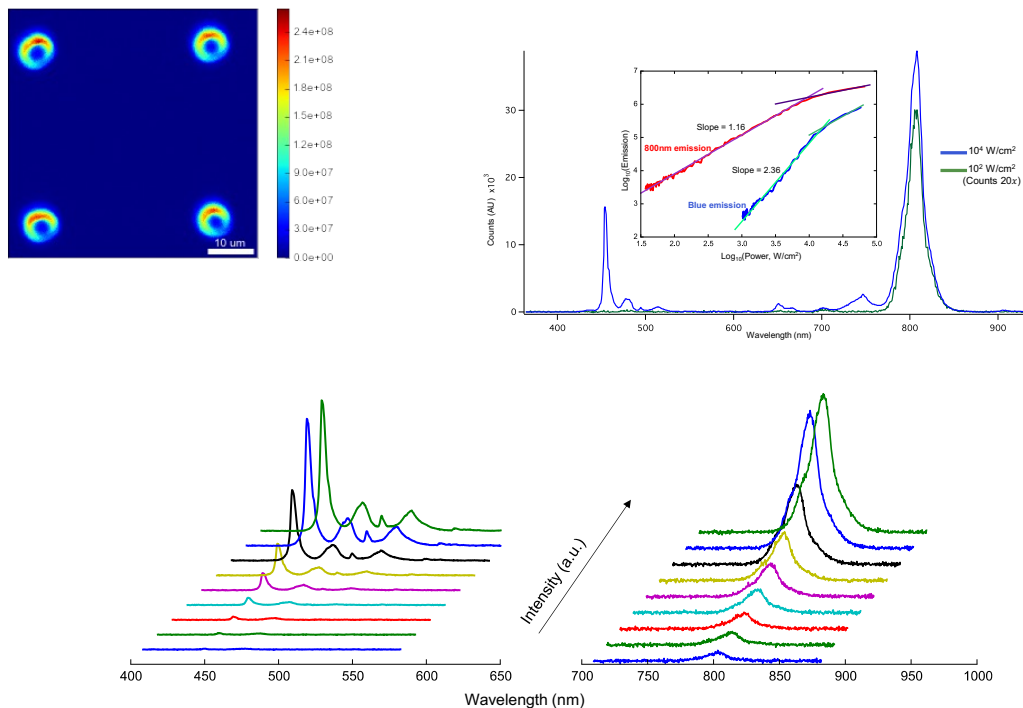


Figure 4.5. Micropillar photoluminescence characterization. (*top left*) Reconstructed confocal scan of UCNP micropillars in air. (*top right*) Upconverted emission power dependence for ${}^3\text{H}_4 \rightarrow {}^3\text{H}_6$ and (${}^1\text{G}_4 \rightarrow {}^3\text{H}_6 + {}^1\text{D}_2 \rightarrow {}^3\text{F}_4$) Tm^{3+} transitions, showing two and three photon dependence, respectively, and characteristic power-dependence saturation at high powers. (*bottom left*) Blue emission waterfall spectra for excitation intensity from 10^3 to 10^4 W/cm^2 shown in and (*bottom right*) 800 nm emission spectra for excitation intensity from 10^2 to 10^3 W/cm^2 .

4.4 Imaging through thick brain slices

To show the efficacy of our MLBs for high resolution delivery of light deep into the brain tissue, we imaged the MLBs through thick coronal brain slices from a mouse subject. Briefly, adult C57BL/6 mice (7-10 weeks old) were anesthetized with isoflurane and decapitated. Using a vibratome (Leica VT1200 S), coronal brain slices were prepared at different thicknesses (ranging from $150\ \mu\text{m}$ to $2\ \text{mm}$) in a chilled slicing solution consisting of (in mM) 234 sucrose, 11 glucose, 24 NaHCO_3 , 2.5 KCl , 1.25 NaH_2PO_4 , 10 MgSO_4 , and 0.5 CaCl . After brain preparation from these mice, slices were incubated in artificial cerebrospinal fluid (ACSF) containing (in mM): 126 NaCl , 26 NaHCO_3 , 2.5 KCl , 1.25 NaH_2PO_4 , 1 MgCl_2 , 2 CaCl , and 10 glucose and equilibrated with 95% O_2 / 5% CO_2 . Slices were then fixed overnight in 4% paraformaldehyde/1X PBS, and individually placed on the MLB array on a silicon substrate to image the emission pattern. The measurement arrangement is depicted in Fig. 4.6a. Fig. 4.6b shows the emission pattern integrated over $\lambda = 400\text{-}800\ \text{nm}$ through a $2\ \text{mm}$ brain slice for a pump intensity of $10^5\ \text{W}/\text{cm}^2$ entering the brain slice. (This power assumes the laser is fully focused at the brain surface. However, the laser actually focuses $2\ \text{mm}$ below the surface, and because of scattering and absorption through the brain, the power at the focal spot through the brain will be considerably less.) The emission spectra at a single

point on top of a pillar is shown in Fig. 4.6c. The integration time at each pixel is 10 ms. As expected the blue emission is highly attenuated through the tissue; however, the NIR emission at $\lambda = 800$ nm can pass through the whole thickness of brain tissue.

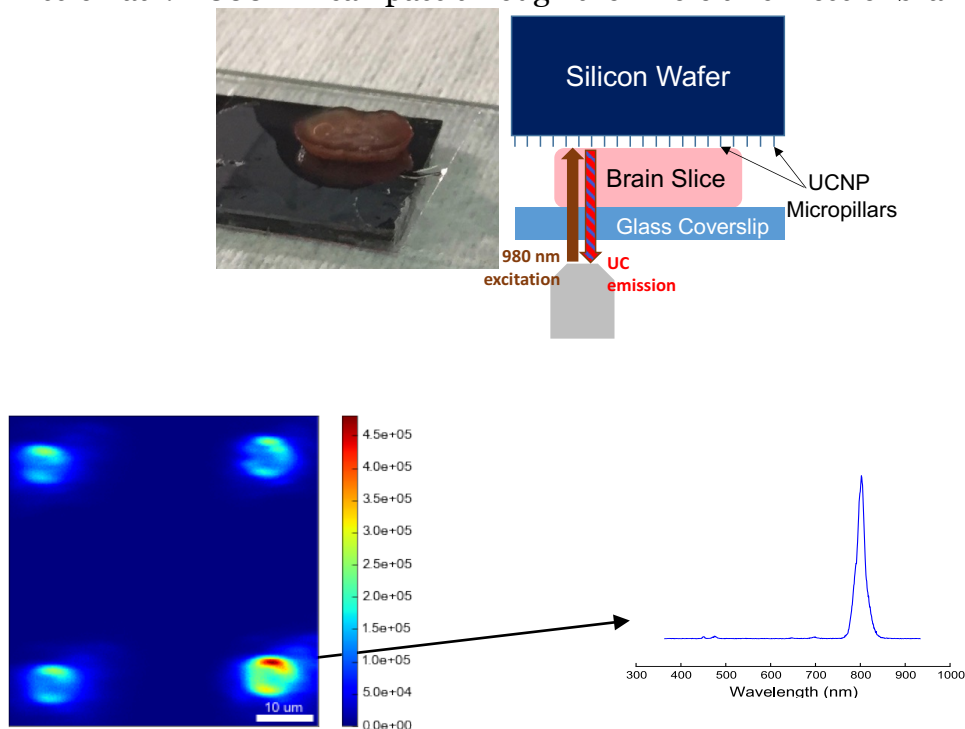


Figure 4.6 Imaging micro lightbulbs through mouse brain. (top) Image of mouse brain slice and schematic of experiment for imaging through slice. (bottom left) Reconstructed confocal scan of UCNP micropillar array, excited and collected through 2 mm mouse brain. Pillars are clearly visible, with some aberration including elongation in the x -direction. (bottom right) Spectrum from pillar collected through 2 mm brain slice; estimated excitation intensity at the pillars is 10^3 W/cm² (see Fig. 4.7).

A finer scan of a single MLB in air and also through the brain slice is shown in Fig. 4.7a. The line cut profiles show that the image of the MLB is only slightly distorted through the brain slice, yet by taking advantage of the low attenuation of NIR light, we are still able to obtain a relatively high resolution image of the MLB through the 2 mm of brain corona.

It is difficult to measure the blue emission intensity through the brain slice, especially below $I_{\text{pump}}=10^3$ mW/mm², where the attenuated emission is very weak and falls below the detectable signal / noise of our APD. However, we can use the NIR emission at $\lambda = 800$ nm as a proxy measurement of the blue emission. Fig. 7c plots the ratio (blue emission at $\lambda = 450$ nm / NIR emission at $\lambda = 800$ nm) against excitation power. Using this calibration curve, we can estimate the local blue emission intensity by measuring the NIR emission intensity coming out of the brain. For example, at a pump intensity of 10^4 W/cm² entering the brain slice, the NIR emission intensity of the MLB is 3.8×10^{-3} mW/mm² when the attenuation of the NIR emission through the tissue is considered. This corresponds to an intensity of 3.8×10^{-5} mW/mm² at $\lambda = 450$ nm

immediately out of the MLBs (assuming a power of $2 \times 10^3 \text{ W/cm}^2$ of 980nm light reaches the MLBs). While blue light at $\lambda = 450 \text{ nm}$ undergoes -30 dB attenuation in 2mm of brain tissue, the pump light at $\lambda = 980 \text{ nm}$ only undergoes -6 dB. Therefore, at the same power, we can reach 250 \times deeper into the brain tissue using MLBs compared to direct illumination of tissue using blue light.

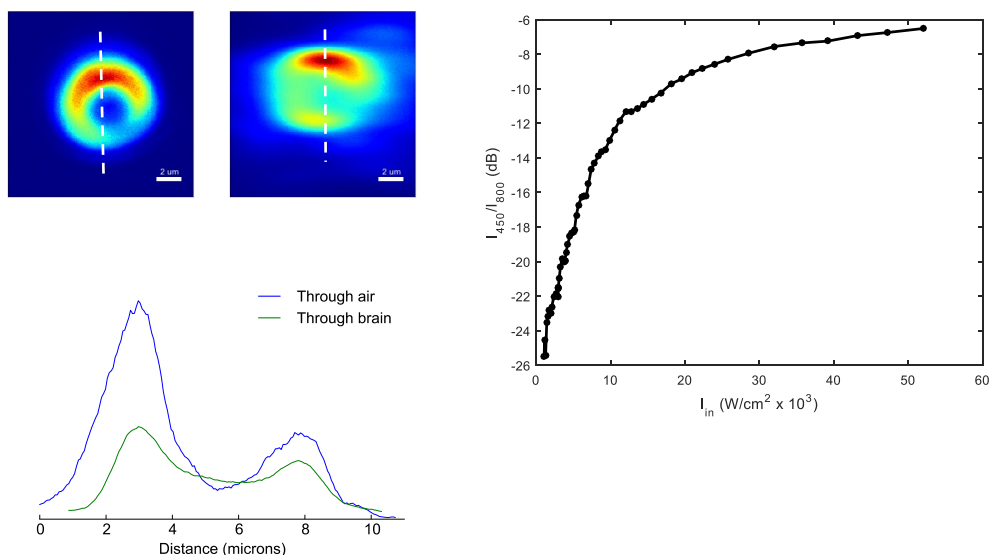


Figure 4.7 Evaluating micro lightbulbs for optogenetic applications. (*top left*) zoomed-in images of UCNP micropillar imaged through air (left) and 2mm brain slice (right). (*bottom left*) Vertical line-cuts through the in-air (blue) and through-slice (green) scans. The measured intensity through air is divided by a scaling factor of 250 for ease of comparison. All scans integrate 800nm emission from UCNPs only, excluding the other wavelengths with interference filters. (*right*) Calibration curve showing the ratio of blue emission to the NIR emission (the ratio of integrated ${}^1\text{G}_4 \rightarrow {}^3\text{H}_6$ transitions) versus excitation power, which is known to be intensity dependent.

4.5 Discussion

In this paper, we demonstrated the implementation of brightly emitting UCNP-based micro lightbulbs for deep-tissue imaging and excitation. The passive MLBs can be injected into the tissue and then remotely excited using an external NIR light source that can penetrate deep into the tissue with less absorption and scattering compared to visible light. As a result of upconversion, visible light is locally emitted from the MLBs, which can be used for optogenetic stimulation among other probing techniques.

Cylindrical MLBs were demonstrated in this paper; however, the concept can be extended to more sophisticated geometries in order to shape the emission beam of the upconverted light arbitrarily through proper design of the MLBs. For example, one can imagine the realization of a lensed facet to focus the emitted light or introducing anisotropies in the MLB shape for more directional emission. The cross section of the light bulb can be arbitrarily defined through optical lithography and etching. Moreover,

we can add metallic reflectors into the structure to enhance collection and directionality of the emitted photons. In addition to beam-shaping, the geometry of the light bulb can be designed to possess resonance modes at the wavelength of excitation and/or emission to further enhance the generation and emission of upconverted photons. Generally, the MLB scheme presented here presents a range of new and promising lines of follow-up research.

The use of NIR light allows for significant penetration depth through tissue. In this paper we used 980 nm light to locally excite the MLBs, maximizing the absorption by the UCNP particles while also minimizing scattering and absorption in the tissue. As the light propagates through the tissue, it gets absorbed and scattered. In particular, ballistic photons are the primary contributors to the upconversion process, and these photons exponentially decay from the surface of the tissue. While increasing the intensity of the excitation source can extend the depth of penetration, beyond a certain level the input intensity would begin to damage the superficial layers of tissue. One solution to alleviate this problem involves pulsing the excitation source. The lifetime of the UCNP excited states are on the order of 100's of μsec , allowing the input laser to be pulsed at a repetition rate of ~ 10 kHz, minimizing phototoxicity without affecting upconversion performance. If these MLBs are used to optogenetically excite neurons, given the millisecond time response of usual opsins, only a small number of such 10 kHz excitation pulses would be required to evoke action potentials. As a result, the laser pulses only need to be on for a fraction of the time.

In this work, we have optimized the chemical composition of our UCNP's to maximize the upconverted blue emission of Tm^{3+} while exciting the $\lambda = 980$ nm transition of the sensitizer Yb^{3+} ions. The optimized UCNP's were used to fabricate micro lightbulbs out of the biocompatible polymer parylene, and we successfully demonstrated that these MLBs can be imaged through 2 mm of mouse brain tissue. To further increase the penetration depth, the excitation wavelength can be shifted to longer wavelengths by using the infrared transitions of Tm^{3+} for instance. For example, it was recently shown that by using an excitation wavelength of $\lambda = 1280$ nm, two-photon imaging is possible at a depth of 1.6 mm into a mouse cortex⁹⁵.

Our results demonstrate the possibility of targeted deep tissue imaging and optical stimulation using the proposed upconverting micro lightbulbs. This concept can be extended to generate arbitrary beam shapes at any desired visible wavelength through optimizing its various modular components.

5 Conclusion

5.1 Summary

Upconversion nanoparticles promise to transform a range of technologies, increasing the efficiency of solar cells or enabling unprecedented biological imaging and manipulation at the cellular or protein level. However, several key challenges remain before these nanoparticles become widely adopted, and some of these challenges differ depending on the application. Dye sensitization remains a promising avenue to address these challenges; yet within this subfield key challenges also remain including overall efficiency of the upconversion process and stability of the hybrid system. In this chapter I will address possible means to overcome these challenges, and bring dye-sensitized UCNPs, and UCNPs more generally, out of the niche lab and into the practical realm.

5.2 Dye-sensitized UCNP efficiency improvement

As discussed at length in Chapter 3 of this work, adding organic dyes to the surface of UCNPs greatly improves the upconversion efficiency, in the case described, by ~100 fold, bringing the overall external quantum efficiency of UCNP cores from ~0.05% to 5%. While this improvement is quite dramatic, it is still an order of magnitude away from an ideal quantum efficiency for this two-photon process, and stepping out of the quest for perfection, is about 4-fold lower than what is needed to see meaningful improvements in solar cell efficiencies¹. Thus these systems still require significant advances in order to reach performances of practical application.

As was also shown in Chapter 3, the lanthanide nuclei within the UCNPs induce intersystem crossing within the organic dye antennae, enabling Dexter electron exchange via the triplet excited state of the dye. Thus the triplet energy states are imperative to a highly efficient system. Not only that, but because the UCNP composition influences the amount of triplets present in the system, this becomes a coupled problem, and therefore the standard optimization procedure of independently optimizing each component individually before combining the constituents becomes invalid. In other words, dye-sensitized UCNPs must be thought of as a single system, and changing parameters such as the amount of Yb³⁺ in the UCNP will have the dual effect of changing the photophysics in the UCNP and changing the amount of triplets available in the dye, and thus changing the photophysics of the dye-UCNP hybrid. Thus the optimization procedure becomes much more challenging.

5.2.1 Dye optimization

If it is possible to choose the triplet energy level of the dye being utilized, the ideal triplet should sit ~2,000 cm⁻¹ in energy above acceptor of the lanthanide, in order to prevent back-transfer from the lanthanide to the triplet¹⁰³. This is in contrast to the direct overlap between the dye triplet and lanthanide acceptor state used in Chapter 3, and therefore suggests that further improvement is possible with a more ideal dye.

Furthermore, the spatial distribution of electron density of the triplet state on the dye molecule should be optimized to allow electron density at or near the linking moiety of the dye. Because triplet energy transfer typically occurs via Dexter electron exchange (See Chapter 1), it is highly distance dependent and requires wavefunction overlap of the electrons in question. This typically is achieved at distances less than 1 nm between the donor and acceptor. Therefore placing triplet electron density on the linker molecule would allow more facile, and more efficient electron, and subsequently energy exchange between the dye and NP¹⁰⁴. The most facile means for achieving this would likely involve incorporating the binding moiety into the conjugated backbone of the dye itself. In practice, this may prove somewhat difficult, or may diminish the brightness of the dye for reasons beyond the scope of this work.

Lastly, if these systems are desired for solar capture applications, it is likely that a dye absorption further into the infrared is needed. The IR-808 dye used in Chapter 3 is proof of concept, but the energies involved with that system are not practical for real-world use (unless a semiconductor material with a bandgap wider than silicon is used, such as a lead halide perovskite.) Unfortunately, finding infrared dyes with absorptions at 1,100-1,200 nm (beyond the wavelength of silicon, but with likely triplet states capable of transferring to the 1330 nm state of Tm³⁺) is difficult, and such large conjugated backbones are likely unstable. Nonetheless, such dye systems need be explored.

If these systems are to be used in biological applications, finding a dye with absorption close to 1300 nm could also be beneficial. This would extend the laser wavelength into one of the deepest brain tissue absorption troughs of the NIR⁵, allowing deeper penetration through tissue. However, a reason for reservation depends on the desired biological application. For imaging, this could be ok, especially if you could then upconvert to the Tm³⁺ 800 nm band, such that a high quantum efficiency photodetector could be used. If, however, the desired application involves optogenetics, the larger loss would likely be moving from a possible two-photon excitation to three-photon excitation (980 nm → 550 nm versus 1330 nm → 550 nm). And this assumes that an opsin with good absorption efficiency in the green is utilized. Thus if optogenetic studies are desired, it is likely prudent to maintain the IR-808 system.

5.2.2 Dye: UCNP optimization

As stated above, the optimal composition of lanthanides within UCNPs coated with organic dyes is likely different from UCNPs that do not utilize dye antennae. Because the dyes are absorbing orders of magnitude more incident radiation than the UCNPs would themselves, the dye: UCNP system will essentially see more of the excitation. This effectively amounts to turning up the laser power without actually doing so, similar to a solar concentrator on top of an expensive semiconductor. Therefore, the UCNP should be optimized with lanthanide compositions more amenable to high laser power. It has been shown⁴⁹ that a higher relative concentration of emitter lanthanides to sensitizer lanthanides is ideal in this environment. A detailed study across lanthanide compositions, however, is needed, because of the added variable of increasing triplet

populations with increasing amount of lanthanide ions in the UCNP relative to Y^{3+} (See Chapter 3).

Stability remains the key challenge when utilizing dyes to enhance UCNP absorption cross-sections. Stability is always an issue when using organic dyes in high-flux applications, and most organic dye lasers utilize a continuous flow of fresh dye to avoid photo bleaching. In these dye:UCNP systems, the (in)stability of the dye is exacerbated by the fact that intersystem crossing to the dye's triplet state is enhanced, and organic dye triplet states easily photobleach by creating singlet oxygen with O_2 molecules from the atmosphere. It is therefore imperative to encapsulate the dye:UCNPs in an air-free environment. For solar applications, it is possible to simply encapsulate the film under glass in the construction of the photovoltaic device. However, for biological applications, where the nanoparticle nature likely need be preserved, a particle-by-particle encapsulation technique should be explored. Methods such as wrapping individual dye-coated UCNPs with polymer impenetrable to air are possible, or even encapsulating each one with an inorganic shell such as silica or titania¹⁰⁵. Care should be taken to avoid damaging the dye during the wrapping or encapsulation. Pinholes in the protective coating also need to be avoided. In summary, this will be an ongoing challenge to using these systems for biology, and easily becomes the key challenge – and critical breakthrough when solved – for use in such systems.

6 Bibliography

1. Briggs, J. A., Atre, A. C. & Dionne, J. A. Narrow-bandwidth solar upconversion: Case studies of existing systems and generalized fundamental limits. *J. Appl. Phys.* **113**, 124509–124514 (2013).
2. Johnson, C. M. & Conibeer, G. J. Limiting efficiency of generalized realistic c-Si solar cells coupled to ideal up-converters. *J. Appl. Phys.* **112**, (2012).
3. Goldschmidt, J. C. & Fischer, S. Upconversion for Photovoltaics - a Review of Materials, Devices and Concepts for Performance Enhancement. *Adv. Opt. Mater.* **3**, 510–535 (2015).
4. Horton, N. G. *et al.* In vivo three-photon microscopy of subcortical structures within an intact mouse brain. *Nat. Photonics* **7**, 205–209 (2013).
5. Levy, E. S. *et al.* Energy-Looping Nanoparticles: Harnessing Excited-State Absorption for Deep-Tissue Imaging. *ACS Nano* **10**, 8423–8433 (2016).
6. Zhou, B., Shi, B., Jin, D. & Liu, X. Controlling upconversion nanocrystals for emerging applications. *Nat. Nanotechnol.* **10**, 924–936 (2015).
7. Chan, E. M. Combinatorial approaches for developing upconverting nanomaterials: high-throughput screening, modeling, and applications. *Chem. Soc. Rev.* **44**, 1653–1679 (2015).
8. Steinkemper, H., Fischer, S., Hermle, M. & Goldschmidt, J. C. Stark level analysis of the spectral line shape of electronic transitions in rare earth ions embedded in host crystals. *New J. Phys.* **15**, (2013).
9. Ostrowski, A. D. *et al.* Controlled Synthesis and Single-Particle Imaging of Bright, Sub-10 nm Lanthanide-. *ACS Nano* **6**, 2686–2692 (2012).
10. Kramer, K. W. *et al.* Hexagonal Sodium Yttrium Fluoride Based Green and Blue Emitting Upconversion Phosphors. *Chem. Mater.* **16**, 1244–1251 (2004).
11. Chan, E. M. *et al.* Combinatorial discovery of lanthanide-doped nanocrystals with spectrally pure upconverted emission. *Nano Lett.* **12**, 3839–45 (2012).
12. Zhong, Y. *et al.* Elimination of photon quenching by a transition layer to fabricate a quenching-shield sandwich structure for 800 nm excited upconversion luminescence of Nd³⁺-sensitized nanoparticles. *Adv. Mater.* **26**, 2831–2837 (2014).
13. Wu, S. *et al.* Non-blinking and photostable upconverted luminescence from single lanthanide-doped nanocrystals. *Proc. Natl. Acad. Sci. U. S. A.* **106**, 10917–21 (2009).

14. Wang, F. *et al.* Simultaneous phase and size control of upconversion nanocrystals through lanthanide doping. *Nature* **463**, 1061–5 (2010).
15. Wang, J. *et al.* Enhancing multiphoton upconversion through energy clustering at sublattice level. *Nat. Mater.* **13**, 157–62 (2014).
16. Wisser, M. D., Fischer, S., Alivisatos, A. P., Salleo, A. & Dionne, J. A. Emission Enhancement via Local Symmetry Distortion in Lanthanide-Based Upconverting Nanoparticles. 1–2 (2016). doi:10.1021/acsphotonics.6b00166
17. Fischer, S., Bronstein, N. D., Swabeck, J. K., Chan, E. M. & Alivisatos, A. P. Precise tuning of surface quenching for luminescence enhancement in core-shell lanthanide-doped nanocrystals. *Nano Lett.* **16**, 7241–7247 (2016).
18. Nag, A. *et al.* Metal-free inorganic ligands for colloidal nanocrystals: S²⁻, HS⁻, Se²⁻, HSe⁻, Te²⁻, HTe⁻, TeS₃²⁻, OH⁻, and NH₂⁻ as surface ligands. *J. Am. Chem. Soc.* **133**, 10612–10620 (2011).
19. Boles, M. A., Ling, D., Hyeon, T. & Talapin, D. V. The surface science of nanocrystals. *Nat. Mater.* **15**, 141–153 (2016).
20. Fischer, S., Johnson, N. J. J., Pichaandi, J., Goldschmidt, J. C. & Van Veggel, F. C. J. M. Upconverting core-shell nanocrystals with high quantum yield under low irradiance: On the role of isotropic and thick shells. *J. Appl. Phys.* **118**, (2015).
21. Pokhrel, M., Kumar, G. A. & Sardar, D. K. Highly efficient NIR to NIR and VIS upconversion in Er³⁺ and Yb³⁺ doped in M₂O₂S (M = Gd, La, Y). *J. Mater. Chem. A* **1**, 11595–11606 (2013).
22. Johnson, N. J. J. & van Veggel, F. C. J. M. Lanthanide-Based Heteroepitaxial Core-Shell Nanostructures: Compressive versus Tensile Strain Asymmetry. *ACS Nano* **8**, 10517–10527 (2014).
23. Upconversion, P., Wu, D. M., Garc, A., Salleo, A. & Dionne, J. A. Plasmon-Enhanced Upconversion. (2014).
24. Sun, Q.-C. *et al.* Plasmon-enhanced energy transfer for improved upconversion of infrared radiation in doped-lanthanide nanocrystals. *Nano Lett.* **14**, 101–6 (2014).
25. Zou, W., Visser, C., Maduro, J. a., Pshenichnikov, M. S. & Hummelen, J. C. Broadband dye-sensitized upconversion of near-infrared light. *Nat. Photonics* **6**, 560–564 (2012).
26. Chen, G. *et al.* Energy-cascaded upconversion in an organic dye-sensitized core/shell fluoride nanocrystal. *Nano Lett.* **15**, 7400–7407 (2015).
27. Klink, S. I., Keizer, H. & van Veggel, F. C. J. M. Transition metal complexes as photosensitizers for near-infrared lanthanide luminescence. *Angew. Chemie Int. Ed.* **39**, 4319–4321 (2000).

28. Beeby, A., Faulkner, S., Parker, D. & Williams, J. A. G. Sensitised luminescence from phenanthridine appended lanthanide complexes: analysis of triplet mediated energy transfer processes in terbium, europium and neodymium complexes. *J. Chem. Soc. Perkin Trans. 2* 1268–1273 (2001). doi:10.1039/b009624p
29. Faulkner, S., Natrajan, L. S., Perry, W. S. & Sykes, D. Sensitised luminescence in lanthanide containing arrays and d-f hybrids. *Dalton Trans.* 3890–3899 (2009). doi:10.1039/b902006c
30. Forster, T. Zwischenmolekulare Energiewanderung und Fluoreszenz. *Ann. Phys.* **33**, 55–75 (1948).
31. Dexter, D. L. A Theory of Sensitized Luminescence in Solids. *J. Chem. Phys.* **21**, 836 (1953).
32. Brown, A. & Wilkinson, F. Intermolecular energy transfer in rigid matrices at 77K. *J. Chem. Soc. Faraday Trans. 2 Mol. Chem. Phys.* **75**, 880–895 (1979).
33. Watson, W. M., Zerger, R. P., Yardley, J. T. & Stucky, G. D. Examination of photophysics in rare earth chelates by laser-excited luminescence. *Inorg. Chem.* **14**, 2675–2680 (1975).
34. Crosby, G. a., Whan, R. E. & Alire, R. M. Intramolecular Energy Transfer in Rare Earth Chelates. Role of the Triplet State. *J. Chem. Phys.* **34**, 743 (1961).
35. Chen, G. *et al.* Efficient broadband upconversion of near-infrared light in dye-sensitized core/shell nanocrystals. *Adv. Opt. Mater.* **4**, 1760–1766 (2016).
36. Chen, G. *et al.* Energy-Cascaded Upconversion in an Organic Dye-Sensitized Core/Shell Fluoride Nanocrystal. *Nano Lett.* acs.nanolett.5b02830 (2015). doi:10.1021/acs.nanolett.5b02830
37. Steigerwald, M. L. *et al.* Surface derivatization and isolation of semiconductor cluster molecules. *J. Am. Chem. Soc.* **110**, 3046–3050 (1988).
38. Polte, J. Fundamental Growth Principles of Colloidal Metal Nanoparticles - a new Perspective. *CrystEngComm* **17**, 6809–6830 (2015).
39. Fultz, B. & Howe, J. *Transmission Electron Microscopy and Diffractometry of Materials.* (2008).
40. Zou, W., Visser, C., Maduro, J. a., Pshenichnikov, M. S. & Hummelen, J. C. Broadband dye-sensitized upconversion of near-infrared light. *Nat. Photonics* **6**, 560–564 (2012).
41. Park, Y. Il, Lee, K. T., Suh, Y. D. & Hyeon, T. Upconverting nanoparticles: a versatile platform for wide-field two-photon microscopy and multi-modal in vivo imaging. *Chem. Soc. Rev.* **44**, 1302–1317 (2014).

42. Liu, Y. *et al.* Amplified stimulated emission in upconversion nanoparticles for super-resolution nanoscopy. *Nature* **543**, 229–233 (2017).
43. Wang, C., Li, X. & Zhang, F. Bioapplications and biotechnologies of upconversion nanoparticle-based nanosensors. *Analyst* **141**, 3601–3620 (2016).
44. Wu, X. *et al.* Dye-sensitized core/active shell upconversion nanoparticles for optogenetics and bioimaging applications. *ACS Nano* **10**, 1060–1066 (2016).
45. Hososhima, S. *et al.* Near-infrared (NIR) up-conversion optogenetics. *Sci. Rep.* **5**, 16533 (2015).
46. Schmidt, T. W. & Castellano, F. N. Photochemical Upconversion : The Primacy of Kinetics. **1**, 1–31 (2014).
47. Schulze, T. F. & Schmidt, T. W. Photochemical upconversion: present status and prospects for its application to solar energy conversion. *Energy Environ. Sci.* **8**, 103–125 (2015).
48. Olivier, J. H. *et al.* Near-infrared-to-visible photon upconversion enabled by conjugated porphyrinic sensitizers under low-power noncoherent illumination. *J. Phys. Chem. A* **119**, 5642–5649 (2015).
49. Gargas, D. J. *et al.* Engineering bright sub-10-nm upconverting nanocrystals for single-molecule imaging. *Nat. Nanotechnol.* **9**, 300–5 (2014).
50. Park, Y. Il *et al.* Nonblinking and nonbleaching upconverting nanoparticles as an optical imaging nanoprobe and T1 magnetic resonance imaging contrast agent. *Adv. Mater.* **21**, 4467–4471 (2009).
51. Shao, W. *et al.* Tunable narrow band emissions from dye-sensitized core/shell/shell nanocrystals in the second near-infrared biological window. *J. Am. Chem. Soc.* **138**, 16191–16195 (2016).
52. Lee, J. *et al.* Ultra-wideband multi-dye-sensitized upconverting nanoparticles for information security application. *Adv. Mater.* **29**, 1603169 (2017).
53. Du, C., Wang, H., Yang, F. & Hammel, P. C. Systematic variation of spin-orbit coupling with d -orbital filling: Large inverse spin Hall effect in 3d transition metals. *Phys. Rev. B - Condens. Matter Mater. Phys.* **90**, 1–5 (2014).
54. Klink, S. I. *et al.* A systematic study of the photophysical processes in polydentate triphenylene-functionalized Eu 3+. *J. Phys. Chem. A* **104**, 5457–5468 (2000).
55. Bunzli, G., J.-C. & Pigué C. Taking advantage of luminescent lanthanide ions. *Chem. Soc. Rev.* **34**, 1048–1077 (2005).
56. Thompson, N. J. *et al.* Energy harvesting of non-emissive triplet excitons in tetracene by emissive PbS nanocrystals. *Nat. Mater.* **13**, 1039–1043 (2014).

57. Cedric, M., Garakyaraghi, S., Razgoniaeva, N., Zamkov, M. & Castellano, F. N. Direct observation of triplet energy transfer from semiconductor nanocrystals. *Science* (80-.). **351**, 369–372 (2016).
58. Tabachnyk, M. *et al.* Resonant energy transfer of triplet excitons from pentacene to PbSe nanocrystals. *Nat. Mater.* **13**, 1033–1038 (2014).
59. Agbo, P., Xu, T., Sturzbecher-Hoehne, M. & Abergel, R. J. Enhanced ultraviolet photon capture in ligand-sensitized nanocrystals. *ACS Photonics* **3**, 547–552 (2016).
60. Huang, Z. *et al.* Hybrid molecule-nanocrystal photon upconversion across the visible and near-infrared. *Nano Lett.* 150710114602002 (2015). doi:10.1021/acs.nanolett.5b02130
61. Piland, G. B., Huang, Z., Lee Tang, M. & Bardeen, C. J. Dynamics of Energy Transfer from CdSe Nanocrystals to Triplet States of Anthracene Ligand Molecules. *J. Phys. Chem. C* **120**, 5883–5889 (2016).
62. Wang, F. *et al.* Tuning upconversion through energy migration in core-shell nanoparticles. *Nat. Mater.* **10**, 968–73 (2011).
63. Marling, J. B., Gregg, D. W. & Wood, L. Chemical quenching of the triplet state in flashlamp-excited liquid organic lasers. *Appl. Phys. Lett.* **17**, 527–530 (1970).
64. Pappalardo, R., Samelson, H. & Lempicki, A. Long pulse laser emission from rhodamine 6 G using cyclooctatetraene. *Appl. Phys. Lett.* **16**, 267–269 (1970).
65. Schols, S., Kadashchuk, A., Heremans, P., Helfer, A. & Scherf, U. Triplet excitation scavenging in films of conjugated polymers. *ChemPhysChem* **10**, 1071–1076 (2009).
66. Schaap, A. P. *Singlet Molecular Oxygen*. (John Wiley and Sons, 1976).
67. Gorke, A. P., Nani, R. R., Zhu, J., Mackem, S. & Schnermann, M. J. A near-IR uncaging strategy based on cyanine photochemistry. *J. Am. Chem. Soc.* **136**, 14153–14159 (2014).
68. Han, Y. *et al.* Degradation observations of encapsulated planar CH₃NH₃PbI₃ perovskite solar cells at high temperatures and humidity. *J. Mater. Chem. A* **3**, 8139–8147 (2015).
69. Boyer, J.-C. & van Veggel, F. C. J. M. Absolute quantum yield measurements of colloidal NaYF₄: Er³⁺, Yb³⁺ upconverting nanoparticles. *Nanoscale* **2**, 1417 (2010).
70. Johnson, N. J. J. *et al.* Direct evidence for coupled surface and concentration quenching dynamics in lanthanide-doped nanocrystals. *J. Am. Chem. Soc.* **139**, 3275–3282 (2017).

71. Chan, E. M., Levy, E. S. & Cohen, B. E. Rationally Designed Energy Transfer in Upconverting Nanoparticles. *Adv. Mater.* **27**, 5753–5761 (2015).
72. Ostrowski, A. D. *et al.* Controlled synthesis and single-particle imaging of bright, sub-10 nm lanthanide-doped upconverting nanocrystals. *ACS Nano* **6**, 2686–2692 (2012).
73. Li, X. *et al.* Successive Layer-by-Layer Strategy for Multi-Shell Epitaxial Growth: Shell Thickness and Doping Position Dependence in Upconverting Optical Properties. *Chem. Mater.* **25**, 106–112 (2013).
74. Fritzing, B., Capek, R. K., Lambert, K. & Martins, C. Utilizing Self-Exchange To Address the Binding of Carboxylic Acid Ligands to CdSe Quantum Dots. *Jacs* 10195–10201 (2010).
75. Martin, R. L. Natural transition orbitals. *J. Chem. Phys.* **118**, 4775–4777 (2003).
76. Mewes, J. M. *et al.* Experimental benchmark data and systematic evaluation of two a posteriori, polarizable-continuum corrections for vertical excitation energies in solution. *J. Phys. Chem. A* **119**, 5446–5464 (2015).
77. You, Z. Q., Mewes, J. M., Dreuw, A. & Herbert, J. M. Comparison of the Marcus and Pekar partitions in the context of non-equilibrium, polarizable-continuum solvation models. *J. Chem. Phys.* **143**, (2015).
78. Champagne, B., Guillaume, M. & Zutterman, F. TDDFT investigation of the optical properties of cyanine dyes. *Chem. Phys. Lett.* **425**, 105–109 (2006).
79. Fabian, J. TDDFT-calculations of Vis/NIR absorbing compounds. *Dye. Pigment.* **84**, 36–53 (2010).
80. Peach, M. J. G., Williamson, M. J. & Tozer, D. J. Influence of triplet instabilities in TDDFT. *J. Chem. Theory Comput.* **7**, 3578–3585 (2011).
81. Rothe, C., King, S. & Monkman, A. P. Long-range resonantly enhanced triplet formation in luminescent polymers doped with iridium complexes. *Nat. Mater.* **5**, 463–466 (2006).
82. Baryshnikov, G., Minaev, B. & Ågren, H. Theory and calculation of the phosphorescence phenomenon. *Chem. Rev.* **117**, 6500–6537 (2017).
83. Rachford, A. A., Goeb, S. & Castellano, F. N. Accessing the triplet excited state in perylenediimides. *J. Am. Chem. Soc.* **130**, 2766–2767 (2008).
84. Danilov, E. O. *et al.* Ultrafast energy migration in platinum (II) diimine complexes bearing pyrenylacetylde chromophores. *J. Phys. Chem. A* **109**, 2465–2471 (2005).
85. Deisseroth, K. Optogenetics. *Nat. Methods* **8**, 26–29 (2010).

86. Boyden, E. S. A history of optogenetics: the development of tools for controlling brain circuits with light. *F1000 Biol. Rep.* **3**, (2011).
87. Baker, B. J. *et al.* Imaging brain activity with voltage-and calcium-sensitive dyes. *Cell. Mol. Neurobiol.* **25**, 245–282 (2005).
88. Djurusic, M. *et al.* Voltage-sensitive dyes. (2002).
89. Yang, L. & Miklavcic, S. J. Revised Kubelka-Munk theory. III. A general theory of light propagation in scattering and absorptive media. *J. Opt. Soc. Am. A* **22**, 1866 (2005).
90. Zorzos, A. N., Scholvin, J., Boyden, E. S. & Fonstad, C. G. Three-dimensional multiwaveguide probe array for light delivery to distributed brain circuits. *Opt. Lett.* **37**, 4841–3 (2012).
91. Wu, F. *et al.* An implantable neural probe with monolithically integrated dielectric waveguide and recording electrodes for optogenetics applications. *J. Neural Eng.* **10**, 56012 (2013).
92. Abaya, T. V. F., Blair, S., Tathireddy, P., Rieth, L. & Solzbacher, F. A 3D glass optrode array for optical neural stimulation. *Biomed. Opt. Express* **3**, 3087–104 (2012).
93. Zorzos, A. N., Boyden, E. S. & Fonstad, C. G. Multiwaveguide implantable probe for light delivery to sets of distributed brain targets. *Opt. Lett.* **35**, 4133–5 (2010).
94. Chamanzar, Maysamreza ; Borysov, Mykhailo ; Maharbiz, Michel ; Blanche, T. High-Density Optrodes for Multi-Scale Electrophysiology and Optogenetic Stimulation. in *IEEE EMBS* (2014).
95. Kobat, D., Horton, N. G. & Xu, C. In vivo two-photon microscopy to 1.6-mm depth in mouse cortex. *J. Biomed. Opt.* **16**, 106014 (2011).
96. Horton, N. G. *et al.* In vivo three-photon microscopy of subcortical structures within an intact mouse brain. **7**, 205–209 (2013).
97. Fenno, L., Yizhar, O. & Deisseroth, K. The development and application of optogenetics. *Annu. Rev. Neurosci.* **34**, 389–412 (2011).
98. Chan, E. M. *et al.* Reproducible, high-throughput synthesis of colloidal nanocrystals for optimization in multidimensional parameter space. *Nano Lett.* **10**, 1874–1885 (2010).
99. Zhao, J. *et al.* Single-nanocrystal sensitivity achieved by enhanced upconversion luminescence. *Nat. Nanotechnol.* **8**, 729–34 (2013).
100. Pashaie, R. *et al.* Optogenetic brain interfaces. *IEEE Rev. Biomed. Eng.* **7**, 3–30 (2014).

101. Muller, R. *et al.* 24.1 A miniaturized 64-channel 225 μ W wireless electrocorticographic neural sensor. in *2014 IEEE International Solid-State Circuits Conference Digest of Technical Papers (ISSCC)* 412–413 (IEEE, 2014). doi:10.1109/ISSCC.2014.6757492
102. Ledochowitsch, P., Olivero, E., Blanche, T. & Maharbiz, M. M. A transparent μ ECoG array for simultaneous recording and optogenetic stimulation. *Conf. Proc. IEEE Eng. Med. Biol. Soc.* **2011**, 2937–40 (2011).
103. Latva, M. *et al.* Correlation between the lowest triplet state energy level of the ligand and lanthanide(III) luminescence quantum yield. *J. Lumin.* **75**, 149–169 (1997).
104. Wood, C. J., Robson, K. C. D., Elliott, P. I. P., Berlinguette, C. P. & Gibson, E. a. Novel triphenylamine-modified ruthenium(ii) terpyridine complexes for nickel oxide-based cathodic dye-sensitized solar cells. *RSC Adv.* **4**, 5782–5791 (2014).
105. Ow, H. *et al.* Bright and stable core-shell fluorescent silica nanoparticles. *Nano Lett.* **5**, 113–117 (2005).